Monthly Notices
of the
ROYAL ASTRONOMICAL SOCIETY

MNRAS **544,** 3900–3935 (2025)
Advance Access publication 2025 October 30

https://doi.org/10.1093/mnras/staf1867

BlackTHUNDER – A non-stellar Balmer break in a black hole-dominated little red dot at $z = 7.04$

Xihan Ji,[1,2★] Roberto Maiolino,[1,2,3] Hannah Übler,[4] Jan Scholtz,[1,2] Francesco D'Eugenio,[1,2] Fengwu Sun,[5] Michele Perna,[6] Hannah Turner,[1,2] Stefano Carniani,[7] Santiago Arribas,[6] Jake S. Bennett,[5] Andrew Bunker,[8] Stéphane Charlot,[9] Giovanni Cresci,[10] Mirko Curti,[11] Eiichi Egami,[12] Andy Fabian,[13] Kohei Inayoshi,[14] Yuki Isobe,[1,2,15] Gareth Jones,[1,2] Ignas Juodžbalis,[1,2] Nimisha Kumari,[16] Jianwei Lyu,[12] Giovanni Mazzolari,[17,18] Eleonora Parlanti,[4,8] Brant Robertson,[19] Bruno Rodríguez Del Pino,[6] Raffaella Schneider,[20,21,22,23] Debora Sijacki,[1,13] Sandro Tacchella,[1,2] Alessandro Trinca,[21,22,24] Rosa Valiante,[21,22] Giacomo Venturi,[8] Marta Volonteri,[9] Chris Willott,[25] Callum Witten[26] and Joris Witstok[27,28]

Affiliations are listed at the end of the paper

Accepted 2025 October 24. Received 2025 October 24; in original form 2025 January 22

ABSTRACT

Recent observations from *James Webb Space Telescope* (*JWST*) have revealed an abundant population of active galactic nuclei (AGNs) and the so-called 'Little Red Dots' (LRDs) at $2 \lesssim z \lesssim 11$, many of which are characterized by V-shaped UV-to-optical continua with turnovers around the Balmer limit. The physical nature of these LRDs is unclear, and it remains debated whether the peculiar spectral shape originates from AGN, compact galaxies, or both. We present the analysis of new NIRSpec-IFU data from the BlackTHUNDER *JWST* Large Programme and archival NIRSpec-MSA data of a lensed LRD at $z = 7.04$. The spectra confirm the presence of a smooth Balmer break and a broad Hβ tracing the Broad Line Region (BLR) of an AGN. The small velocity dispersion of the Hβ narrow component indicates a small dynamical mass of the host galaxy of $M_{\rm dyn} < 4 \times 10^8$ M$_\odot$, which implies that the stellar population cannot contribute more than 10 per cent to the optical continuum. We show that the Balmer break can be well described by an AGN continuum absorbed by very dense ($n_{\rm H} \sim 10^{10}$ cm^{-3}) and nearly dust-free gas along our line of sight (possibly gas in the BLR or its surrounding). The same gas is expected to produce Hβ absorption, at a level consistent with a tentative detection (3σ) in the high-resolution spectrum. Such a non-stellar origin of the Balmer break may apply to other LRDs, and would alleviate the issue of extremely high stellar mass surface densities inferred in the case of a stellar interpretation of the Balmer break. We note that this is a rare case of a black hole that is overmassive relative to both the host galaxy stellar and dynamical masses. We finally report indications of variability and the first attempt of AGN reverberation mapping at such an early epoch.

Key words: galaxies: active – galaxies: high-redshift.

1 INTRODUCTION

The first two years of observations with the *James Webb Space Telescope* (*JWST*) have revealed a large number of accreting black holes (active galactic nuclei, AGNs) at $2 \lesssim z \lesssim 11$ (e.g. Y. Harikane et al. 2023; D. D. Kocevski et al. 2023; R. L. Larson et al. 2023; M. Perna et al. 2023; H. Übler et al. 2023; J. E. Greene et al. 2024; J. Matthee et al. 2024; R. Maiolino et al. 2024a; I. Juodžbalis et al. 2024b; R. Maiolino et al. 2024b; H. Übler et al. 2024b; M. Perna et al. 2025; J. Scholtz et al. 2025). A significant fraction of these AGNs were classified as Type 1, through the detection of a broad component in permitted emission lines (primarily Hα and/or Hβ) with a full-width-at-half-maximum (FWHM) $\gtrsim 1000$ km s^{-1}, and without a counterpart in forbidden emission lines (in particular [O III]λ5008), indicating that the broad component emerges from the Broad Line Region of AGN (BLR; Y. Harikane et al. 2023; D. D. Kocevski et al. 2023; H. Übler et al. 2023; R. Tripodi et al. 2024; R. Maiolino et al. 2024a; A. J. Taylor et al. 2025). An even more abundant population of narrow-line (Type 2) AGN has also been identified by the detection of high-ionization emission lines or by using narrow-line diagnostic diagrams (e.g. J. Chisholm et al. 2024; G. Mazzolari et al. 2024b, 2025; J. Scholtz et al. 2025). All these studies have opened the exploration of intermediate-/low-luminosity AGN with typically estimated $L_{\rm bol} \lesssim 10^{45}$ erg s^{-1} and $M_{\rm BH} \lesssim 10^{7-8}$ M$_\odot$ at $z \gtrsim 4$, populating a parameter space not sampled by observations in the pre-*JWST* era.

However, the new population of AGN revealed by *JWST* has properties that are quite different compared to the general population of AGN in the local Universe as well as luminous and distant quasars

---

★ E-mail: xj274@cam.ac.uk

(QSOs). In fact, most of the *JWST* selected AGN are characterized by significant X-ray weakness, many of them showing no detection of hard X-ray emission at $2-10$ keV in the rest frame (T. T. Ananna et al. 2024; J. Lyu et al. 2024; M. Yue et al. 2024b; R. Maiolino et al. 2025b), as well as radio weakness, at 5 GHz in the rest frame (I. Juodžbalis et al. 2024a; G. Mazzolari et al. 2024a). In terms of continuum emission, many *JWST*-selected AGN with multi-epoch photometry seem to lack variability in the rest-frame optical and UV (M. Kokubo & Y. Harikane 2024; R. Maiolino et al. 2025b; Z. Zhang et al. 2025). In terms of emission lines, the Type 1 AGN selected by *JWST* show a significantly weaker Fe II emission bump in the optical compared to low-redshift AGN with similar luminosities (B. Trefoloni et al. 2025). In addition, the loci of *JWST*-selected AGN in widely used optical narrow-line diagnostic diagrams such as BPT/VO diagrams (J. A. Baldwin, M. M. Phillips & R. Terlevich 1981; S. Veilleux & D. E. Osterbrock 1987) are clearly offset from those of low-redshift AGN (Y. Harikane et al. 2023; H. Übler et al. 2023; R. Maiolino et al. 2024b). These peculiarities have raised concerns about the true identities of these *JWST*-selected sources and prompted the question of non-AGN scenarios for explaining this population of objects (M. Kokubo & Y. Harikane 2024; M. Yue et al. 2024b; R. Maiolino et al. 2025b). However, it has been shown, on various physical and observational grounds, that currently proposed non-AGN scenarios are not tenable for most of these sources and produce more difficulties (M. Killi et al. 2024; I. Juodžbalis et al. 2024a; R. Maiolino et al. 2025b; Ji et al., in preparation). Alternatively, the above peculiarities of *JWST*-selected AGN might be explainable in the context of high (near-to-super Eddington) gas accretion around the central black hole and/or dense gas obscuration due to changes in the BLR structure (e.g. R. Schneider et al. 2023; A. King 2024; P. Madau & F. Haardt 2024; F. Pacucci & R. Narayan 2024; A. Trinca et al. 2024; K. Inayoshi & R. Maiolino 2025; K. Inayoshi, S. S. Kimura & H. Noda 2025; P. Madau 2025; B. Trefoloni et al. 2025; R. Maiolino et al. 2025b).

A fraction of this new population of AGN uncovered by *JWST* exhibits further peculiar features by having red optical colours and compact morphologies in their NIRCam images, and ‘V-shaped’ spectral energy distributions (SEDs) with turnovers at roughly 4000 Å in the rest frame (e.g. J. E. Greene et al. 2024; D. J. Setton et al. 2024; B. Wang et al. 2025). Based on the above observational facts, these sources are usually referred to as ‘Little Red Dots’ (LRDs). Notably, not all *JWST*-selected AGN are found to be LRDs, and not all LRDs are identified as AGN. While the fraction of AGN among LRDs is debated (ranging between 20 per cent and 80 per cent, e.g. J. E. Greene et al. 2024; P. G. Pérez-González et al. 2024; D. D. Kocevski et al. 2025), which likely depends on the specific criteria for selecting LRDs, the opposite has been established quite carefully: only about 10 per cent–30 per cent of the new population of Type 1 AGN discovered by *JWST* have colours and/or slopes typical of LRDs (K. N. Hainline et al. 2025), although the fraction probably depends on luminosity and redshift.

An intriguing feature of spectroscopically confirmed LRDs is the presence of a prominent break at around 4000 Å in the rest frame (e.g. L. J. Furtak et al. 2024; J. E. Greene et al. 2024; B. Wang et al. 2024, 2025; D. D. Kocevski et al. 2025). If this feature is interpreted as the Balmer break associated with stellar populations, one usually obtains very high stellar masses and, combined with the compact sizes of LRDs ($R_\mathrm{e} \lesssim 100$ pc), extremely high stellar densities ($\sim 10^4-10^7$ $\mathrm{M}_\odot$ pc^{-2} from a maximum AGN contribution to no AGN contribution, see e.g. J. F. W. Baggen et al. 2024) not observed in galaxies at lower redshift (e.g. J. F. W. Baggen et al. 2024; C. A. Guia, F. Pacucci & D. D. Kocevski 2024; B. Wang et al. 2024, 2025; Y. Ma et al. 2025; H. B. Akins et al. 2025b). In fact, such a high density is only comparable locally to the nuclear star clusters (NSCs) at the center of galaxies (e.g. P. F. Hopkins et al. 2010; H. Pfister et al. 2020). For example, the NSC in the Milky Way (MW) has a stellar density of $\sim 10^{6.4}$ $\mathrm{M}_\odot$ pc^{-2} but is only within the central 0.5 pc (N. Neumayer, A. Seth & T. Böker 2020). In addition, the implied stellar mass densities from LRDs within the cosmic volume might be in tension with the standard ΛCDM cosmology (K. Inayoshi & K. Ichikawa 2024; B. Wang et al. 2024; H. B. Akins et al. 2025b). The above stellar Balmer break interpretation hence raises the questions of what physical mechanisms make these systems so massive and what could dissolve these systems into the galaxies at low redshift.

Another interesting feature found in $10-20$ per cent of the Type 1 AGN newly discovered by *JWST* (including LRDs) is the presence of Hα and/or Hβ absorption along with the broad emission components (e.g. I. Labbé et al. 2024; X. Lin et al. 2024; J. Matthee et al. 2024; B. Wang et al. 2024, 2025; I. Juodžbalis et al. 2024a; D. D. Kocevski et al. 2025; A. J. Taylor et al. 2025). These absorption features are relatively narrow (with typical FWHM $\sim 100-200$ km s^{-1}) yet deep (with typical equivalent widths of EW $\gtrsim 4$ Å). The centroids of the absorption are generally slightly blueshifted (typically by $\sim$100–200 km s^{-1}), but there are cases in which the absorption is nearly at the rest frame of the narrow-line emission or even redshifted (e.g. I. Labbé et al. 2024; J. Matthee et al. 2024). If the Balmer absorption observed in LRDs comes from photospheric absorption in stars, based on the extremely high stellar masses inferred from the Balmer break ($\gtrsim 10^{10}$ $\mathrm{M}_\odot$) and the small sizes (< 100 pc) of LRDs, the expected FWHM should be $\gtrsim 1000$ km s^{-1} (J. F. W. Baggen et al. 2024), which is significantly broader than the observed widths. Additionally, the large EW of the Hα absorption (relative to the continuum) is generally far larger than observed in any stellar population. Furthermore, many of these absorption features show velocity offsets relative to both the narrow and broad Hα. Therefore, the Balmer absorption in these systems cannot have a stellar origin.

The findings of the Balmer absorption lines are surprising because, unlike lines that are often seen in absorption such as C IV$\lambda\lambda$1548, 1551, Hα and Hβ are not resonant lines (i.e. the lower level of the emission, $n = 2$ of hydrogen, is not even metastable and is extremely short-lived). Hence, to see Balmer lines in absorption, it requires the $n = 2$ level of hydrogen to be populated and to keep it populated. By studying an AGN with deep Balmer absorption selected by *JWST* at $z = 2.26$, I. Juodžbalis et al. (2024a) showed that, in order to produce the observed absorption, one needs [in addition to temperatures typical of the warm ionized interstellar medium (ISM), which is $\sim 10^4$ K] gas densities higher than 10^8 cm^{-3}. The required densities are much higher than the densities found in the ISM of any galaxies at $0 \lesssim z \lesssim 10$ (X. Ji et al. 2020; R. L. Davies et al. 2021; Y. Isobe et al. 2023; S. Li et al. 2025). In fact, such high densities are more typical of the clouds in the BLRs of AGN (H. Netzer 1990). Given the identifications of AGN in these sources, a natural explanation is that we are seeing absorption from clouds within or very close to the BLRs. Since the BLR clouds are supposed to lie within the dust sublimation radius and are thus likely dust free (although some dust might still be present in the outer BLRs, e.g. G. A. Shields, R. R. Ludwig & S. Salviander 2010), the broad-line emission is not extinguished by dust despite the potentially large column densities of these clouds ($\sim 10^{23}$ cm^{-2}; H. Netzer 1990). The small velocities and velocity dispersions of the absorption lines imply that such nuclear gas is not rapidly outflowing.

It is worth noting that the current fraction of the Balmer absorption among *JWST*-discovered AGN and LRDs is about 10–20 per cent, but this is likely a lower limit. This is because detecting Hα (not to mention Hβ) in absorption requires high signal-to-noise (S/N) and high spectral resolutions, as the absorption can be hidden by the narrow component in the emission of the same line. For instance, F. D'Eugenio et al. (2025b) report a case where Hα absorption is seen when using R2700 spectroscopy, while the same absorption is undetected in the R1000 spectrum. Since most of the *JWST* spectra for Type 1 AGN are obtained with low-resolution NIRSpec/PRISM ($R\sim100$) and medium-resolution NIRSpec/grating ($R\sim1000$) or NIRCam/grism ($R\sim1600$) spectroscopy, the Balmer absorption lines in these AGNs might well go undetected.

Within the same context, K. Inayoshi & R. Maiolino (2025) have pointed out that the presence of Hα and/or Hβ in absorption must also entail the absorption in higher order Balmer lines and the presence of a Balmer break. In addition, K. Inayoshi & R. Maiolino (2025) point out that at least part of the Balmer break seen in LRDs (with broad line detections) discovered by *JWST* could have a non-stellar origin, and the non-stellar part must be associated with the same dense gas responsible for Hα and/or Hβ absorption. As speculated by K. Inayoshi & R. Maiolino (2025), the Balmer breaks observed in LRDs can potentially be entirely associated with non-stellar gas absorption, although thus far, no full-spectral fitting attempts have been made for individual spectra of *JWST* selected LRDs confirmed as broad-line sources. The non-stellar explanation for the Balmer breaks in LRDs has the advantages of alleviating the issue associated with extreme stellar densities as well as the need for special dust attenuation laws (see e.g. Z. Li et al. 2025; Y. Ma et al. 2025). Still, these aspects remain to be tested with actual observations.

In the context of broad-line LRDs in observations, Abell 2744-QSO1 is one of the most intriguing and enigmatic objects. It was first identified by L. J. Furtak et al. (2023) as a triply imaged red point-like source lensed by the cluster Abell 2744, as part of observations from the UNCOVER survey (Ultra-deep NIRSpec and NIRCam ObserVations before the epoch of reionization; PIs: I. Labbé, R. Bezanson; R. Bezanson et al. 2024). Subsequent low-resolution (PRISM) NIRSpec-MSA spectroscopy confirmed a spectroscopic redshift at $z=7.04$ and identified the presence of broad Hβ, which indicates the presence of an AGN (L. J. Furtak et al. 2024). This source also has a V-shaped continuum, with a red optical slope and a blue UV slope in the rest frame (L. J. Furtak et al. 2024). The spectrum shows, as in other LRDs, the presence of a turnover around 4000 Å, resembling the shape of a Balmer break. However, as pointed out recently by Y. Ma et al. (2025), the spectral shape of Abell 2744-QSO1 cannot be well reproduced with a stellar continuum and an associated Balmer break without invoking a large stellar mass of $M_*\approx4\times10^9$ M$_\odot$, an unusually steep dust attenuation law, and a dust attenuated AGN continuum in the rest-frame optical. The derived stellar mass, combined with the small size of the system ($R_\mathrm{e}<30$ pc), places Abell 2744-QSO1 among the galaxies with the highest stellar mass surface density observed to date ($>10^6$ M$_\odot$ pc^{-2}; Y. Ma et al. 2025). Even with the best-fitting model that includes the above assumptions, the reduced χ^2 of the fit *excluding* emission lines and the continuum region close to Lyα emission is 2.85 (table 2 of Y. Ma et al. 2025, the full range is $\chi^2_\nu=2.74-4.32$ based on different model assumptions). On the other hand, the same authors point out that an AGN continuum absorbed by dust cannot reproduce the shape of the turnover either, unless a very peculiar extinction curve is assumed.

In this work, we combine previous NIRSpec-MSA spectroscopic observations of Abell 2744-QSO1 with newly obtained high-resolution (grating; $R\sim2700$) and low-resolution (PRISM; $R\sim100$) NIRSpec-integral field unit (IFU) spectroscopic observations from the BlackTHUNDER Large Programme (Black holes in THe early Universe aNd their DensE surRoundings; PID 5015; PIs: H. Übler, R. Maiolino). Among other findings, we illustrate that the shape of the continuum can be fit by an AGN continuum absorbed by dense gas along the line of sight, which reproduces the smooth Balmer break seen in the low-resolution spectrum and the tentative Hβ absorption seen in the high-resolution spectrum.

The layout of the paper is as follows. In Sections 2 and 3, we describe the observational data and the data reduction. In Section 4, we describe our spectral measurements. In Section 5, we present our derivation of the black hole parameters and discuss them in the context of scaling relations. In Section 6, we describe our new method to fit the UV-to-optical *JWST*/NIRSpec spectra of Abell 2744-QSO1 and present our fitting results. In Section 7, we present our analysis on the variability of Abell 2744-QSO1 based on multiple observations. We discuss the implications of our results in Section 8 and draw our conclusions in Section 9. Throughout this work, we assume a flat ΛCDM cosmology with $h=0.674$ and $\Omega_\mathrm{m}=0.315$ (Planck Collaboration VI 2020).

2 OBSERVATIONAL DATA

2.1 BlackTHUNDER NIRSpec-IFU spectra

We used integral field spectra from the BlackTHUNDER Large Programme (PID 5015; PIs: H. Übler, R. Maiolino). The programme consists of observations with the NIRSpec-IFU mode (T. Böker et al. 2022, 2023; P. Jakobsen et al. 2022), both at high (G395H, hereafter R2700) and low (PRISM) spectral resolution, of a sample of 20 Broad-Line AGNs previously identified by *JWST* MSA observations at $z>5$.[1]

Image A of Abell-2744-QSO1 was observed for 7.4 h with the high-resolution grating G395H and 2 h with the PRISM on 2024 December 10. Image A is less magnified than image B. However, image B is contaminated by a bright foreground galaxy, closer than 1 arcsec in projection. 14 dithers with the 'medium' pattern were adopted for both observations. For the grating observation, 26 groups and the NRSIRS2 readout mode were adopted, while for the PRISM observation, we used 34 groups and the NRSIRS2RAPID pattern (B. J. Rauscher et al. 2017).

We downloaded raw data files from the Barbara A. Mikulski Archive for Space Telescopes (MAST) and subsequently processed them with the *JWST* Science Calibration pipeline.[2] version 1.15.0 under the Calibration Reference Data System (CRDS) context jwst_1281.pmap. To increase data quality, we made the following modifications to the default reduction steps (see M. Perna et al. 2023, for details): count-rate frames were corrected for $1/f$ noise through a polynomial fit; and during calibration in Stage 2, we removed regions affected by failed open MSA shutters and strong cosmic ray residuals. Remaining outliers were flagged in individual exposures using an algorithm similar to LACOSMIC (P. G. Dokkum 2001) and we rejected the 95th (99.5th) percentile of the resulting distribution for the grating (PRISM) observations. The cubes were combined using the 'drizzle' method and reconstructed using a 0.″05 spaxel scale. To identify residual outliers not flagged by the procedures summarized previously, we used the ERROR extension of the data cubes. We flagged any pixels whose error is 10× above the median

---

[1] The sample was selected from published sources at the time of the proposal writing and excluded those already having IFU observations.

[2] https://jwst-pipeline.readthedocs.io/en/stable/jwst/introduction.html

error value of the cubes. We verified that this choice of threshold does not have any impact on the emission line maps by using the 5 and 20 thresholds without any changes to our results.

To perform background subtraction, we mask the location of the source based on its Hβ emission (2σ S/N contours). Then, we estimate the background using `astropy.photutils.background.Background2D` (2D background estimator) task with 5×5 spaxels box window, for each individual channel in the data cubes. We visually inspected the resulting background spectra and found no evidence of narrow features (e.g. emission or absorption lines). Therefore, we smoothed the background in spectral space using a median filter with a width of 25 channels to reduce any noise effects. The final estimated background is subtracted from the flux data cubes.

As a basis for our scientific analysis of the NIRSpec-IFU data, we extracted the integrated PRISM spectrum with an extraction aperture of diameter $0\farcs25$. We also estimated the wavelength-dependent aperture losses by extracting the spectrum with a much larger diameter of $0\farcs5$. The latter spectrum is much more noisy, but can be used to estimate the total flux of the source at each wavelength, which was then used to correct the flux (as a function of wavelength) of the smaller (and higher S/N) aperture spectrum. The average correction factor around Hβ is 1.8. The integrated grating spectrum is extracted from the same circular aperture of $0\farcs25$ and a similar process for aperture-loss correction is applied. However, the flux extracted from the grating spectrum is roughly a factor of 1.9 higher than that of the PRISM spectrum near the location of Hβ, possibly due to a flux calibration issue. We also compare the flux of the IFU PRISM spectrum with that of the MSA PRISM spectrum (image A with the GTO reduction; see also Sections 2.2.2 and 7) and find good consistency. Therefore, we scale the flux of the grating spectrum to match that of the PRISM spectrum.

Previous works have noted that the error extension in the combined NIRSpec-IFU cube can be underestimated (e.g. H. Übler et al. 2023; B. Rodríguez Del Pino et al. 2024). To obtain realistic uncertainties on our aperture-integrated spectra, we rescale the noise spectrum with a measurement of the noise obtained from the sigma-clipped rms of the integrated spectra in regions free of line emission.

The top panel of Fig. 1 shows the field of view of the IFU observation and the extraction aperture on top of the NIRCam images (to be introduced in the next subsection) and IFU images. The middle panel shows the extracted 1D PRISM spectrum for image A from BlackTHUNDER together with MSA spectra from images A + C and images A + B + C, which we introduce in Section 2.2.2. The bottom panel of Fig. 1 shows a portion of the extracted spectrum around Hβ and [O III]$\lambda\lambda$4960, 5008, illustrating the well resolved broad component of Hβ, a clear narrow component of Hβ and a narrow [O III]λ5008. Hβ also presents a tentative detection of an absorption feature, which will be discussed in Section 4.

2.2 Archival data

2.2.1 Imaging

Abell 2744-QSO1 was initially discovered through NIRCam imaging observations of UNCOVER in November 2022 (L. J. Furtak et al. 2023; R. Bezanson et al. 2024). Cycle-1 DDT-2756 (PI: Chen) also obtained NIRCam imaging observations covering the three images of Abell 2744-QSO1 on 2022 October 20 and December 6. The repeated filters are F115W, F150W, F200W, F277W, F356W, and F444W. In November–December 2023, Cycle-2 program GO-3516 (All the Little Things, ALT; R. P. Naidu et al. 2024) obtained repeated NIRCam imaging observations in the F356W band at two PAs. We have processed these imaging data through the same *JWST* pipeline version 1.11.2 and CRDS context `jwst_1174.pmap`. In addition to the standard *JWST* pipeline, we also include many frequently adopted customized steps, such as $1/f$ noise subtraction, additional bad pixel masking, wisp removal, and global background subtraction. For the UNCOVER observations, two epochs of DDT-2756 and ALT images are mosaicked separately with a common world coordinate system (WCS) at a pixel size of $0\farcs03$, and the astrometry is tied to Gaia DR3 (Gaia Collaboration 2023).

2.2.2 Spectroscopy

NIRSpec-MSA PRISM spectroscopy of the three lensed images of Abell 2744-QSO1 were obtained between 2023 July 31 and August 2 (R. Bezanson et al. 2024; L. J. Furtak et al. 2024). The observations are discussed in detail in L. J. Furtak et al. (2024). Here we only briefly summarize that the observations used a 2-points dithers pattern with a 3-shutters nodding strategy for background subtraction. The total exposure times for the three images ranged from 9.4 to 16.4 h.

We also use the spectrum of the three images extracted and combined by L. J. Furtak et al. (2024) and present the analysis in Appendix C. However, we also re-process the MSA PRISM spectra of the three images with the NIRSpec GTO pipeline, following the same procedure described in F. D'Eugenio et al. (2025c). We note that, especially for exploring variability (in contrast with some previous studies) the spectra must be extracted from the full shutter, as it is the only extraction that guarantees accurate path losses and diffraction losses corrections. Additionally, the spectra should be extracted from the individual 2D dithered spectra and then the extracted 1D spectra should be combined. Extracting 1D spectra from the 2D-combined spectra is deprecated as the combination of the 2D spectra does not preserve the path losses and diffraction losses of each individual spectrum.

When the spectra of the three images are compared, image B shows a bluer spectrum at wavelengths shorter than ~ 3 µm, when compared to the spectra of the A and C images. This can be clearly seen in Appendix C, where the three spectra are normalized to the flux densities at $\lambda = 3.6$ µm. The reason for this difference in shape is unlikely due to variability but instead to improper background subtraction of the spectrum of image B because of the extended emission of a foreground, large, and bluer galaxy, located about $0\farcs9$ in projection from image B. We therefore do not use image B in our analysis, and combine the spectra of images A and C, normalized and inverse variance weighted.

The GTO-processed and combined spectra of images A and C are shown in Fig. 1, where they are compared with the combined spectrum in L. J. Furtak et al. (2024) as well as the PRISM spectrum of image A from the BlackTHUNDER programme as described in Section 2.1. The spectra are generally consistent with each other, but they also present some deviations. One difference is that the noise estimated for the GTO-processed spectra is higher than the one inferred by L. J. Furtak et al. (2024). The lack of one of the spectra (image B) cannot explain the difference in the noise. The reason, as when comparing many other spectra between the GTO and other pipelines, is that the noise (ERROR) extension of the GTO pipeline incorporates a factor to account for the effect of correlated noise (B. Dorner et al. 2016), which is instead typically not accounted for by the other pipelines. The finer grid of the GTO pipeline also partly contributes to the higher noise. The

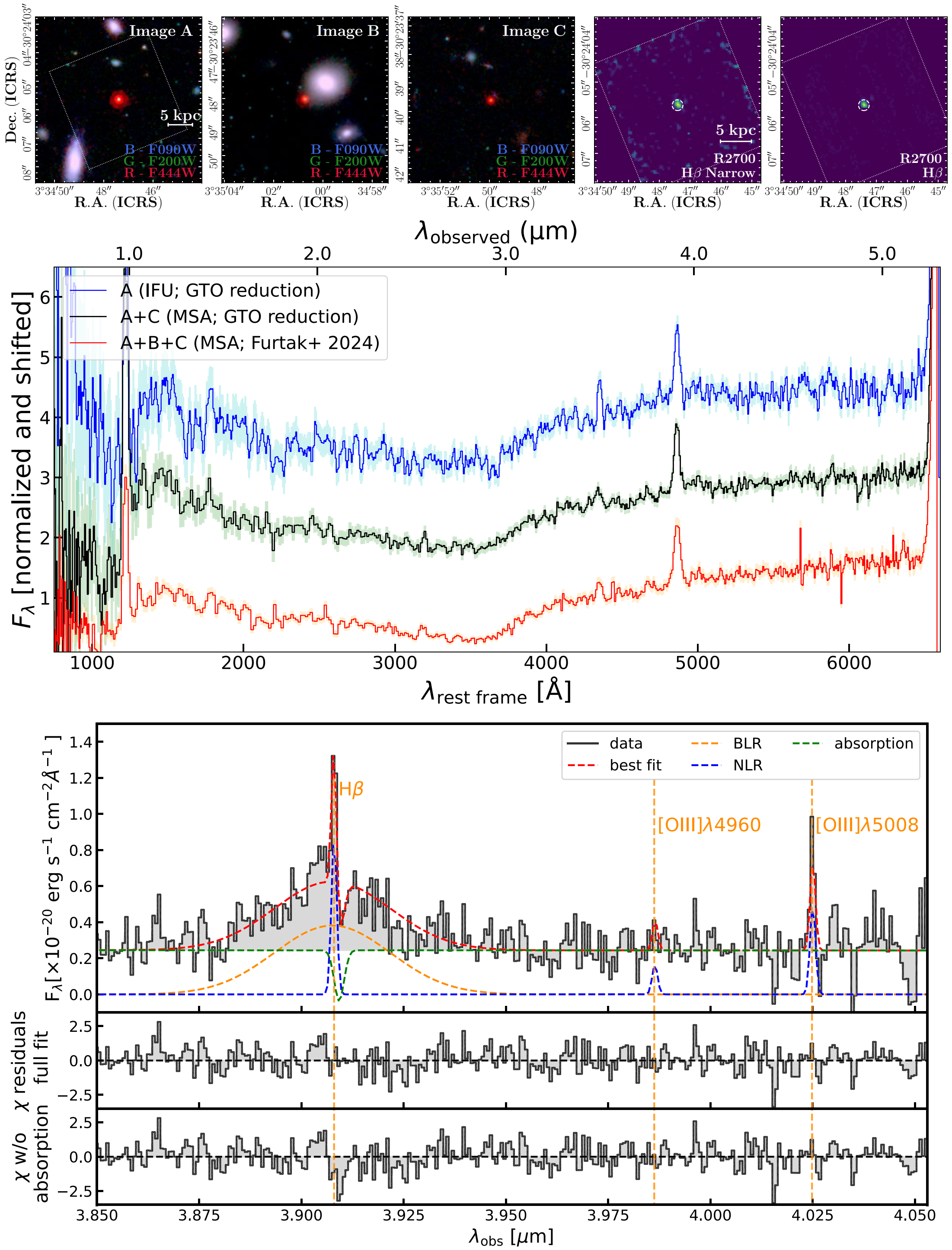

Figure 1. Observations of the triply imaged Abell 2744-QSO1. *Top:* Colour-composite NIRCam images as well as NIRSpec/IFU maps. The NIRCam images of three lensed images from the UNCOVER DR4 (S. H. Price et al. 2025) are shown, where the field of view of the IFU observation for image A is indicated by the dotted white rectangular aperture. For IFU maps, fluxes of the narrow and the whole Hβ are shown and the extraction aperture for the PRISM and grating spectra is indicated by the dashed white circle. *Middle:* IFU and MSA PRISM spectra combining different lensed images normalized to the flux density at $\lambda = 4260$ Å in the rest frame. The spectra are manually shifted in the y axis for presentation purposes. From top to bottom, the spectra correspond to the central region of image A extracted from a circular aperture with a diameter of 0.″25 using the BlackTHUNDER IFU observations with the GTO reduction, the A and C images combined from the MSA observations with the GTO reduction (image B is removed due to the background subtraction issue described in Section 2), and the A, B, and C images combined from the MSA observations with L. J. Furtak et al. (2024)'s reduction, respectively. The shaded regions correspond to the 1σ pipeline uncertainties. *Bottom:* The high-resolution (R2700) BlackTHUNDER IFU spectrum of image A extracted from a circular aperture of 0.″25 zoomed around the location of Hβ and [O III]λλ4960, 5008. The dashed lines are the best-fitting emission line and continuum models, which show a tentative absorption in Hβ at a significance of 3σ. The two bottom panels show the residuals normalized by uncertainties (χ = residual/σ) of fits with and without the Hβ absorption, respectively. The fit with the Hβ absorption produces improved χ residuals near the centroid of the broad Hβ (∼ 3.91 µm).

additional difference is that at short wavelengths ($\lambda < 1.3$ μm) our A + C combined and GTO-pipeline-processed spectrum is bluer than the L. J. Furtak et al. (2024) spectrum; the difference likely originates from the problematic background subtraction in image B used in the combined L. J. Furtak et al. (2024) spectrum. However, this spectral region is not critical for the modelling of the source, except when trying to explore the contribution of the nebular continuum, as discussed later. Indeed, in Appendix C we show that fitting the combined spectra by L. J. Furtak et al. (2024) provides an equally good fit – the reduced χ^2 is higher, but primarily as a consequence of the lower estimation of the errors in that spectrum.

3 PHOTOMETRY FROM IMAGING

According to L. J. Furtak et al. (2023) and Y. Ma et al. (2025), the three images of Abell 2744-QSO1 are unresolved. As already mentioned, image B is located in the halo of a bright foreground galaxy, located about 0."9 in projection. This may cause some problems in the photometry and, as already discussed, in the background subtraction of the MSA spectrum. The foreground galaxy and its halo are much bluer than Abell 2744-QSO1, hence the contamination effect is likely most significant in the blue bands. As we are predominantly interested in the spectroscopic aspects of Abell 2744-QSO1, we mostly rely on the UNCOVER photometry provided by L. J. Furtak et al. (2023).

However, for exploring variability, we also extracted photometry from the UNCOVER, DDT-2756, and ALT images in the F356W and F444W filters, covering the wavelength redder than the Balmer break. F356W is the only band used in these three programmes. Circular aperture photometry is conducted with radius $r = 0.''15$. Local background is measured using a circular annulus and subtracted. We correct for aperture loss assuming the `webbpsf` model and compute photometric uncertainty from random-aperture experiments in source-free regions. The F356W and F444W flux densities of all three images are similar to those reported by L. J. Furtak et al. (2024), and we do not find photometric variability at a significance level higher than 3σ for any of the images, similar to previous studies (Z. Zhang et al. 2025). Yet, variations of up to 25 per cent can be potentially consistent with photometric errors and calibration/flat-field uncertainties for image C in DDT-2756 epochs.

4 SPECTRAL MEASUREMENTS

The spectral fitting of the low-resolution PRISM spectra will be discussed extensively in Section 6. For Lyα, which is not modelled in Section 6, we measured its basic properties. To be consistent with the grating-based measurements, we measured Lyα observed in the image A. We remain agnostic about the physical nature of the continuum during the fit by using a power law to describe the UV continuum, where the region near the Lyα damping wing is described by a step function convolved with the instrumental line spread function (LSF) of the NIRSpec PRISM spectrum. For Lyα, we fitted it as a Gaussian function, which is LSF-dominated due to the low resolution of PRISM ($R \lesssim 50$ near 1 μm). Therefore, the kinematics of Lyα remain largely unconstrained.

Next, we focus on the analysis and fitting of the various components of the Hβ line (as well as the tentative detection of [O III]) in the high resolution BlackTHUNDER spectrum. We fitted the integrated aperture R2700 spectra of this source (see bottom panel of Fig. 1) as a series of Gaussian profiles for emission and absorption lines, and a power law to describe the continuum, using the `Fitting` routines in `QubeSpec` code.[3] We fit the Hβ and [O III]$\lambda\lambda$4960, 5008. To each of the emission lines we fit a single Gaussian profile to describe the narrow component of the emission lines, tying their redshift (centroid) and intrinsic FWHM to a common value to reduce the number of free parameters, leaving the flux of each Gaussian profile free. We fixed the [O III]λ5008/[O III]λ4960 flux ratio to be 2.99, given by the Einstein coefficients (M. S. Dimitrijević et al. 2007). The broad line region and the absorption associated with it is modelled as a Gaussian profile with its own redshift and FWHM. The FWHM of each emission line is convolved with the line spread function of NIRSpec from the JDOCS.[4]

We note that recently, it was found that the broad Hα observed in LRDs is better described by two Gaussians (e.g. M. Brazzini et al. 2025; X. Ji et al. 2025; X. Lin et al. 2025; F. D'Eugenio et al. 2025a) or an exponential (X. Ji et al. 2025; V. Rusakov et al. 2025), when enough S/N is achieved. The double-Gaussian broad lines were also observed in some AGN at $z \sim 2$ (D. J. D. Santos et al. 2025). For Abell 2744-QSO1, specifically, the broad-line profile is discussed extensively by F. D'Eugenio et al. (2025a), R. Maiolino et al. (2025a), and I. Juodžbalis et al. (2025b), who show that, by extending the nominal wavelength coverage of the NIRSpec spectrum with a customized reduction to cover Hα, the broad Hα is better described by two Gaussians. R. Maiolino et al. (2025a) also suggest that the broad Hβ might have an intermediate component, which, however, seems to be spatially resolved and thus likely associated with a (low-metallicity) outflow. I. Juodžbalis et al. (2025b) reach the same conclusion for the intermediate Gaussian component of Hα, which they found to be spatially resolved. Given these results, we also attempted fitting the broad Hβ with two Gaussians, and we used the Bayesian Inference Criterion (BIC; A. R. Liddle 2007) to check whether the double-Gaussian model is preferred. We found $\Delta\mathrm{BIC} = -46 < 0$, which indicates given the current S/N of the data, the double-Gaussian model is not preferred statistically for the broad Hβ. With the above results and given the current data quality, we used the single-Gaussian fitting result for the broad Hβ. Later in Section 5, we show that the Hβ-based single-epoch black hole mass is consistent with the recent dynamical measurement of the black hole mass performed by I. Juodžbalis et al. (2025b).

We note that, while for NIRSpec-MSA spectroscopy, compact sources result in a spectral resolution significantly higher than the nominal spectral resolution (because the source is smaller than the shutter width), this is not the case for NIRSpec-IFU spectroscopy. This is due to the anamorphic magnification in the IFU optical path, which makes each slice of the IFU image slicer have a width of 0."1 projected on sky, while maintaining the 2-spectral pixel sampling. For a compact, unresolved source the effective resolution might still be slightly higher than the nominal spectral resolution (which is for a uniform illumination of each slice), but the effect is not as large as in the case of the MSA.

The best-fitting parameters are estimated with a Bayesian approach, where the posterior probability distribution is estimated using the Markov-Chain Monte-Carlo (MCMC) ensemble sampler – EMCEE (D. Foreman-Mackey et al. 2013) with 10 000 steps. For each of the variables, we need to define set priors for the MCMC integration. The prior on the redshift of each component is set as a truncated Gaussian distribution, centred on the systemic redshift of

---

[3] https://github.com/honzascholtz/Qubespec

[4] Available at jwst-docs website.

Table 1. Spectral measurements for Abell 2744-QSO1 based on the new BlackTHUNDER IFU R2700 spectrum extracted from the central 0.″25 of image A (shown in the bottom panel of Fig. 1) as well as the GTO reduced R100 spectrum. The velocities are measured with respect to the narrow component. The fluxes are corrected for aperture losses and are scaled to the flux of the IFU PRISM spectrum. The fluxes are not corrected for lensing magnification.

Line	v (km s^{-1})	FWHM (km s^{-1})	Flux (10^{-20} erg s^{-1} cm^{-2})	Equivalent width (Å)
R2700 spectrum				
Hβ (narrow emission)	–	< 75 (< 112 conserv.)	$12.8^{+2.6}_{-2.2}$	$7.5^{+2.5}_{-2.1}$
Hβ (broad emission)	17^{+41}_{-43}	2658^{+351}_{-292}	118^{+10}_{-8}	$72.6^{+10.1}_{-7.7}$
Hβ (absorption)	101^{+65}_{-77}	185^{+69}_{-72}	$-7.3^{+2.3}_{-2.0}$	$5.5^{+2.2}_{-1.7}$
[O III]λ5008	–	< 75 (< 112 conserv.)	$7.6^{+1.8}_{-1.8}$	$4.52^{+1.4}_{-1.2}$
R100 spectrum				
Lyα	–	unresolved	491 ± 16	155 ± 11

the galaxy with a sigma of 300 km s^{-1} and boundaries of ±1000 km s^{-1}. The prior on the intrinsic FWHM of the narrow-line component is set as a uniform distribution between 10 and 500 km s^{-1}, while the prior on the amplitude of the line is set as a uniform distribution in log-space between 0.5×rms of the spectrum and the maximum of the flux density in the spectrum.

The final best-fitting parameters and their uncertainties are calculated as the median value and the 68 per cent confidence interval of the posterior distribution. We note that all the quantities derived from R2700 spectral fitting are calculated from the posterior distribution to account for any correlated uncertainties in the spectrum between each component.

Despite the longer exposure, the high-resolution spectrum appears more noisy as a consequence of the continuum and broad Hβ being spread over many more resolution elements. The broad Hβ is well detected and its FWHM agrees with the value reported in L. J. Furtak et al. (2024). However, the grating spectrum clearly reveals a narrow component of Hβ, which is barely resolved and it cannot be deblended using the PRISM alone. Formally, the fit provides a 3σ upper limit on the width of FWHM < 75 km s^{-1} (after deconvolving for the instrumental LSF). However, in the rest of this paper, to be even more conservative, we take as an upper limit on the line width the nominal spectral resolution of the IFU at this wavelength (i.e. < 112 km s^{-1}, although the actual resolution is probably slightly better). There is also a detection of [O III]λ5008 at a significance of 4σ, which matches the velocity of the narrow component of the Hβ emission.

The profile of broad Hβ also shows the tentative detection of Hβ absorption with a FWHM of 185^{+69}_{-72} km s^{-1} and a velocity shift of 101^{+65}_{-77} km s^{-1} with respect to the narrow component, indicative of an inflow. As discussed in Introduction, the presence of Balmer absorption is not uncommon among *JWST*-discovered AGNs, and at least 20 per cent of the systems are found with this feature in Hα or Hβ when they are observed at medium to high resolution (e.g. I. Labbé et al. 2024; X. Lin et al. 2024; J. Matthee et al. 2024; B. Wang et al. 2024, 2025; I. Juodžbalis et al. 2024a; D. D. Kocevski et al. 2025; A. J. Taylor et al. 2025).

The coloured dashed lines in the bottom panel of Fig. 1 show the best fit of that portion of the spectrum with the following components: a broad component of Hβ (orange), a narrow component of Hβ and [O III] (blue), and a power-law continuum and absorption component of Hβ (green). The total fit is shown with a red dashed line. The central row of the same panel shows the χ residuals of the full fit, while the bottom row shows the residuals when not accounting for Hβ absorption. We summarize the spectral measurements for the image A of Abell 2744-QSO1 in Table 1.

5 BLACK HOLE PROPERTIES AND SCALING RELATIONS

In this section, we describe the derivations of the black hole properties in Abell 2744-QSO1 as well as the related scaling relations. We also discuss implications for the stellar mass of Abell 2744-QSO1.

5.1 Black hole mass and accretion rate

The black hole mass can be estimated assuming the local virial relations between BH mass, widths of the lines from the BLR, and the continuum or broad line luminosity (e.g. J. E. Greene & L. C. Ho 2005; M. Vestergaard & B. M. Peterson 2006; A. E. Reines & M. Volonteri 2015). It is not obvious that the same relations apply at high redshift. In particular, it has been speculated that in the super-Eddington regime (which may apply to some high-z AGN), the black hole masses may be overestimated (e.g. E. Lambrides et al. 2024; A. Lupi et al. 2024). However, recently the GRAVITY + collaboration has obtained a direct (interferometric) measurement of the BLR size and of the BH mass in a quasar at $z = 2.33$ (R. Abuter et al. 2024), which is a cosmic epoch much closer to Abell 2744-QSO1 than to the present epoch. According to their direct measurements, this black hole is accreting at a highly super-Eddington rate ($L/L_{\rm Edd} \sim 7 - 20$). Despite the high accretion rate, the BH mass estimated from the virial relation using broad Hα is consistent with the direct interferometric measurement within a factor of 2.5, well within the scatter of the virial relation (and this small offset can be mitigated even further by applying the correction factor proposed by R. Abuter et al. 2024). When using broad Hβ the agreement is worse (a factor of 5), but still not in dramatic contrast with the virial relations, taking into account their scatter and also the fact that this test case is actually a highly super-Eddington accreting black hole.

We take the FWHM of the broad component of Hβ measured in the grating spectrum. Then we estimate the luminosity of Hα by assuming a typical Hα/Hβ ratio of 3 (different from the Case B value of 2.86 due to the collisional enhancement in AGN-ionized gas, see e.g. X. Dong et al. 2008) and correcting for a visual dust extinction of $A_{\rm V} = 2.1$ estimated from our spectral fitting result in Section 6 (see Table 3) assuming a Small Magellanic Cloud (SMC) extinction curve with $R_{\rm V} = 2.505$ (K. D. Gordon et al. 2003), which has been adopted for describing dust attenuation in high-z galaxies (e.g. N. A. Reddy et al. 2015). This leads to Hα/Hβ = 7.6. As a consistency check, we measure the Balmer decrement from the MSA PRISM spectrum of image A with PPXF (M. Cappellari & E. Emsellem 2004; M. Cappellari 2017). Although the profile of Hα is only partially covered as can be seen in Fig. 1, we assumed it is Gaussian and fixed its kinematics to those of Hβ. The resulting ratio from the fit is Hα/H$\beta = 8.0 \pm 0.8$, consistent with our estimation above. We note that L. J. Furtak et al. (2024) also reported the PRISM-based Balmer decrement for images A + B + C of Abell 2744-QSO1 assuming Gaussian line profiles, which is Hα/H$\beta = 7.5 \pm 0.4$ (based on their table 1). We also correct the luminosity for a lensing magnification of $\mu_A = 5.8$ for image A. We describe the measurements of the lensing magnification in Appendix A, which are broadly consistent with measurements of L. J. Furtak et al. (2023) and L. J. Furtak et al. (2024). We then use the virial relation proposed by A. E. Reines & M. Volonteri (2015), to estimate a black hole mass of $\log{(M_{\rm BH}/{\rm M}_\odot)} = 7.59$. The formal uncertainties would be about 0.2 dex. However, we prefer to be conservative by giving an uncertainty of 0.3 dex to take into account the dispersion and uncertainties in the virial relations (e.g. L. C. Ho & M. Kim 2014).

One caveat of the above analysis is the assumed intrinsic ratio of the Balmer decrement, which can be significantly larger than 3 in LRDs (e.g. E. Lambrides et al. 2024; S.-J. Chang et al. 2025). If we simply used the Hβ luminosity to derive the BH mass following J. E. Greene & L. C. Ho (2005), and applied the dust attenuation correction based on the narrow-line attenuation of $A_{\rm V} = 0.66 \pm 0.40$ mag derived by R. Maiolino et al. (2025a), we obtained a black hole mass of $\log{(M_{\rm BH}/{\rm M}_\odot)} = 7.2 \pm 0.3$. This estimation is consistent with the value estimated above within the combined 1σ uncertainty, especially considering that the BLR is likely more dust attenuated compared to the NLR. Interestingly, I. Juodžbalis et al. (2025b) recently made a dynamical measurement of the BH mass for Abell 2744-QSO1 and obtained $\log{(M_{\rm BH}/{\rm M}_\odot)} = 7.7 \pm 0.3$, which is more consistent with our first single-epoch BH mass estimation. We refer the readers to I. Juodžbalis et al. (2025b) for further discussions on BH mass measurements in Abell 2744-QSO1.

We also estimate the bolometric luminosity of the AGN by using the scaling relations with broad emission line fluxes presented by J. Stern & A. Laor (2012); using the Hβ line (corrected as discussed above) gives $L_{\rm AGN} \approx 2.6 \times 10^{44}$ erg s^{-1}, hence implying $L/L_{\rm Edd} \approx 0.05$. As we discuss in Sections 5.2, 6, and 7, the rest-frame optical light is likely dominated by the AGN continuum. Therefore, we can also infer the bolometric luminosity from the optical continuum (L_{5100}), corrected for extinction and lensing magnification, and again adopting the scaling relation in J. Stern & A. Laor (2012), resulting in $L_{\rm AGN} \approx 1.2 \times 10^{45}$ erg s^{-1}, hence $L/L_{\rm Edd} \approx 0.24$. This is close to the estimation by L. J. Furtak et al. (2024) of $L/L_{\rm Edd} \approx 0.3$ based on MSA PRISM spectra of Abell 2744-QSO1, where they used a bolometric conversion to get $L_{\rm bol}$ from line luminosities. The two estimations of the bolometric luminosity differ by 0.66 dex, larger than the combined scatter of 0.43 dex between the bolometric conversions of J. Stern & A. Laor (2012). The difference might arise due to the intrinsic difference between the SED of Abell 2744-QSO1 and the average SED of J. Stern & A. Laor (2012)'s sample. Qualitatively, if the accretion disc in Abell 2744-QSO1 has a softer ionizing spectrum, the bolometric luminosity based on hydrogen Balmer lines that scale with the ionizing luminosity would give a lower bolometric luminosity compared to the 5100 Å continuum-based value. In addition, if the observed Balmer lines have non-negligible optical depths, the actual bolometric conversion factor would be higher than assumed. Finally, as discussed in R. Maiolino et al. (2025b), if the covering fractions of BLRs in *JWST*-selected AGN are systematically different from the low-redshift AGN, the Balmer line-based bolometric conversions would also be different. Regardless, since in either case this black hole is accreting at substantially sub-Eddington, it is unlikely that it is in the regime where the virial scaling relations are drastically affected.

5.2 A small dynamical mass of the host galaxy

As discussed above, the very small velocity dispersion inferred for the narrow component of Hβ (and for [O III]$\lambda\lambda$4960, 5008; see Table 1) indicates that the dynamical mass of the host galaxy must be quite low. In this section, we quantify this aspect starting with the conservative upper limit on the line width of FWHM<112 km s^{-1}.

In order to constrain the dynamical mass, we use the same approach as H. Übler et al. (2023) and R. Maiolino et al. (2024b) by estimating the dynamical mass through the equation

$$M_{\rm dyn} = K(n)K(q)\frac{\sigma^2 R_{\rm e}}{G}, \tag{1}$$

where $K(n) = 8.87 - 0.831n + 0.0241n^2$ with Sérsic index n, following M. Cappellari et al. (2006), $K(q) = [0.87 + 0.38{\rm e}^{-3.71(1-q)}]^2$, with axis ratio q following A. der Wel et al. (2022), and $R_{\rm e}$ is the effective radius. Given that we do not have information on q, we take it equal to one, which gives an even more conservative estimate of the upper limit on the dynamical mass; taking $q = 0$ would reduce the value by a factor of about two. As for the size, we use the measurements from L. J. Furtak et al. (2023), who report the source to be unresolved both in the rest-frame UV and optical. Therefore, we take the upper limit of 30 pc on the effective radius of the source inferred by L. J. Furtak et al. (2023). In this equation, σ is the stellar velocity dispersion. As we do not have this information, we adopt the same approach as in some previous papers (H. Übler et al. 2023; R. Maiolino et al. 2024b) of using the nebular gas velocity dispersion and applying the empirical scaling between integrated stellar and gaseous velocity dispersions derived by R. Bezanson et al. (2018) at $z \sim 1$. There are only a few systems in which this relation can be tested at higher redshift (A. C. Carnall et al. 2023; F. D'Eugenio et al. 2024; R. G. Pascalau et al. 2025), and it seems to hold, although in systems much more massive than Abell 2744-QSO1 ($M_\star \gtrsim 10^{10.5}$ M$_\odot$). The correction from the R. Bezanson et al. (2018) relation entails an increase of 0.18 dex in the velocity dispersion. As for the Sérsic index, we assume $n = 1$, as is the case for the majority of star-forming galaxies at such high redshift (e.g. K. Ormerod et al. 2024), including AGN host galaxies (R. Maiolino et al. 2024b). Since we assume an upper limit on both the velocity dispersion and the size, we obtain a very conservative upper limit on the dynamical mass, which we estimate to be $M_{\rm dyn} < 4.4 \times 10^8$ M$_\odot$. Alternatively, if we assume the system is dispersion-dominated and apply equation (A2) of T. Díaz-Santos et al. (2021), which is $M_{\rm dyn}^{\rm disp} = 3.4\sigma^2 R_{\rm e}/G$, we obtain $M_{\rm dyn}^{\rm disp} < 1.2 \times 10^8$ M$_\odot$. Interestingly, the latter upper limit would imply that the dynamical mass of the system is dominated by the black hole.[5] If we used the formal 3σ upper limit from the fit on the FWHM of the line (<75 km s^{-1}), then the upper limits on the dynamical masses would be even tighter, specifically $M_{\rm dyn} < 2.0 \times 10^8$ M$_\odot$ if using equation (1), and $M_{\rm dyn}^{\rm disp} < 5.5 \times 10^7$ M$_\odot$ if using the dispersion-dominated equation.

One caveat of the above calculations is the origin of the narrow lines, that is, whether they are dynamically influenced by the whole galaxy or only by the black hole if they are sufficiently concentrated

---

[5] We note that rotation-dominated broadening would disappear at very low inclination. However, since the inclination should be random in observations but many LRDs likely have $M_\star/M_{\rm dyn} > 1$, the low-inclination scenario seems implausible.

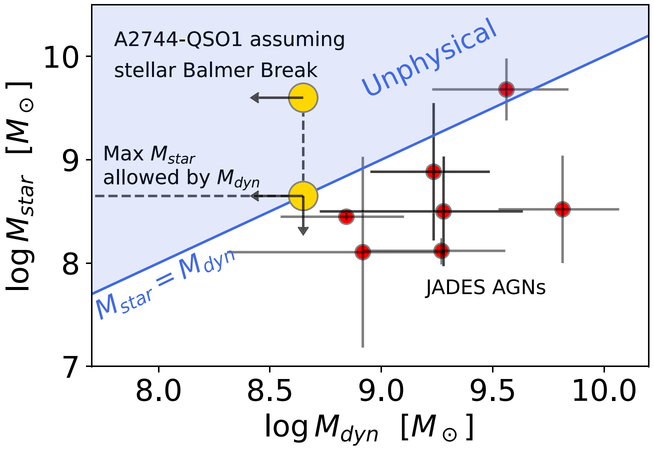

Figure 2. Comparison of stellar and dynamical masses for AGN at high-z discovered by *JWST* and observed with high spectral resolution. The shaded region is the 'unphysical' area where the stellar mass is larger than the dynamical mass. Red small symbols are objects in the JADES sample presented in R. Maiolino et al. (2024b) (updated with new estimated stellar masses in I. Juodžbalis et al. 2025a). The upper golden symbol shows the dynamical mass estimated by the BlackTHUNDER high resolution spectrum of Abell2744-QSO1, where the stellar mass is the one inferred by Y. Ma et al. (2025) assuming that the optical continuum and Balmer break are entirely dominated by stellar light; clearly this scenario leads to an unphysically high stellar mass, about an order of magnitude larger than the dynamical mass. The maximum stellar mass allowed by the dynamical mass is shown with the lower golden symbol.

spatially. Interestingly, as recently pointed out by I. Juodžbalis et al. (2025b) and R. Maiolino et al. (2025a), the narrow lines in Abell 2744-QSO1 are actually spatially resolved in NIRSpec IFU observations, whose dynamics were subsequently modelled by I. Juodžbalis et al. (2025b) using the code MOKA3D (C. Marconcini et al. 2023). I. Juodžbalis et al. (2025b) found that the kinematics of narrow Hα are best modelled by a point source-like mass of 5×10^7 M$_\odot$, likely dominated by the central black hole. While an extended exponential disc component is not preferred by the data, enforcing such a component would give an upper limit on the extended dynamical mass of 2×10^7 M$_\odot$, much smaller than our dynamical mass estimate. Therefore, no matter whether we used the rough dynamical mass estimate by assuming an unresolved stellar component and stellar velocity dispersion scaled from the gas velocity dispersion, or took the more sophisticated dynamical modelling result of I. Juodžbalis et al. (2025b), we obtained relatively small dynamical mass upper limits in a range of $10^{7.3-8.6}$ M$_\odot$.

We note that the derived dynamical mass, even taking the most conservative upper limit, is an order of magnitude lower than the stellar mass inferred by Y. Ma et al. (2025) when assuming that the optical continuum and Balmer break are entirely dominated by stellar light, which is 4×10^9 M$_\odot$.[6] This discrepancy is illustrated visually in Fig. 2. This result highlights that most of the optical light, as well as the Balmer break, cannot have a stellar origin. Even our most conservative upper limit on the dynamical mass is only 10 per cent of the stellar mass inferred from stellar dominated Balmer break and optical continuum. Our finding indicates that no more than 10 per cent of the optical light originates from stars. In Section 6, we further illustrate that an AGN continuum and dense gas along the line of sight (LOS) can explain well the shape of the optical continuum and, in particular, the Balmer break, hence greatly alleviating the issue of the high stellar mass and extremely high stellar densities inferred when assuming a stellar origin of the Balmer break.

5.3 An overmassive black hole

The upper limits on the dynamical mass also translate into a tight upper limit on the stellar mass. These upper limits can be compared with the black hole mass inferred from the virial relations and with the local scaling relations between black hole mass and galaxy properties.

The left panel of Fig. 3 shows the relationship between BH mass and host galaxy stellar mass. Local galaxies (blue points) are taken from A. E. Reines & M. Volonteri (2015); these are disc galaxies, hence with Sérsic index n comparable to the host galaxies of high-z AGN; additionally, the black hole masses in this sample have been measured using the same virial relations as adopted in our work, hence are fully consistent. We also show the galaxies reported in J. E. Greene, J. Strader & L. C. Ho (2020), which also have Sérsic index $n \sim 1$, although in this case the BH masses are estimated with a different calibration. The black solid line and blue solid line show the relations inferred from those two local studies, and the grey and blue shaded regions show their dispersions. We also show the relation obtained by M. C. Bentz & E. Manne-Nicholas (2018) for local AGN with reverberation mapping (orange line and shaded region), mostly in disc galaxies. For completeness we also show with a dot-dashed black line the J. Kormendy & L. C. Ho (2013) $M_{\rm BH}$–$M_{\rm spheroid}$ relation for early-type galaxies, but we caution that this is inadequate as for the vast majority of high-z galaxies, including AGN hosts, the stellar light has a disc-like profile. The red points are black hole and host galaxy stellar mass measurements from various *JWST* studies at $z > 4$ (A. C. Carnall et al. 2023; X. Ding et al. 2023; A. D. Goulding et al. 2023; Y. Harikane et al. 2023; D. D. Kocevski et al. 2023; V. Kokorev et al. 2023; H. Übler et al. 2023; Á. Bogdán et al. 2024; M. A. Stone et al. 2024; B. Wang et al. 2024; M. Yue et al. 2024a; R. Maiolino et al. 2024b; B. Trefoloni et al. 2025; I. Juodžbalis et al. 2025a). Note that candidate dual/merging BHs are connected with red dashed lines (R. Maiolino et al. 2024b). Most of the high-z AGN discovered by *JWST* are overmassive relative to the local $M_{\rm BH}$–$M_\star$ relations, by even orders of magnitude. This was already highlighted by previous studies (e.g. Y. Harikane et al. 2023; H. Übler et al. 2023; I. Juodžbalis et al. 2024b; R. Maiolino et al. 2024b; M. A. Marshall et al. 2025). The golden large symbol shows the location of Abell 2744-QSO1. As no solid detection of the stellar light has been obtained yet, here we use the dynamical mass (based on the conservative upper limit on the line width) as a conservative upper limit on the stellar mass. Abell 2744-QSO1 deviates from the local relations by orders of magnitude. This was already pointed out by L. J. Furtak et al. (2024), by setting an upper limit on the stellar mass by assuming the case that all observed optical light is associated with stellar emission. Here we confirm their finding but in this case using the dynamical mass as an independent constraint on the stellar mass.

The right panel of Fig. 3 shows the $M_{\rm BH}$–$M_{\rm dyn}$ relations. In this case, for local galaxies we use the early-type sample of J. Kormendy & L. C. Ho (2013) (blue points and dot-dashed best-fitting relation), where we use their stellar masses as a proxy of the dynamical masses. The justification is that these early-type galaxies have very little gas content and the total dynamical mass is nearly

---

[6] It is worth noting that the fiducial fit by Y. Ma et al. (2025) also includes contributions from AGN to the optical continuum. Even in this case, the inferred stellar mass is $\sim 4 \times 10^9$ M$_\odot$.

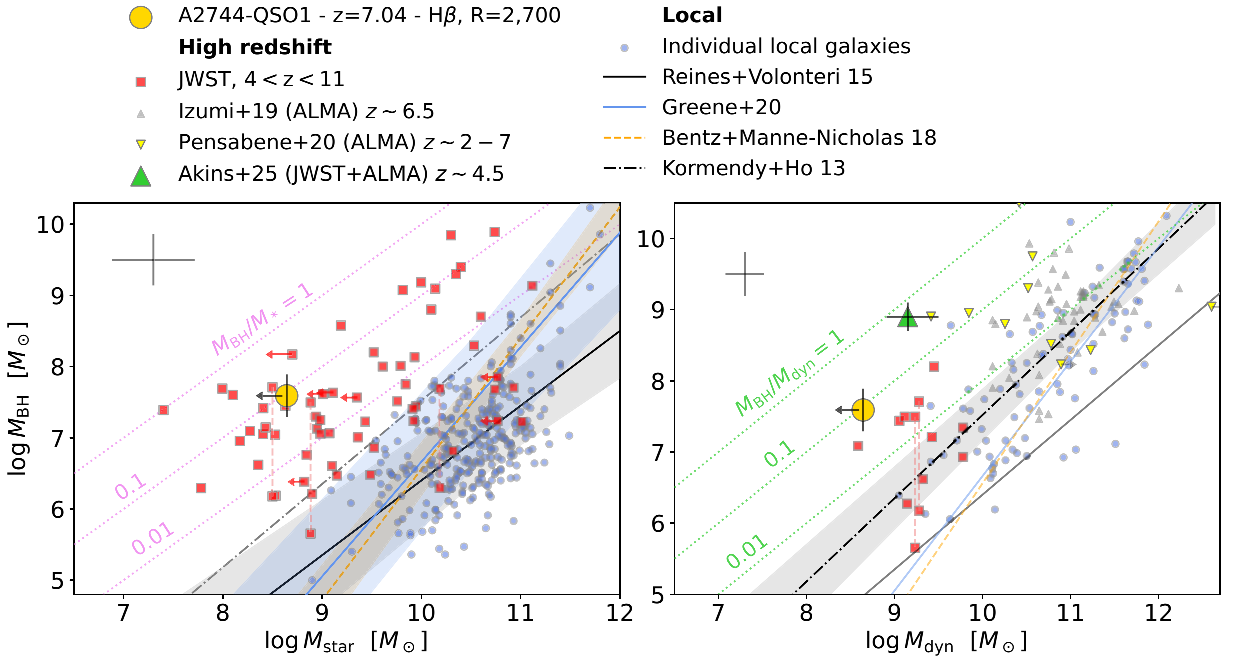

Figure 3. Scaling relations between black holes and their host galaxies, specifically BH mass versus galaxy stellar mass (left) and versus galaxy dynamical mass (right). The small blue symbols show local galaxies, and the straight lines and shaded regions illustrate the best-fitting local scaling relations (see the text for details). The red squares show AGN at 4<z<11 for which the black hole mass and host galaxy stellar/dynamical mass has been measured with *JWST* data, as reported by Á. Bogdán et al. (2024); A. C. Carnall et al. (2023); X. Ding et al. (2023); A. D. Goulding et al. (2023); Y. Harikane et al. (2023); D. D. Kocevski et al. (2023); V. Kokorev et al. (2023); H. Übler et al. (2023); M. A. Stone et al. (2024); B. Wang et al. (2024); M. Yue et al. (2024a); R. Maiolino et al. (2024b); B. Trefoloni et al. (2025); I. Juodžbalis et al. (2025a). The mean uncertainties of masses are indicated by the black cross on the top left location of each panel. Additionally, we plot high-z sources from T. Izumi et al. (2019); A. Pensabene et al. (2020); H. B. Akins et al. (2025a). The golden circles show Abell2744-QSO1 for which we have taken the upper limit on the host galaxy dynamical mass as conservative upper limit on the stellar mass. The black hole in Abell2744-QSO1 is clearly overmassive both in terms of stellar and dynamical mass, when compared with the local relations.

coincident with the spheroidal stellar mass component.[7] However, for completeness we also show the stellar relation for the disc samples (solid black and solid blue lines), although these are inadequate for assessing the dynamical masses, given the large amount of gas and also dark matter expected in these early galaxies. The red points shown here are AGN at $z > 4$ discovered by *JWST*, whose dynamical masses could be estimated based on high spectral resolution data (H. Übler et al. 2023; R. Maiolino et al. 2024b). In this case, the high-z BHs are closer to the local relation. This is partly due to the fact that the local J. Kormendy & L. C. Ho (2013) relation is higher than those by A. E. Reines & M. Volonteri (2015) and J. E. Greene et al. (2020), although, given that the J. Kormendy & L. C. Ho (2013) relation is based on direct dynamical measurements of BH masses, it is likely biased high (i.e. for black holes massive enough that their sphere of influence can be resolved). Also, black holes in non-classical bulges are excluded from the fit of J. Kormendy & L. C. Ho (2013). However, regardless of the adopted local relation and its potential biases, most high-z AGN do not have black holes masses that are in excess of 0.1 times the dynamical mass, which instead is the case for the stellar masses. One exception is the LRD with $M_{\rm dyn}$ measured by H. B. Akins et al. (2025a) with the tentative detection of [C I](2-1) using ALMA, where $M_{\rm BH}/M_{\rm dyn}$ is close to 1, although [C I](2-1) might be spatially offset from the centre of the NIRCam image. Regarding Abell2744-QSO1 (large golden symbol), the upper limit on its dynamical mass is lower than most *JWST* AGN and it indicates that its black hole mass is heavily overmassive also relative the black hole-dynamical mass relation. As already pointed out in the previous section, using the formal 3σ upper limit on the width of the narrow Hβ, or adopting the dispersion-dominated scenario, would yield an even lower upper limit on the dynamical mass, approaching the mass of the black hole itself. In fact, the recent work of I. Juodžbalis et al. (2025b) has shown that the dynamical mass of QSO1 is indeed dominated by the central black hole.

For other *JWST*-discovered AGN the overmassive nature on the $M_{\rm BH}$–$M_\star$ relation and being more aligned with the $M_{\rm BH}$–$M_{\rm dyn}$ relation could have been interpreted in terms of the host galaxy having the adequate baryon mass, but where most of the gas had been inefficient in forming stars. Yet, in the case of Abell2744-QSO1 the black hole is overmassive in all regards, also relative to the dynamical mass of the host galaxy.

6 A BALMER BREAK ORIGINATING FROM DENSE GAS ABSORPTION

As discussed in Section 5.2, interpreting the optical continuum and the Balmer break with a stellar origin would result in a stellar mass that is an order of magnitude larger than the dynamical mass. Additionally, the implied stellar density would be far larger than any other system seen at lower redshift. However, the growing number of *JWST*-discovered AGN showing either Hα and Hβ absorption (visible only in medium- and high-resolution spectra; I. Labbé et al.

---

[7] We note that below $\log(M_\star/{\rm M}_\odot) = 10.5$, the dark-matter fraction decreases with decreasing stellar mass (M. Cappellari et al. 2013; E. Toloba et al. 2014; F. S. Eftekhari et al. 2022). This would make the true $M_{\rm BH}$–$M_{\rm dyn}$ relation steeper, making Abell 2744-QSO1even more overmassive.

2024; X. Lin et al. 2024; J. Matthee et al. 2024; I. Juodžbalis et al. 2024a; D. D. Kocevski et al. 2025; B. Wang et al. 2025) indicates that many (probably most) of these systems require extremely dense gas ($n_{\rm H} > 10^8$ cm^{-3}) with high column densities ($N_{\rm H} > 10^{21}$ cm^{-2}) along the LOS, possibly associated with the BLR clouds, which is the only way to keep the short-lived $n = 2$ level of hydrogen populated and subsequently result into the observed Balmer absorption (I. Juodžbalis et al. 2024a). As shown in Fig. 1, Abell2744-QSO1 has a tentative detection of Hβ absorption as well. K. Inayoshi & R. Maiolino (2025) pointed out that Hα and/or Hβ absorption must also necessarily come with absorption of higher Balmer orders and including a Balmer break.

In this section, we explore whether the Balmer break observed in Abell 2744-QSO1, as well as its other spectral properties, can be explained in the scenario where the optical light is dominated by an AGN continuum with dense absorbing gas along the line of sight. As we mentioned in Section 2, the background subtraction of image B is likely problematic. Thus, we used the spectrum from the combined images of A and C obtained through the GTO reduction as the fiducial spectrum. Still, we checked the results based on the spectrum from the combined images of A, B, and C images reduced by L. J. Furtak et al. (2024), as well as the integrated IFU spectrum from image A observed in BlackTHUNDER, as detailed later.

6.1 Balmer break fitting: method

We formulate our spectral model as follows

$$F_{\lambda;\rm model} = b\lambda^m + 10^{-0.4A_\lambda}(F^{\rm att.}_{\lambda;\rm Acc.\ disc} + C_f F_{\lambda;\rm neb.\ BLR}) + F_{\lambda;\rm neb.\ narrow}, \tag{2}$$

based on a series of physically motivated assumptions. In the equation above, $F_{\lambda;\rm Acc.\ disc}$ represents the flux of the accretion disc attenuated by a slab of dust-free gas in the BLR, $C_f F_{\lambda;\rm neb.\ BLR}$ represents the nebular emission from the BLR observed along the LOS, $F_{\lambda;\rm neb.\ narrow}$ represents the nebular emission from the narrow-line component, $10^{-0.4A_\lambda}$ is a dust attenuation factor for the BLR emission, and $b\lambda^m$ is a power-law continuum. We explain in detail the physical meaning of each term below.

First, we assume the AGN emission that dominates the optical spectrum has two major components, which represent the attenuated continuum emission and the nebular emission, respectively. The first component, $F_{\lambda;\rm Acc.\ disc}$, originates in the AGN accretion disc and is attenuated by dense and dust-free gas along the LOS. For the accretion disc emission, we used theoretical SEDs parametrized by the black hole mass, $M_{\rm BH}$, and the Eddington ratio, $\lambda_{\rm Edd}$, computed by E. Pezzulli et al. (2017). According to the estimation of L. J. Furtak et al. (2024), Abell 2744-QSO1 has a black hole mass of $M_{\rm BH} = 4^{+2}_{-1} \times 10^7$ M$_\odot$ and an Eddington ratio of $\lambda_{\rm Edd} = L_{\rm bol}/L_{\rm Edd} \sim 0.3$. In comparison, our estimations involving the new BlackTHUNDER observations give $M_{\rm BH} = 4^{+4}_{-2} \times 10^7$ M$_\odot$ and $\lambda_{\rm Edd} = L_{\rm bol}/L_{\rm Edd} \sim 0.05 - 0.24$ (see Section 5.1). We note that Abell 2744-QSO1 shows no detection of He IIλ4686 in the optical (L. J. Furtak et al. 2024), which might imply the lack of high energy photons with $h\nu > 54$ eV (although low He IIλ4686/Hβ down to 0.1 and lower has also been observed in local AGN, e.g. D. E. Vanden Berk et al. 2001; G. Tozzi et al. 2023). As recently suggested by E. Lambrides et al. (2024), the lack of high ionization lines in *JWST*-selected Type 1 AGN might imply near-to-super Eddington accretion and the Eddington ratio might have been underestimated in these systems. Therefore, we considered theoretical SEDs with $M_{\rm BH} = 10^7$ M$_\odot$ and $\lambda_{\rm Edd} = 0.1, 1, 10$ and compared their fitting results. In the sub-Eddington regime ($10^{-2} \lesssim \lambda_{\rm Edd} \leq 1$), the SED is computed assuming the standard disc model with a geometrically thin and optically thick disc (N. I. Shakura & R. A. Sunyaev 1973). In the super-Eddington regime, the accretion disc becomes geometrically thick due to inefficient radiative cooling, where instead energy advection via photon trapping dominates and suppresses the emergent radiation flux from the innermost disc region (M. A. Abramowicz et al. 1988). E. Pezzulli et al. (2017) accounted for the photon trapping effect on the SED by removing the emergent radiation flux within the characteristic radius, resulting in a softer UV SED. However, the emission within the photon-trapping radius is not entirely suppressed in super-Eddington accretion. In fact, the UV SED could become harder compared to the sub-Eddington case due to contributions from the hotter optically thick regions of the accretion disc extended within the innermost stable circular orbit (e.g. A. Kubota & C. Done 2019; K. Inayoshi et al. 2025; however, see F. Pacucci & R. Narayan 2024 for a different model). We discuss the effect of different SEDs later in this section and in Appendix B.

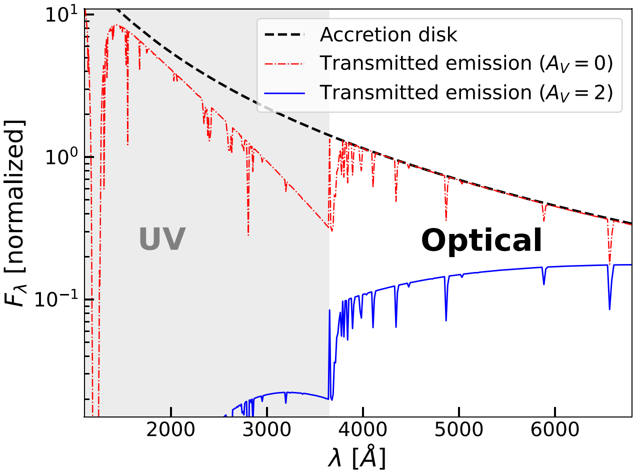

Figure 4. Example of an AGN accretion disc emission with $M_{\rm BH} = 10^7$ M$_\odot$ and $\lambda_{\rm Edd} = 0.1$ attenuated by a slab of gas with $n_{\rm H} = 10^{10}$ cm^{-3}, $N_{\rm H} = 10^{23}$ cm^{-2}, $U = 10^{-1.5}$, and $v_{\rm turb} = 120$ km s^{-1} (definitions of parameters given in Section 6.2.1). The simulation is performed with CLOUDY. The dashed line is the intrinsic continuum normalized at $\lambda = 4260$ Å. The dash-dotted red line is the dust-free attenuated continuum, which exhibits prominent absorption features including Balmer lines and the Balmer break. The solid blue line is the attenuated continuum further obscured by a dust screen with $A_{\rm V} = 2$, which shows an uprising optical continuum in addition to the Balmer break resembling the rest-frame optical part of LRDs. The spike at the UV-optical interface is an artefact caused by the limited number of resolved energy levels of hydrogen.

Fig. 4 shows the shape of the accretion disc continuum with $M_{\rm BH} = 10^7$ M$_\odot$ and $\lambda_{\rm Edd} = 0.1$ in the UV-to-optical regime. We adopt this value as the baseline, given that the estimated accretion rate is sub-Eddington and in the range $\lambda_{\rm Edd} \sim 0.05 - 0.24$.

To obtain the gas-absorbed SED, we passed the intrinsic disc emission through a slab of gas with high densities and column densities. This calculation is done with the photoionization code CLOUDY (v17.03, G. J. Ferland et al. 2017). As already shown by K. Inayoshi & R. Maiolino (2025), at densities of $n_{\rm H} \sim 10^{9-11}$ cm^{-3}, collisional excitation efficiently populates neutral hydrogen to the excited state of $n = 2$, leading to a strong Balmer break. At such high densities, the gas likely originates from the BLR or its proximity (I. Juodžbalis et al. 2024a). Therefore, we did not consider dust attenuation within the dense gas, as the BLR clouds are usually within

Table 2. Input parameters for CLOUDY simulations of BLR absorption and emission. The fiducial parameters are shown in the bold font.

Parameter	Values
SED	$\boldsymbol{M}_{\rm BH} = \mathbf{10^7}$ $\mathrm{M}_\odot$, $\lambda_{\rm Edd} = \mathbf{0.1}$, 1, 10 (E. Pezzulli et al. 2017)
$\log(U)$	-2.5, -2.25, -2.0, -1.75, $\mathbf{-1.5}$, -1.25, -1.0
$\log(Z/Z_\odot)$	-1
Solar abundance set	N. Grevesse et al. (2010) solar abundance set
$\log(n_{\rm H}/{\rm cm^{-3}})$	8, 8.5, 9, 9.5, **10**, 10.5, 11, 11.5, 12
$\log(N_{\rm H}/{\rm cm^{-2}})$	21, 21.5, 22, 22.5, 23, 23.5, **24**
$v_{\rm turb}$ (km s^{-1})	20, 40, 60, 80, 100, **120**
Dust	No dust
Resolved hydrogen energy levels	50
Atomic data set	CHIANTI (v7, K. P. Dere et al. 1997; E. Landi et al. 2013)

the dust sublimation radius (H. Netzer & A. Laor 1993; C. M. Gaskell 2009; for discussions of BLR models with dust, see e.g. G. A. Shields et al. 2010). In Fig. 4, we show a continuum attenuated by a slab of gas with $n_{\rm H} = 10^{10}$ cm^{-3} and $N_{\rm H} = 10^{23}$ cm^{-2}. One can see a clear Balmer break starting around the Balmer limit of 3646 Å, as well as a series of absorption features underlying the locations of Balmer lines. Another notable feature is a spike of emission near the Balmer limit, which is also seen in the models of K. Inayoshi & R. Maiolino (2025). This spike is due to the fact that not all energy levels of hydrogen are resolved in the simulation. To save computational time, we include the first 50 energy levels from the ground level in the calculation. We note that the remaining spike does not have any significant impact on the fitting result. We also considered dust attenuation external to the BLR, which is described by the attenuation factor $10^{-0.4A_\lambda}$ (note that potentially some of this dust obscuration can also come from some dust content in self-shielded clouds in the outer BLR, as suggested by G. A. Shields et al. 2010; regardless, the dust location would not affect the fitting results). The extinction curve is assumed to be an SMC bar extinction curve with $R_V = 2.505$ (K. D. Gordon et al. 2003). Recently, Y. Ma et al. (2025) suggested that an unusually steep dust attenuation law is required to fit the spectrum of Abell 2744-QSO1. However, as we show later, the SMC extinction curve is sufficient to provide a sensible fit with the framework adopted here. In Fig. 4, we show an example where the gas-obscured continuum is attenuated by a dust screen with $A_V = 2$, which leads to a rising continuum in the optical resembling the optical spectrum of LRDs (see e.g. D. D. Kocevski et al. 2025).

In addition to the continuum emission, we considered the nebular emission from the BLR, $F_{\lambda;{\rm neb.\ BLR}}$, including the nebular continuum and emission lines. The nebular emission is also computed with CLOUDY with the same physical condition as the continuum absorbing gas. We considered a wide range of model parameters as summarized in Table 2. The effects of various model parameters and how we narrowed down the ranges for these parameters are described in the next section. The nebular emission is multiplied by a covering fraction, C_f, before being added to the continuum emission as the total emission from the BLR. The covering fraction is defined as $C_f \equiv \Omega/4\pi$, where Ω is the solid angle of the BLR clouds with respect to the central accretion disc. This parameter is included out of a geometrical consideration to describe how much of the nebular emission is produced and captured along the LOS (see D. E. Osterbrock & G. J. Ferland 2006 and section 16.44 of Hazy 1, C17[8]). Again, we considered the BLR nebular emission is further processed by external dust extinction with the same factor of $10^{-0.4A_\lambda}$ as the continuum emission.

Then, we assume the UV continuum is a featureless power law, representing either an AGN SED (e.g. scattered light by extended gas) or a stellar SED with young stellar populations. For the moment, we do not consider the case where the physical process generating the UV continuum produces a Balmer break, for which the reason is justified as the following. As shown by Y. Ma et al. (2025), assuming the UV continuum has a Balmer break and has a stellar origin, the AGN component needs to be sub-dominant over the full UV-to-optical range. This leads to three difficulties, which are the high intrinsic equivalent widths for broad emission lines (see e.g. R. Maiolino et al. 2025b), an extremely high stellar mass density (not observed in any lower redshift galaxy), and an unusual dust attenuation law (Y. Ma et al. 2025). Assuming the UV continuum has a Balmer break but has an AGN origin also faces difficulties, which are discussed later in Section 6.2.3. In Section 6.2.3, we also discuss in detail the possible physical origin of the UV continuum based on the observed Lyα damping wing. However, at the level of the fitting, as this is not the focus of the paper, we remain agnostic on the origin of the UV continuum and, as said, we simply empirically fit it with a power law.

Finally, for the narrow-line emission, we only include Hβ and Hγ as no other lines are significantly detected in the PRISM spectrum. While L. J. Furtak et al. (2024) claimed detection of other lines in the PRISM spectrum such as [O III]$\lambda\lambda$4960, 5008 and S IIλ6347, as shown in Section 2, presence of these lines depends on data reduction and thus we do not consider them as confirmed detections. The flux of the narrow Hβ in the model is fixed to that of the broad Hβ by the observed ratio of H$\beta_{\rm narrow}$/H$\beta_{\rm broad}$ in Table 1. Then the flux of the narrow Hγ is obtained by multiplying the flux of the narrow Hβ by a Case B factor of 0.469 (B. T. Draine 2011). Since the narrow-line emission is significantly weaker than the broad-line emission, whether we include the dust attenuation for the narrow-line emission or not has little impact on the fitting results.

We used equation (2) to describe the spectral range of $\lambda = 1600 - 6400$ Å to avoid the proximity of the Lyα damping wing and the partially covered Hα line. Later in Section 6.2.3, we extend the spectral range to $\lambda = 1250 - 6400$ Å to fit part of the Lyα damping wing. Before fitting, we convolve the BLR nebular emission with a FWHM measured from the broad Hβ, which is 2658 km s^{-1} (the intrinsic FWHM of the CLOUDY models is negligible compared to the value). We did not convolve the attenuated continuum emission or the narrow-line emission with the measured widths, which are much narrower compared to the LSFs of the PRISM spectrum ($\sim 1 - 3 \times 10^3$ km s^{-1}). We then convolved the full model with

---

[8] https://gitlab.nublado.org/cloudy/cloudy/-/wikis/home

the LSF for point sources observed with the MSA given by A. Graaff et al. (2024), and resampled the model to the wavelength grid of the PRISM spectrum using the PYTHON function SPECTRES (A. C. Carnall 2017).

There are a total of five free parameters to be fitted once the parameters for the CLOUDY simulations are fixed. These parameters are the normalization of the power law, b, the power-law slope, m, the covering fraction, C_f [$\in (0, 1)$], the magnitude of the V-band attenuation, A_V, and the overall normalization of the BLR component, $f_{\rm BLR}$ (the normalization of the narrow-line component has been tied to the BLR component based on the flux ratio in Table 1). We used the Markov chain Monte Carlo (MCMC) method with EMCEE (D. Foreman-Mackey et al. 2013) to estimate the best-fitting values of the parameters. We set the likelihood function to

$$\log L_{\rm likelihood} = \sum_{\lambda} -0.5(F_{\lambda;{\rm obs.}} - F_{\lambda;{\rm model}})^2/\sigma_{\lambda}^2, \quad (3)$$

and assumed flat priors for all model parameters. We ran 5000 steps of MCMC for each fit and took the medians of the posterior distributions as the best-fitting parameters. The 1σ uncertainties are estimated using the 68 per cent confidence interval of the posterior distributions.

6.2 Balmer break fitting: results

In this section, we present our fitting results. As we mentioned in the previous section, there are a total of five free parameters we need to constrain in addition to the CLOUDY parameters. While the CLOUDY simulations cover a large parameter space, as shown by K. Inayoshi & R. Maiolino (2025), the Balmer break is enhanced in certain regimes of the parameter space. Therefore, we divide the section into two major parts. In the first part, we re-examine the dependencies of the Balmer break and Balmer absorption on various CLOUDY parameters, similar to what K. Inayoshi & R. Maiolino (2025) did. In the second part, we perform a series of full spectral fits and check the effects of other model parameters in equation (2).

6.2.1 *Effects of different photoionization parameters*

In Table 2, we list a series of photoionization parameters to vary for CLOUDY models, including the shape of the SED, the ionization parameter, $U \equiv \Phi_0/n_{\rm H}c$ (Φ_0 is the hydrogen ionizing photon flux, $n_{\rm H}$ is the hydrogen density, and c is the speed of light), the hydrogen density, $n_{\rm H}$, the hydrogen column density, $N_{\rm H}$, and the microturbulence velocity, $v_{\rm turb}$. We set the metallicity to 0.1 solar, as no strong constraints from nebular emission lines are available (L. J. Furtak et al. 2024). Regardless, the metallicity has little impact on our results as we focus on spectral features produced by hydrogen. Additionally, we considered no dust in our simulations, as expected for typical BLRs that lie within the dust sublimation radius (H. Netzer & A. Laor 1993; C. M. Gaskell 2009). The possible presence of dust surviving in the outer (possibly self-shielded) parts of the BLR (G. A. Shields et al. 2010), is accounted for by the dusty-screen part of the model, whose location does not affect the results.

First of all, we explore the effects of varying parameters other than the SED. Fig. 5 shows the model-predicted strength of the Balmer break as well as the Hβ absorption as a function of different parameters, where the SED is fixed to the one with $M_{\rm BH} = 10^7$ M$_{\odot}$ and $\lambda_{\rm Edd} = 0.1$ that best match our measurements in Section 5.1. Here we characterize the strength of the Balmer break using the ratio between the flux densities at 4050 Å and 3640 Å to avoid any line features as well as the artificial spike seen in Fig. 4. The strength of the Hβ absorption is simply represented by its equivalent width (EW) with respect to the continuum. In each panel, we vary only one parameter while keeping all the other parameters fixed to the values shown on the top.

The top left panel of Fig. 5 shows the effects of $n_{\rm H}$ once the other parameters are fixed. The Balmer break is much more sensitive to the variation in $n_{\rm H}$ compared to the Hβ absorption. Overall both the break and the absorption reach the maximum values around $n_{\rm H} = 10^{10}$ cm^{-3}. The same effect was noted by K. Inayoshi & R. Maiolino (2025) and is explained by the strength of the collisional excitation. At very low densities, the collisional excitation of hydrogen is not strong enough to populate the atoms to their excited states. At very high densities, the collisional excitation is so strong that a considerable fraction of hydrogen is populated at $n > 2$ levels. Both of the above tend to reduce the strength of the Balmer absorption, leading to the peak we see at $n_{\rm H} \approx 10^{10}$ cm^{-3}. While this density produces the strongest Balmer break, it should be noted that a Balmer break is expected at any density higher than 10^9 cm^{-3}.

The top right panel of Fig. 5 shows the effect of $N_{\rm H}$. Both the Balmer break and the Hβ absorption are enhanced with increasing $N_{\rm H}$. The only difference is that the Balmer break starts to increase with $N_{\rm H}$ faster at $N_{\rm H} \gtrsim 10^{23}$ cm^{-2}, whereas the Hβ absorption starts to saturate at $N_{\rm H} \gtrsim 10^{22-23}$ cm^{-2}. Increasing $N_{\rm H}$ strengthens Lyα trapping that helps to populate hydrogen to $n = 2$, thereby leading to the observed trends (P. B. Hall 2007; I. Juodžbalis et al. 2024a).

The bottom left panel of Fig. 5 shows the effect of the ionization parameter U. Increasing U significantly enhances the Balmer break and slightly enhances the Balmer absorption. This can be understood as the fact that the bound-free absorption is enhanced with the increasing ionizing flux.

Finally, the bottom right panel shows the effect of the microturbulence velocity, $v_{\rm turb}$. The microturbulence velocity describes the relative motions of gas within the line emitting/absorbing regions and is related to the observed velocity dispersion via $v_{\rm turb} = \sqrt{2}\sigma$. While the physical origin of the microturbulence remains debated, mechanisms such as disc winds and magnetohydrodynamic (MHD) waves have been proposed to explain the formation of the turbulence (M. Bottorff et al. 2000; M. C. Bottorff & G. J. Ferland 2000). It has been shown by many previous modelling works that to reproduce the nebular emission of BLRs, a microturbulence velocity of $v_{\rm turb} \sim 100$ km s^{-1} is needed, which can enhance line escaping as well as continuum pumping (e.g. J. A. Baldwin et al. 2004; G. J. Ferland et al. 2009; A. Sarkar et al. 2021). In our case, $v_{\rm turb}$ clearly enhances the Hβ absorption but only moderately enhances the Balmer break. The enhancement of EW(Hβ) can be understood as the strengthened continuum absorption due to a broader wing of the absorption profile boosted by the velocity dispersion (I. Juodžbalis et al. 2024a). More specifically, the absorption profile around Hβ can be written in the analytical form of

$$f_{\lambda} \propto \exp\left[-\tau_0 \, e^{-(1-\lambda/\lambda_0)^2 c^2/(v_{\rm therm}^2 + v_{\rm turb}^2)}\right], \quad (4)$$

where τ_0 is the optical depth at the line centre (which depends inversely on the line width, see B. T. Draine 2011), λ_0 is the central wavelength, c is the speed of light, $v_{\rm therm} = \sqrt{2k_{\rm B}T_{\rm e}/m_{\rm H}}$ is the thermal broadening (typically 10–20 km s^{-1}), and $v_{\rm turb}$ is the turbulent broadening. This equation indicates that the absorption profile is broadened at higher turbulence, leading to a larger equivalent width. We note that K. Inayoshi & R. Maiolino (2025) did not consider $v_{\rm turb}$ in their CLOUDY simulations, which actually lead to an important implication on the smoothness of the Balmer break, as we discuss later in this section.

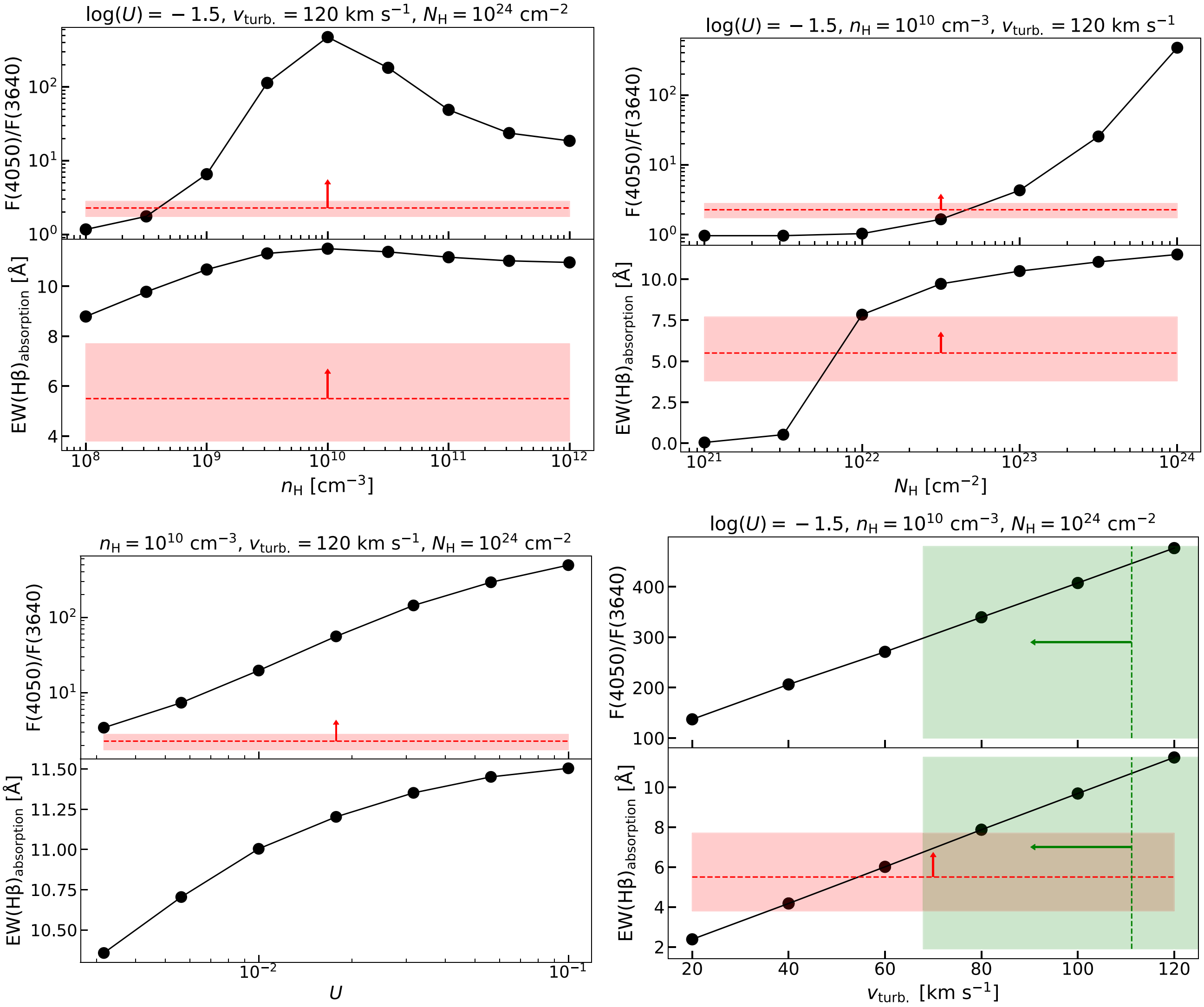

Figure 5. Dependencies of the strength of the Balmer break and the equivalent width of the Hβ absorption on various model parameters for an AGN continuum attenuated by a slab of dust-free gas computed with CLOUDY. From top left to bottom right, we vary the hydrogen density, $n_{\rm H}$, the hydrogen column density, $N_{\rm H}$, the ionization parameter, U, and the microturbulence velocity, $v_{\rm turb}$, respectively. The horizontal red dashed lines and shaded regions represent lower limits and their 68 per cent confidence intervals constrained by the observed spectra of Abell 2744-QSO1. The vertical green dashed lines and shaded regions represent the upper limit on $v_{\rm turb}$ and its 68 per cent confidence interval. For the strength of the Balmer break, the constraint is a lower limit since the intrinsic break is lifted by the extension of the UV continuum. Similarly, for EW(Hβ), the constraint is a lower limit since the optical tail the UV spectrum is not subtracted. The upper limit on $v_{\rm turb}$ is obtained from the measured width of the Hβ absorption. The inclusion of the Hβ absorption tightens the constraints on the microturbulence velocity, $v_{\rm turb}$, assuming it originates in the same absorber that produces the Balmer break.

Besides the model dependencies, we also show the apparent strengths of the Balmer break and Hβ absorption measured from the spectra of Abell 2744-QSO1 in Fig. 4. These measurements are shown as lower or upper limits with uncertainties. The Balmer break of Abell 2744-QSO1 is measured using the same definition as adopted in the model [i.e. $F(4050)/F(3640)$] and has a value of 2.28.[9] However, since we have not separated the optical continuum from the UV continuum for Abell 2744-QSO1 at this stage, the unremoved UV continuum tends to lower this ratio. Thus, we considered the measured $F(4050)/F(3640)$ as a lower limit, as shown in Fig. 4. One can see this lower limit already sets some rough constraints on CLOUDY model parameters, requiring $n_{\rm H} > 10^{8.5}$ cm^{-3} and $N_{\rm H} > 10^{22.5}$ cm^{-2}, although this is subject to the choice of U. I. Juodžbalis et al. (2024a) found that the ionization parameter of the Balmer-line absorbing gas in another *JWST*-selected AGN at $z = 2.26$ is $U \sim 10^{-1.8} - 10^{-2.1}$ based on the detection of both Balmer and He I absorption lines. We chose a slightly higher value of $U \sim 10^{-1.5}$ to start with. Overall the choice of U within a range of $10^{-2} - 10^{-1.5}$ does not impact our conclusions, as we show in Appendix B. Furthermore, we show the measurement of EW(Hβ) in absorption from the BlackTHUNDER spectrum together with the 1σ uncertainty, which is $5.5^{+2.2}_{-1.7}$ Å. Again, we interpret this measurement as a lower limit, since the optical tail of the UV continuum should lower the apparent EW(Hβ). The lower limit on EW(Hβ) sets a

---

[9] As a comparison, B. Wang et al. (2024) reported break strengths for three LRDs in a range of 1.96–2.44, although they adopted a slightly different definition using spectral windows centred at wavelengths similar to those we adopted.

rough constraint on the turbulence, requiring $v_{\rm turb} \gtrsim 60$ km s^{-1}. Meanwhile, the measured width of the absorption sets an upper limit on the turbulence velocity, $v_{\rm turb} \lesssim \sqrt{2}\sigma_{\rm H\beta;abs} \approx 110$ km s^{-1}. However, due to the large uncertainty in the measured width of the Hβ absorption (see Table 1), the highest allowable value for the turbulence velocity is actually 110 ± 40 km s^{-1}. We considered $v_{\rm turb}$ up to 120 km s^{-1}, which is still well within the 1σ uncertainty. As we mention later in this section, $v_{\rm turb} = 120$ km s^{-1} produces the smallest χ^2 compared to other values by fitting the observed Balmer break best. This motivates us to choose $v_{\rm turb} = 120$ km s^{-1} as the fiducial value, although we note that making a more conservative choice of $v_{\rm turb} = 100$ km s^{-1} only slightly increases the reduced χ^2 of the fit.

Combining all the above analyses, to model the attenuated AGN emission with spectral features compatible with the observational limits and a deep Balmer break, we chose $n_{\rm H} = 10^{10}$ cm^{-3}, $N_{\rm H} = 10^{24}$ cm^{-2}, $U = 10^{-1.5}$, and $v_{\rm turb} = 120$ km s^{-1} as the fiducial model parameters. We further discuss the impacts of these parameters later in this section as well as in Appendix B.

The remaining parameter is the shape of the AGN SED, for which we list a range of Eddington ratios in Table 2. To see the impact of the AGN SED, we performed three fits with different $\lambda_{\rm Edd}$ and fixed the other CLOUDY parameters to the fiducial values. The fitting results for each of these cases are shown in Fig. B2 of Appendix B. The overall continuum shapes produced by different models are very similar. Therefore, we choose $\lambda_{\rm Edd} = 0.1$ in our following analysis, also because it is more aligned with the accretion rate inferred by us in Section 5.1 ($\lambda_{\rm Edd} \sim 0.05 - 0.24$). We caution that we are not trying to set a stringent constraint on the Eddington ratio, but rather select a plausible value. As shown in Fig. B2, the main effect of different Eddington ratios is the strength of the nebular emission, which also leads to a change in the best-fitting covering fraction. In Section 8, we further discuss the scenario where Abell 2744-QSO1 actually hosts an AGN accreting at a super-Eddington rate.

Finally, we can use the fiducial parameters to infer the mass of the dense gas. If we assume that the gas responsible for the Balmer absorption is the same gas emitting the broad Hβ then gas mass can be simply inferred from the equation adopted by S. Carniani et al. (2015) assuming $T_{\rm e} \sim 10^4$ K

$$M_{\rm dense\ gas} = 0.85 \left(\frac{L_{\rm H\beta}}{10^{42}\ {\rm erg\ s^{-1}}}\right) \left(\frac{n_{\rm H}}{10^{10}\ {\rm cm^{-3}}}\right)^{-1} {\rm M_\odot}. \qquad (5)$$

Using the observed Hβ luminosity corrected for extinction as discussed in Section 5.1, and the gas density derived by our fitting of the absorber in this section, we obtain a gas mass of only ~ 4 M$_\odot$. We caution that the above calculation assumes typical emissivity coefficient, $\epsilon_{\rm H\beta} \equiv j_{\rm H\beta}/(n_{\rm e}n_{\rm p})$ (where $j_{\rm H\beta}$ is the Hβ emissivity), for Hβ in the NLR under the Case B assumption at $T_{\rm e} = 10^4$ K, whereas in the BLR, $\epsilon_{\rm H\beta}$ can be different (D. E. Osterbrock & G. J. Ferland 2006). With CLOUDY, we checked this effect by computing the average $\epsilon_{\rm H\beta}$ of two AGN-ionized clouds with $n_{\rm H} = 10^{10}$ cm^{-3} (BLR-like) and $n_{\rm H} = 500$ cm^{-3} (NLR-like), and we found BLR $\epsilon_{\rm H\beta}$ is roughly 12 per cent higher than that of the NLR $\epsilon_{\rm H\beta}$ at a fixed temperature of $T_{\rm e} = 10^4$ K, slightly decreasing the gas mass estimate to 3.6 M$_\odot$. Compared to the density, the temperature has a stronger effect, and we found that by increasing $T_{\rm e}$ from 10^4 K to 3×10^4 K, $\epsilon_{\rm H\beta}$ decreases by roughly a factor of 2, increasing the gas mass estimate to 8 M$_\odot$, which is still a relatively small amount of mass. Such a small gas mass is quite typical of the BLR of AGN, which can be very luminous in the recombination lines despite the small mass involved, as a consequence of the high densities (R. Maiolino et al. 2024b).

6.2.2 *Decomposing the optical spectrum of Abell 2744-QSO1*

In Fig. 6 we show the fitting result of our fiducial model, including the spectral model from the rest-frame UV to the optical for Abell 2744-QSO1, and the best-fitting parameters, which are summarized in Table 3. In the top panel of Fig. 6, we plot individually the component that dominates the rest-frame UV and the component that dominates the rest-frame optical. For the moment, we concentrate our discussion on the optical part, which is the focus of this paper, and we resume the discussion on the UV part in Section 6.2.3.

The most notable feature in the optical part of the model is the Balmer break. Close to the Balmer limit, the Balmer absorption features are increasingly blended as the energy level n increases. At the resolution of the PRISM spectrum, the blended absorption 'erodes' the red side of the Balmer break and leads to the slowly rising break in Abell 2744-QSO1. To make this smooth break, a key parameter is the turbulence velocity. As we have seen in Fig. 5, the depth of the Hβ absorption increases with increasing $v_{\rm turb}$. The same process applies to other Balmer absorption lines, making the erosion on the red side of the Balmer break stronger at high $v_{\rm turb}$. We note that in the CLOUDY models of K. Inayoshi & R. Maiolino (2025), which also predict a Balmer break, $v_{\rm turb}$ is effectively 0 and thus the Balmer break is always sharp. To demonstrate the importance of the turbulence, we compare two models with $v_{\rm turb} = 20$ and 120 km s^{-1}, respectively, in Fig. 7. In the top panel, we show the attenuated AGN continua of the two models normalized at $\lambda = 4260$ Å. The attenuated continuum with $v_{\rm turb} = 120$ km s^{-1} exhibits significantly deeper Balmer absorption and a redder Balmer jump due to the deepened and blended higher order Balmer absorption lines. After applying the dust attenuation, the more turbulent model shows a more gradual break. The bottom panel of Fig. 7 compares the fitting results based on these two models. Notably, without considering a strong turbulence, the fit is much worse around the Balmer break, resulting in $\chi^2_\nu = 1.35$, much larger than $\chi^2_\nu = 1.10$ arising from a strong turbulence.

The strongest turbulence we adopted is compatible with the upper limit set by the width of the Hβ absorption measured from the BlackTHUNDER spectrum, which is ${\rm FWHM}_{\rm H\beta;abs} = 185^{+69}_{-72}$ km s^{-1} (corresponding to $v_{\rm turb} < 110 \pm 40$ km s^{-1}). In addition, a consistency check can be performed using EW(Hβ), which is strongly dependent on $v_{\rm turb}$ as shown in Fig. 5. The best-fitting model with $v_{\rm turb} = 120$ km s^{-1} gives EW(Hβ) = 8.0 Å with respect to the co-added continuum (i.e. attenuated AGN continuum + nebular continuum + UV continuum), which is consistent with the value measured from the high-resolution spectrum, EW(Hβ)$_{\rm R2700} = 5.5^{+2.2}_{-1.7}$ Å within 1.1σ. If we lower the turbulence velocity to $v_{\rm turb} = 100$ km s^{-1}, the fit is slightly worse with $\chi^2_\nu = 1.15$. The resulting strength of the Hβ absorption becomes EW(Hβ) = 6.8 Å, consistent with the observed value within 1σ. Overall, our fitting results suggest that under the assumption of an AGN-dominated Balmer break, the best-fitting model indicates a level of turbulence with $v_{\rm turb} \sim 100$ km s^{-1}. This value is consistent with the turbulence velocity adopted in previous photoionization modelling of BLR clouds (J. A. Baldwin et al. 2004; G. J. Ferland et al. 2009; A. Sarkar et al. 2021).

Next, we examine other spectral features in the optical. The optical spectrum has a rising slope towards longer wavelengths, which can be explained by the dust reddened AGN continuum. The best-fitting value for the visual extinction is $A_{\rm V} = 2.13 \pm 0.02$ mag ($A_{\rm V} = 2.18 \pm 0.02$ mag for the image A used by Y. Ma et al. 2025). This value is slightly higher than the best-fitting magnitude of the dust attenuation estimated by Y. Ma et al. (2025) for their AGN-only model ($A_{\rm V} = 2.08 \pm 0.01$ mag) and Galaxy-only model

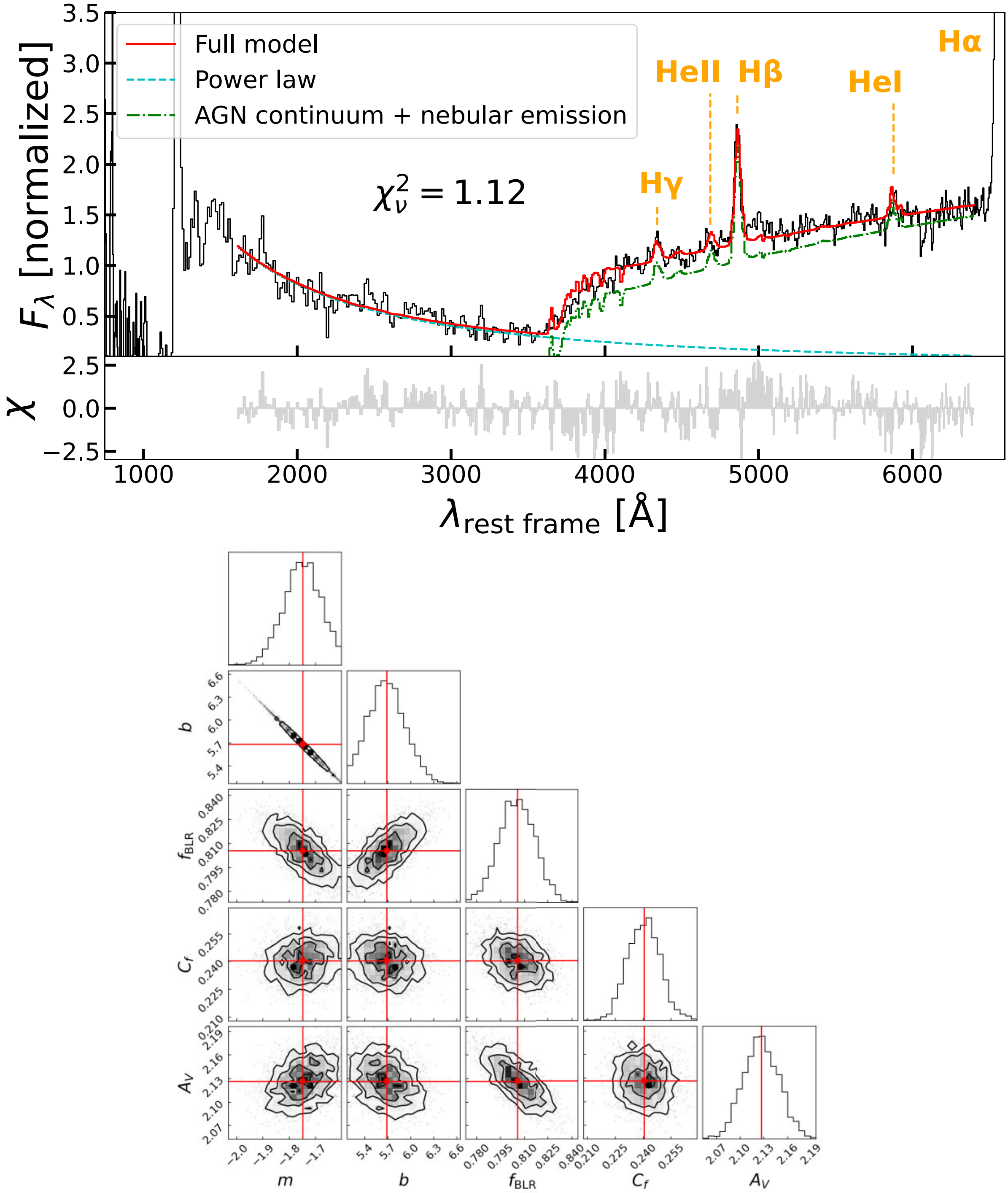

Figure 6. Fiducial fit for the PRISM spectrum of the A + C images reduced by the JADES GTO pipeline. *Top:* Best-fitting model for Abell 2744-QSO1, where the UV component and the optical component are plotted as the dashed line and the dash-dotted line, respectively. *Bottom:* Posterior distributions of the model parameters including the UV power-law slope, m, the UV power-law normalization, b, the normalization of the optical continuum, $f_{\rm BLR}$, the covering fraction of BLR clouds, C_f, and the magnitudes of the V-band extinction for the AGN emission, $A_{\rm V}$. The medians of the distributions are used as the best estimations and are indicated by the solid red lines.

($A_{\rm V} = 2.12 \pm 0.02$ mag), and significantly higher than the best-fitting $A_{\rm V}$ of their fiducial model (AGN + Galaxy; $A_{\rm V} = 0.50 \pm 0.09$ mag for the AGN component and $A_{\rm V} = 2.02 \pm 0.02$ mag for the Galaxy component). Compared to the fiducial fit of Y. Ma et al. (2025) to the image A of Abell 2744-QSO1 from the UNCOVER DR4, beside obtaining an improved χ^2_ν (2.38 versus 2.85; see Table 3), our fiducial fit does not require an unusually steep dust attenuation law. The implication of the dust attenuation is further discussed in Section 8. Finally, we note that the best-fitting nebular emission model, which includes nebular continuum as well as emission lines, is best described by a covering fraction of $C_f = 0.24 \pm 0.01$. The best-fitting value of C_f depends on the choice of $\lambda_{\rm Edd}$ and U, both

Table 3. Best-fitting model parameters for different PRISM spectra of Abell 2744-QSO1. All spectra are normalized to the flux densities at $\lambda = 4260$ Å before fitting. The model is given by $F_{\lambda;\rm model} = b\lambda^m + 10^{-0.4A_\lambda} f_{\rm BLR} F_{\lambda;\rm BLR} + F_{\lambda;\rm NLR}$ [see equation (2); here $f_{\rm BLR}$ is a normalization factor and is absorbed in the BLR terms in equation (2)]. The fiducial photoionization model parameters we used to compute $F_{\lambda;\rm BLR}$ are listed in Table 2. The fitting results for the spectra from L. J. Furtak et al. (2024), BlackTHUNDER, and the UNCOVER DR4 (the same one used by Y. Ma et al. 2025) are shown in Appendix C.

Fiducial model (images A + C); $\chi^2_\nu = 1.12$					
Parameter	m	b	$f_{\rm BLR}$	C_f	$A_{\rm V}$
value	-1.75 ± 0.07	5.7 ± 0.2	0.81 ± 0.01	0.24 ± 0.01	2.13 ± 0.02
Fiducial model (images A + B + C with L. J. Furtak et al. 2024's reduction); $\chi^2_\nu = 1.86$					
Parameter	m	b	$f_{\rm BLR}$	C_f	$A_{\rm V}$
value	-1.61 ± 0.01	5.20 ± 0.05	0.723 ± 0.007	0.22 ± 0.01	2.39 ± 0.02
Fiducial model (image A from BlackTHUNDER); $\chi^2_\nu = 1.09$					
Parameter	m	b	$f_{\rm BLR}$	C_f	$A_{\rm V}$
value	-2.17 ± 0.11	7.0 ± 0.4	0.86 ± 0.01	0.25 ± 0.01	2.04 ± 0.03
Fiducial model (image A from UNCOVER DR4, S. H. Price et al. 2025); $\chi^2_\nu = 2.38$					
Parameter	m	b	$f_{\rm BLR}$	C_f	$A_{\rm V}$
value	-2.00 ± 0.05	6.5 ± 0.2	0.79 ± 0.01	0.22 ± 0.01	2.18 ± 0.02

of which impact the relative strength of the nebular emission with respect to the strength of the continuum. For $\lambda_{\rm Edd} = 0.1 - 10$ and $U = 10^{-1.5}$, the best-fitting covering fraction is $C_f = 0.22 - 0.46$; for $\lambda_{\rm Edd} = 0.1$ and $U = 10^{-2} - 10^{-1}$, the best-fitting covering fraction is $C_f = 0.23 - 0.34$ (see Appendix B). For AGN at lower redshift, observations imply a wide range of C_f from 0.05 to 0.5 and might depend on the luminosities and Eddington ratios (e.g. G. J. Ferland et al. 2020). The best-fitting C_f for Abell 2744-QSO1 is still within the range found in the local Universe. We note that the models of K. Inayoshi & R. Maiolino (2025) assume $C_f = 1$, which leads to a stronger reduction in the strength of the Balmer break at high densities due to the contribution from a Balmer jump in the nebula. We further discuss the implication of the covering fraction in Section 8.

6.2.3 *Origin of the rest-frame UV emission*

Thus far, we have limited the spectral range of the fit away from the proximity of the Lyα damping wing. As already noted by Y. Ma et al. (2025), the PRISM spectrum of Abell 2744-QSO1 might have damped Lyα (DLA) absorption, which can be seen in the top panel of Fig. 1. If this feature close to Lyα emission is indeed a DLA, it might help to constrain the physical origin of the UV continuum.

In previous subsections, we have fitted the UV continuum of Abell 2744-QSO1 with a featureless power law without assuming its physical nature. Previous studies on LRDs have suggested their blue UV continua could come from less attenuated AGN continua or stellar continua (e.g. J. E. Greene et al. 2024; Z. Li et al. 2025; Y. Ma et al. 2025; M. Volonteri et al. 2025). Given the potential presence of the DLA in Abell 2744-QSO1, we aim to test the following two scenarios for the UV continuum. First, the UV continuum comes from the AGN continuum emission attenuated by the same dense gas as the optical continuum, but without being strongly attenuated by a foreground dust screen to preserve the blue UV slope. Secondly, the UV continuum comes from either the AGN continuum emission or a stellar continuum with the DLA absorber located outside the BLR and without being strongly attenuated by a foreground dust screen. The AGN scenarios above would require either that the dusty absorber has partial covering towards the UV continuum (e.g. C. W. Finn et al. 2014) or that the AGN continuum is scattered from a sightline that does not intercept the dusty medium.

In Fig. 8, we compare two fits with different UV continuum models and extend the fitted spectral range from $1600 - 6400$ Å to $1250 - 6400$ Å. In the left panel, the UV continuum is assumed to be the AGN continuum emission attenuated by a slab of gas with $N_{\rm H} = 10^{24}$ cm^{-2} (i.e. the same model as the optical continuum). The corresponding neutral hydrogen column density is $N_{\rm HI} = 9 \times 10^{23}$ cm^{-2}. We also allowed the UV continuum to have additional dust attenuation (independent of the best-fitting magnitude for the optical attenuation) during the fit, which is characterized by a free parameter $A_{\rm V}$ (DLA) and an extinction curve with the same shape as adopted for that of the optical continuum. Still, the best-fitting model yields $A_{\rm V}({\rm DLA}) = 0$. It is clear that such a model cannot provide a proper fit to the spectrum of Abell 2744-QSO1. This model not only fails at the location of the Balmer break by pushing up the break too much, but also fails in the whole UV regime due to the significantly more pronounced DLA feature compared to that observed in Abell 2744-QSO1. In the right panel, we reduce the gas column density that attenuates the AGN emission to $N_{\rm H} = 10^{22}$ cm^{-2} (with a neutral hydrogen column density of $N_{\rm HI} = 2.7 \times 10^{21}$ cm^{-2}) for the UV continuum but keep other model parameters the same. In this case, the overall fit is significantly improved and the DLA feature of the model roughly fits that in the observed spectrum. The best-fitting V-band attenuation is $A_{\rm V}({\rm DLA}) \approx 0.13$ mag, which is significantly lower than that of the optical attenuation. An immediate question is whether the DLA absorber is close to the BLR under the AGN scenario. As shown by A. C. Fabian, R. V. Vasudevan & P. Gandhi (2008), considering the effect of radiation pressure from the AGN emission on the dusty gas in the nuclear region, the gas is only long-lived when $N_{\rm H} > 5 \times 10^{23} \lambda_{\rm Edd}$ cm^{-2}. If the DLA absorber in Abell 2744-QSO1 does originate in the nuclear region, the column density adopted in our CLOUDY model ($N_{\rm H} = 10^{22}$ cm^{-2}) is close to the critical value when the gas becomes dynamically unstable at $\lambda_{\rm Edd} \sim 0.1$. We note that if we reduce the gas column density of the optical continuum model to the same value of $N_{\rm H} = 10^{22}$ cm^{-2}, the Balmer break in the model would become too shallow to fit the observed Balmer break.

Although here we used the AGN continuum to test the fit of the UV spectrum, the same should be applicable to the stellar continuum as the physical mechanism for creating the DLA feature is most sensitive to the gas column density. Also, an advantage of a UV stellar continuum (while the optical continuum being still AGN-dominated)

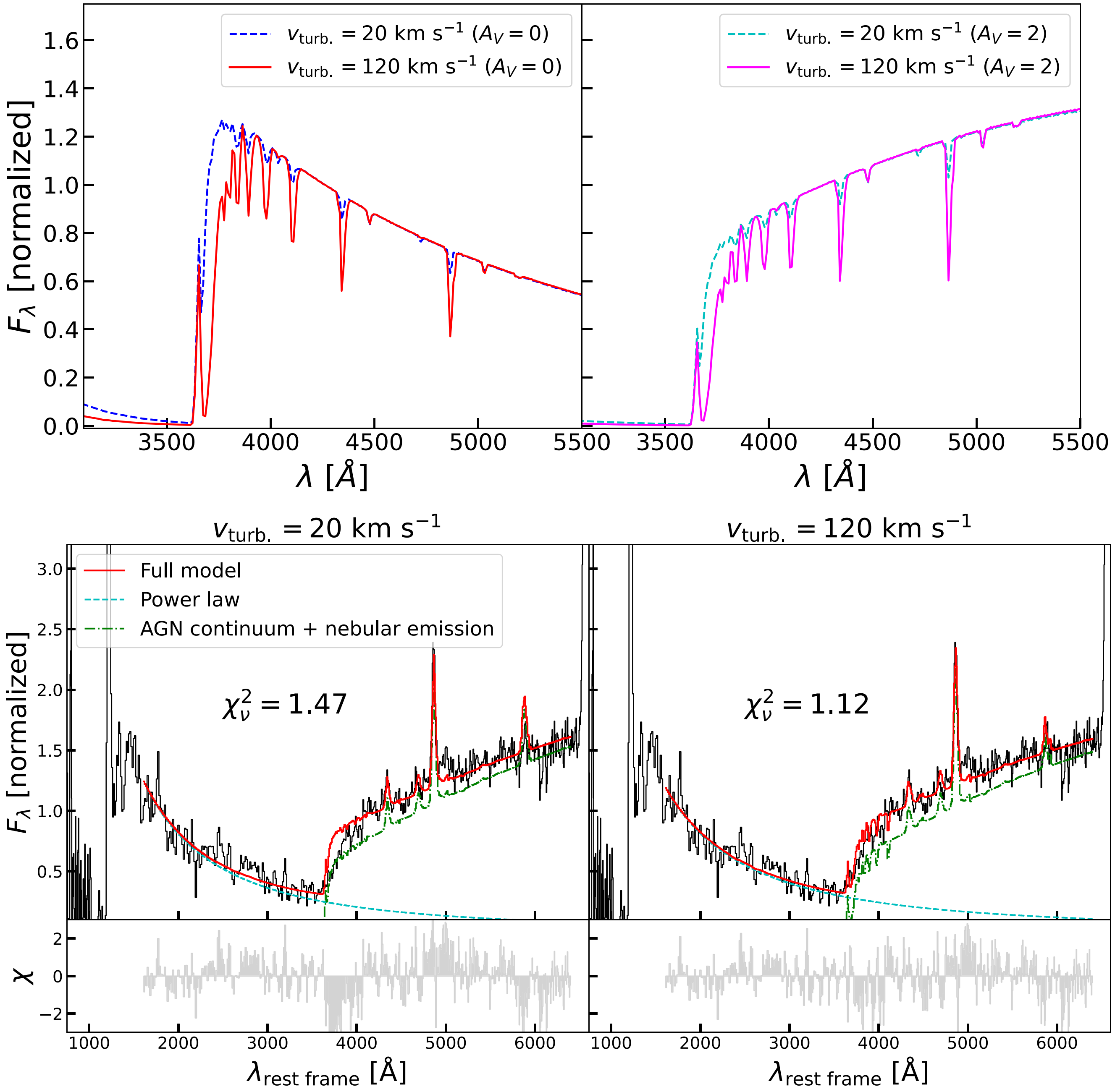

Figure 7. Comparison between model fits with low turbulence and high turbulence. *Top:* CLOUDY models for attenuated AGN continua with $v_{\mathrm{turb}} = 20$ and 120 km s^{-1}. Besides v_{turb}, the rest of the model parameters are fixed to the fiducial values in Table 2. The models have been convolved to the LSF of the PRISM spectrum and resampled to the wavelength grid of the PRISM spectrum. The left panel shows the model continua with no dust attenuation. The right panel shows the model continua attenuated by a foreground dust screen with $A_{\mathrm{V}} = 2$. The model with a higher v_{turb} produces deeper Balmer absorption and thus a more redshifted wing redward to the Balmer break. *Bottom:* Best-fitting models for the PRISM spectrum of Abell 2744-QSO1 (images A + C with the GTO reduction) with $v_{\mathrm{turb}} = 20$ and 120 km s^{-1} with a best-fitting $A_{\mathrm{V}} \approx 2.1$ mag. The high-turbulence fit yields a smaller χ^2_ν due to a better match between the model and the observed spectrum close to the Balmer break.

is that it can alleviate the problem where the UV and optical continua need to have different column densities and dust attenuation, if one considers the stellar populations providing the UV light originate from a much larger physical scale (see e.g. M. Volonteri et al. 2017, 2025). This simple practice shows that the UV continuum needs to be attenuated not only by a significantly less amount of dust but also by a significantly less amount of gas, if there is indeed a DLA absorber in Abell 2744-QSO1. If the UV stellar continuum has a stellar origin, one can estimate the stellar mass associated with the UV. This has been done by I. Juodžbalis et al. (2025b) following the M_{UV} – $M_\star$ relation derived by C. Simmonds et al. (2024) using photometric observations of galaxies at $3 \leq z_{\mathrm{phot}} \leq 9$ in JADES. The UV-based stellar mass estimate is $M_\star \approx 10^6$ M$_\odot$, compatible with the dynamical mass upper limit of $10^{7.3-8.6}$ M$_\odot$ (see Section 5.2).

One might wonder how the presence of the Lyα emission (see Table 1 for the measurements) can be explained if there is DLA at

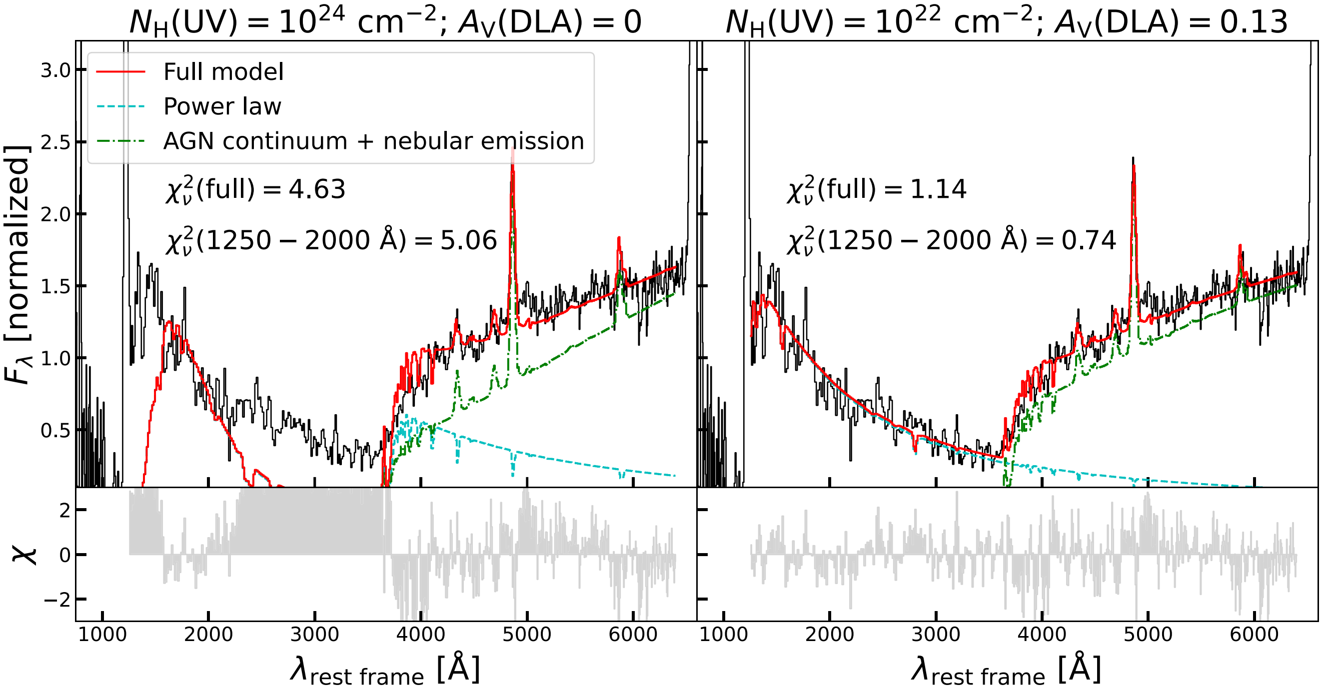

Figure 8. Comparison between two fits to the PRISM spectrum (extracted from the combined A + C images with the GTO reduction) with different UV continuum models. The UV model in the left panel is the AGN continuum emission attenuated by gas with $N_{\rm H} = 10^{24}$ cm^{-2} (i.e. the same gas that attenuates the optical continuum). The UV model in the right panel is the AGN continuum emission attenuated by gas with $N_{\rm H} = 10^{22}$ cm^{-2}. Both UV continuum models are allowed to have dust attenuation characterized by $A_{\rm V}$(DLA) during the fit. The rest of the photoionization model parameters are the same as the fiducial values listed in Table 2. Different from previous fits, the fitted spectral range is extended to 1250 − 6400 Å in the rest frame of Abell 2744-QSO1 to capture part of the DLA-like feature and avoid Lyα emission. The UV component is better fitted by the model with a lower column density compared to that of the optical component.

the same time. One possibility is that the Lyα emission comes from the more diffuse gas on a larger scale (e.g. ionized or reflecting gas in the Circum-Galactic Medium, CGM), whereas the DLA is produced in gas blocking the UV light emitters on a smaller scale along the LOS. Such a geometry has been proposed for several sources with strong Lyα emission and DLA-like feature (e.g. W. Hu et al. 2023; S. Wu et al. 2024; S. Tacchella et al. 2025; J. Witstok et al. 2025). The BlackTHUNDER PRISM IFU data do show that the Lyα emission is offset (by 0.″05 = 270 pc in the image plane and roughly 160 pc in the source plane; L. J. Furtak et al. 2024) relative to the optical continuum, possibly supporting this scenario; however, the analysis of the Lyα emission goes beyond the scope of this work and will be discussed in a separate paper. An alternative explanation is that the UV continuum is actually dominated by a nebular continuum, where the DLA-like feature is actually the signature of a two-photon continuum (A. J. Cameron et al. 2024). Indeed, given the current S/N of the spectrum, we cannot rule out the case where the flux density of the UV continuum peaks at 1430 Å as the two-photon continuum (C. M. Gaskell 1980). This nebular continuum cannot originate in the BLR or its proximity as the two-photon continuum is significantly suppressed at $n_{\rm H} \gtrsim 10^4$ cm^{-3} (M. C. Bottorff, G. J. Ferland & J. P. Straley 2006). It can be created either in the diffuse gas close to/outside the BLR or in the gas surrounding very hot and massive stellar populations (e.g. S. A. Grandi 1982; D. Schaerer 2002; A. Raiter, D. Schaerer & R. A. E. Fosbury 2010; A. K. Inoue 2011; E. Zackrisson et al. 2011).

The existence of the two-photon continuum must be accompanied by the bound-free continuum of hydrogen as well as Balmer emission lines. We can thus perform another fit by including the above components to see whether the nebular continuum scenario works. We set up a simple configuration by using the nebular continuum computed with PYNEB (V. Luridiana, C. Morisset & R. A. Shaw 2015). We used the GET_CONTINUUM function and included two-photon emission, bound-free emission, and free–free emission from hydrogen. The density is set to $n_{\rm H} = 100$ cm^{-3}, below the low-density limit of the two-photon emission. The temperature and the normalization of the nebular continuum is set to vary freely during the fit. Specifically, we allow the temperature to vary within 5×10^3 K $< T_{\rm e} < 3 \times 10^4$ K. In principle, the normalization of the nebular continuum should be fixed to the fluxes of Balmer lines emitted by the same cloud (M. Peimbert 1967). In the case of Abell 2744-QSO1, a natural assumption might be that the nebular continuum originates in the gas emitting the narrow Hβ. Regardless, we set the normalization as a free parameter to see whether the nebular continuum can provide a sensible fit without this physical constraint. Also, we included additional dust attenuation characterized by $A_{\rm V;neb.\ con}$ as a free parameter. Fig. 9 shows the best-fitting model for Abell 2744-QSO1 with a nebular dominated UV component and an optical component dominated by attenuated AGN emission. This fit results in the same χ^2_ν compared to the DLA fit with $N_{\rm H} = 10^{22}$ cm^{-2}. However, the fit is worse in the FUV region as reflected by a significantly larger χ^2_ν at 1250 − 2000 Å mainly due to the underestimation of the flux densities. Clearly, the nebular continuum is not steep enough to describe the UV continuum of Abell 2744-QSO1 especially at shorter wavelengths, even if we included an extra freedom (i.e. the normalization of the nebular continuum) during the fit. The fit also prefers the temperature of the diffuse gas to be $T_{\rm e} \approx 30\,000$ K, which would be among the highest

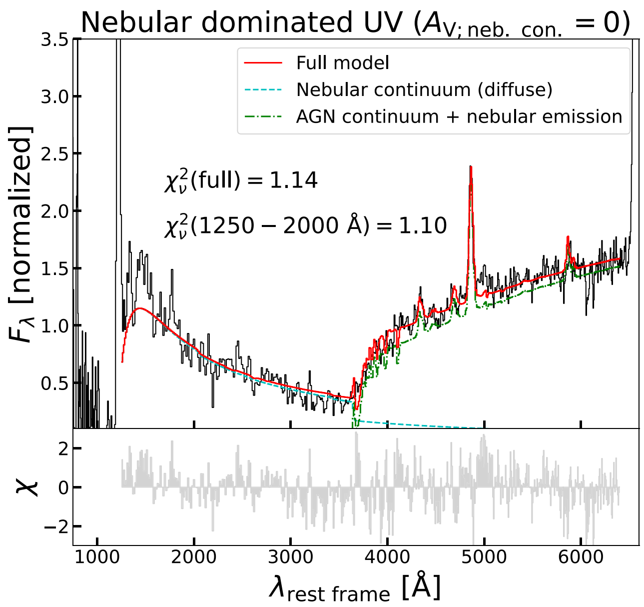

Figure 9. Fitting attempt that adopts a nebular dominated continuum for the UV component. The nebular continuum is assumed to come from low-density (diffuse) gas with no dust attenuation, and it includes hydrogen two-photon emission, the free-bound emission, and the free–free emission. The temperature and the normalization of the nebular continuum are allowed to vary. While the diffuse nebular continuum provides a equally good fit to that of the DLA model based on the overall χ^2_ν, the fit in the FUV region near Lyα is worse.

temperatures currently found by *JWST* at $z \gtrsim 4$ (I. H. Laseter et al. 2024). In Appendix C we show the results for PRISM spectra with other reductions and we found a general agreement between most reductions.

To conclude, while the nature of the UV continuum of Abell 2744-QSO1 remains unclear, it is most likely explained by either stellar populations or AGN continuum emission with little dust attenuation and a DLA produced by gas with $N_{\rm H} \sim 10^{22}\ \rm cm^{-2}$. In the case of stellar light, the UV component is more spatially extended compared to the optical component. In the case of AGN light, the UV component might be as compact as the optical component but a specific geometry is needed to explain the differential attenuation. Still, without better observational constraints in the FUV, we cannot fully rule out the nebular dominated scenario, which is further discussed in Appendix C.

Thus far, we have explored models where the optical spectrum of Abell 2744-QSO1 is dominated by AGN light. An immediate question related to this model is whether there is any sign of variability associated with the AGN emission as typically found at lower redshift (e.g. C. J. Burke et al. 2021), which we discuss next.

7 VARIABILITY AND REVERBERATION MAPPING

The triply imaged system, Abell 2744-QSO1, is in principle an excellent tool to explore variability of AGN at high redshift. Indeed, the arrival times of the three images are subject to delays associated with the image-lens configuration. Specifically, as pointed out in Appendix A, the arrival of image C is followed by image A 18–19 yr later (= 2.2 − 2.4 yr rest-frame), which is then followed by image B another ∼ 2.2 − 3 yr later (3.2–4.5 months rest-frame), depending on the lens model. Unfortunately, as mentioned in Appendix A, the uncertainties in the lensing magnifications of the three images do not allow exploring variability by simply comparing the fluxes of the three images.

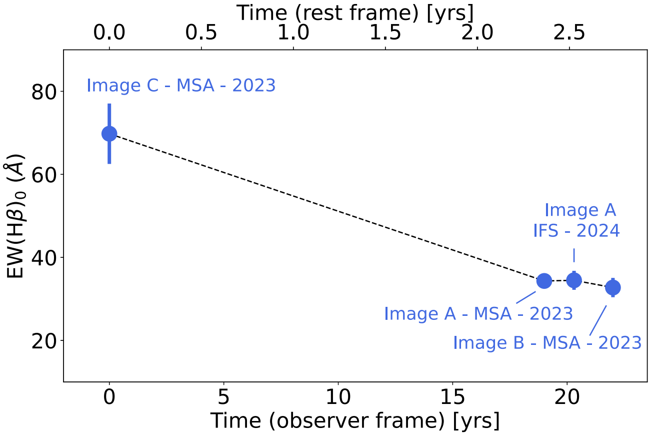

Figure 10. Variation (or lack thereof) of the rest-frame equivalent width of Hβ measured in the four spectra of Abell2744-QSO1: the three MSA spectra of the three images obtained in 2023 and BlackTHUNDER IFU spectrum obtained in 2024. The spectra are plotted as a function of arrival time since the observation of image C, taking into account the lensing time delay. While images A and B do not show evidence for variation of the EW, image C clearly shows an EW that is about two times higher than in the other images, at high significance.

However, the BlackTHUNDER IFU spectrum provides an additional, new epoch of image A, taken one year after the MSA spectrum. In Appendix D, we show that the spectra taken at the two epochs (July 2023 and November 2024) are consistent with each other within the uncertainties, implying that the source has probably been stable within the ∼ 2 months in the rest frame covered by the two observations (although we cannot exclude variability between the two epochs).

While comparing the absolute fluxes is not really possible between the different images, because of the magnification factor uncertainties, it is possible to compare the equivalent widths of the lines, as these are calculated relative to the continuum at similar wavelengths and thus are insensitive to lensing magnification. Fig. 10 shows the variation of the equivalent width (rest frame) of Hβ as a function of time relative to the arrival time of image C. While the EWs of image A in the two epochs (MSA and IFU) and image B are fully consistent with each other, the EW of image C is clearly higher, by about a factor of two and with high significance relative to the other two images.

We note that when undertaking this kind of variability analysis it is important to use the full-shutter, pipeline extracted 1D spectra, as these fully and rigorously take into account path losses and diffraction losses. Using 1D spectra extracted from the 2D spectra with any kind of custom aperture is deprecated in this case, as the extraction from the 2D spectra loses information on the path- and diffraction-losses. In Appendix D, we illustrate this issue by showing that the analysis performed on spectra extracted with the latter method provides results that are quantitatively different because of such issues, although the qualitative trends remain.

The higher equivalent width of Hβ in image C can also be seen visually in the top panel of Fig. 11, where the four PRISM spectra (three MSA and one IFU) are compared with each other after being normalized to the continuum level in the vicinity of Hβ. Although the

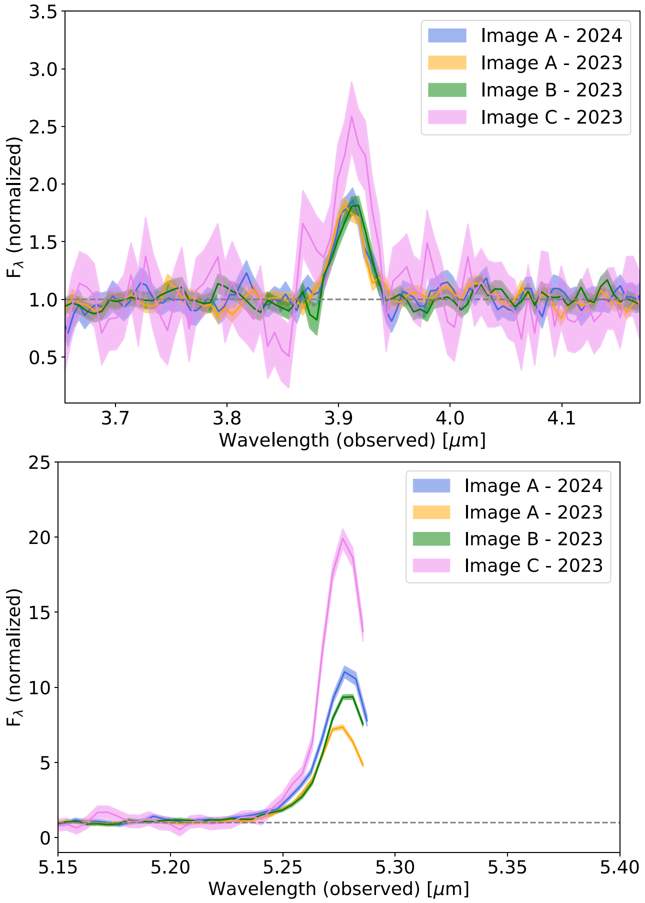

Figure 11. Top: Comparison of the four spectra of Abell2744-QSO1 around Hβ, normalized to the continuum level. Although the spectrum of image C is noisier than the others, its Hβ is clearly more prominent than in the other images (i.e. has a higher equivalent width). Bottom: Same comparison for Hα. The Hα line is at the edge of the available wavelength range, hence its red wing is partly chopped. Additionally, the calibrations at such long wavelengths are more uncertain, hence variations of the order of 15–30 per cent may not be real. However, the spectrum of image C shows that Hα is clearly much stronger (relative to the continuum) when compared with the other two images by about a factor of two, consistent with what observed for Hβ.

spectrum of image C is more noisy, the relative flux of Hβ is clearly higher, even taking into account the noise. The same comparison for Hα is shown in the bottom panel of Fig. 11. Unfortunately, Hα is at the edge of the wavelength range, and the red wing of its profile is chopped. Additionally, at such long wavelengths the calibrations are more uncertain therefore the 10 per cent–30 per cent variation seen in images A and B should be considered with caution and may not be real. However, the Hα line of image C is much stronger (relative to the continuum) than observed in images A and B, by about a factor of two (i.e. at the same level seen in Hβ).

Clearly, the AGN in Abell2744-QSO1 must have undergone a short phase of enhanced accretion before the spectroscopic observation of image C or, equivalently, the accretion rate (hence continuum luminosity) must have dropped during the spectroscopic observation of image C. Then, during the spectroscopic observation of image C we are observing the BLR reverberation traced by the Hβ, which has not yet adjusted its flux relative to the continuum variation, due to the extension of the BLR.

It is possible, in principle, to test this by looking at the flux difference in image C between the photometry in 2022 and its MSA spectrum in 2023. One should always be cautious about comparing photometry and slit spectroscopic measurements because of slit losses plaguing the latter. However, given that Abell2744-QSO1 is point like, and that its location in the shutter is known accurately, the slit losses provided by the pipeline are quite accurate (better than 15 per cent). The comparison of photometry and spectroscopy of image C is shown in bottom panel of Fig. 12, where the red circles show the photometry from 2022 and the orange squares show the synthetic photometry obtained from the spectrum (where the errorbars include both the Poissonian error and calibration uncertainties). In the optical rest frame the photometry from 2022 is clearly higher than the spectrum in 2023 by a factor of about two. This is exactly the flux difference expected by the higher EW(Hβ) observed in 2023 for image C. In other words, the MSA spectrum of image C shows either the increase of EW(Hβ) is due to a drop in continuum ionizing emission between 2022 and 2023, or the Hβ reverberation of an increase in continuum flux in 2022.

The UV rest-frame spectrum of image C is too noisy to draw any conclusions, and it is consistent with no variability within 1–2σ. However, should variability be confirmed also in the UV, this would favour an AGN contribution also in this spectral region, possibly within the partial covering scenario discussed in Section 6.2.3. If the UV is truly varying, following the variability pattern of SDSS quasars measured by C. L. MacLeod et al. (2010), one expects the RMS flux variation in the UV is stronger than that in the optical. For image C, given its optical variation of 50 per cent, the expected UV variation should be roughly 67 per cent, compatible with the measured UV variation of 50 ± 50 per cent. However, we cannot draw any further conclusions due to the large uncertainty and the fact that the RMS variation is not well constrained by two epochs.

Unfortunately, there is no photometry available at the epoch of the spectroscopic observation. As discussed in Section 3, images in F356W and F444W are available about 8 months before and 4 months after the spectroscopic observation. The photometry does not show evidence for variability at those two epochs, at a level higher than 3σ, although for image C variability of up to 25 per cent would be consistent with the photometric observations and associated uncertainties.

We notice that, in contrast to image C, the comparison of photometry and MSA spectroscopy for images A and B does not show evidence for significant flux variation among the two epochs (a variation in the UV for image B is likely due to the problematic background subtraction discussed above and associated with a bright foreground galaxy). This is shown in the top and middle panels of Fig. 12. This means that about 17 yr after the arrival of image C ($\sim$2 yr rest frame) the source was relatively stable in flux for a few rest-frame months, as also evident from the stable EW(Hβ). We note that if the UV of image B is truly varying, taking the small optical variation of ~ 8 per cent at $\lambda_{\rm obs} \approx 4.4$ µm, one expects a UV variation of 13 per cent at $\lambda_{\rm obs} \approx 1.5$ µm following the result of C. L. MacLeod et al. (2010). While this is marginally compatible with the measured UV variation of 35 ± 16 per cent, we again caution on the large uncertainty and the two-epoch measurement.

Unfortunately, with only two data points for image C it is very difficult to attempt a reverberation mapping. However, the finding that the EW(Hβ) is two times higher than its regime value at later epochs, and as expected by the higher continuum flux in 2022, indicates that the BLR has not yet adjusted its flux to the

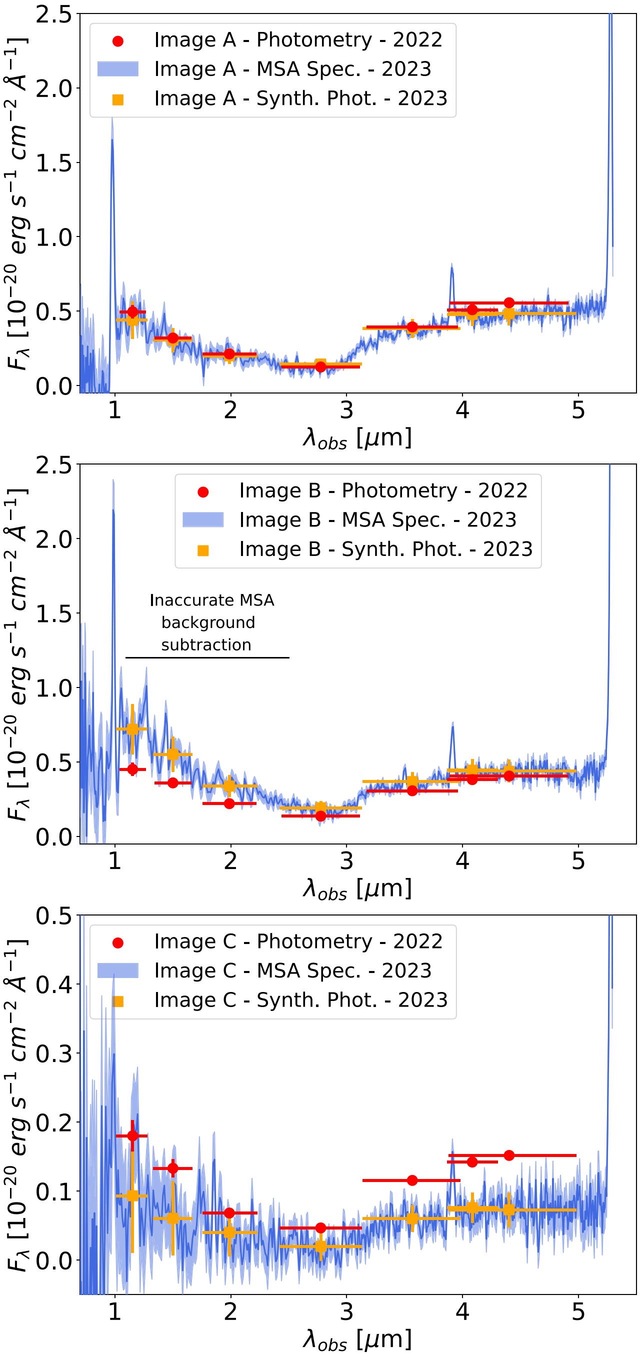

Figure 12. Comparison of the MSA spectra, and associated synthetic photometry (red circles), taken in July–August 2023, with the photometry from the images take in November 2022 (orange squares), for image A (top), B (middle), and C (bottom). Clearly the continuum flux in the optical rest-frame of image C was higher in 2022, by about a factor of two, relative to the spectrum taken in 2023, showing a flux drop, at least in the optical, by a factor of about two between 2022 and 2023. On the contrary, 2022 photometry and 2023 spectroscopy of image A are in agreement within errors, and the same is for the optical part of image B. The UV part of image B shows a variation, but this is likely due to the background subtraction issues in image B due to the blue foreground galaxy, 0.″9 from image B.

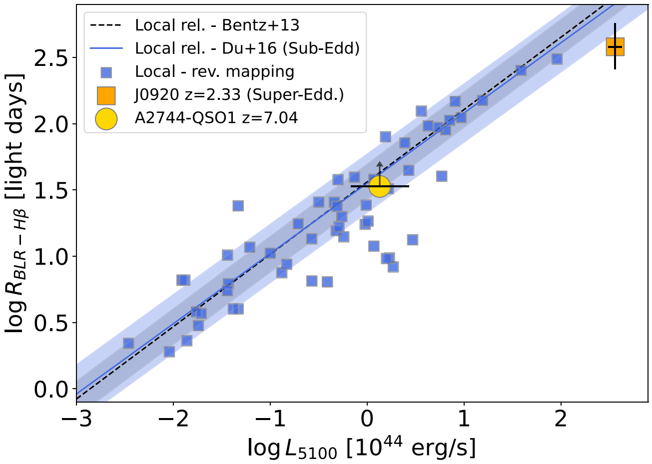

Figure 13. Relation between radius of the BLR and optical continuum luminosity (L_{5100}) from Hβ reverberation mapping in local AGN (small blue squares), where the blue solid line and black dashed lines show the best fit of the local relations from P. Du et al. (2016) (for their sub-Eddington sample) and M. C. Bentz et al. (2013), and the shaded region show the scatter of the relations. The golden circle shows the lower limit on the radius of the BLR inferred for Abell2744-QSO1 based on the variability of image C. The large orange square shows the interferometric measurements at $z = 2.33$ obtained by R. Abuter et al. (2024) for a QSO accreting at a highly super-Eddington rate.

flux drop between November 2022 and July 2023. This essentially means that the radius of the BLR must be larger than about 9-light-months/$(1 + z)$, which is about 45 light-days. This constraint is shown in Fig. 13 and compared with the scaling relation between the BLR radius (for Hβ) and L_{5100}, as inferred from reverberation mapping in local/low-z galaxies, specifically data from table 7 of P. Du et al. (2015) and the relations for sub-Eddington AGN taken from P. Du et al. (2016) (blue solid line and blue shaded region), as well as the relation (from 'Clean2' parameters) of M. C. Bentz et al. (2013). We also show the interferometric image obtained by R. Abuter et al. (2024) at $z = 2.33$ (orange square) for a super-Eddington quasar. The lower limit on the size of the BLR inferred for Abell 2744-QSO1 is consistent with the scatter of the local relations. Additional spectroscopy of image C in the future will be able to verify whether the BLR in this early AGN at $z = 7.04$ behaves as the BLRs of local AGN.

Finally, the simple fact that the continuum of image C has been varying by a factor of two between 2022 and 2024 indicates that at least the optical continuum cannot be dominated by stellar light. This is consistent with our analyses in previous sections, based both on the dynamical mass analysis and on the modelling of the Balmer break and SED.

8 DISCUSSION

In previous sections, we present our physical model for Abell 2744-QSO1 where the optical spectrum is dominated by AGN light based on observational data. In this section, we discuss whether the physical model we adopted for Abell 2744-QSO1 can in principle be generalized to other *JWST*-selected LRDs that host AGN. In addition, we discuss the implications of our fitting results in the context of the peculiar observational features of *JWST*-selected Type 1 AGN.

8.1 Applicability to other LRD AGN

Thus far we have focused our analyses on Abell 2744-QSO1, an LRD and a Type 1 AGN identified by *JWST*. An immediate question is whether the *V*-shape spectra and Balmer break observed in other LRD AGN can be explained by the same modelling approach.

Based on our analyses shown in Section 6.2, the *V*-shape can be explained by an unobscured UV component of a stellar or an AGN origin, and an optical component corresponding to an AGN continuum attenuated first by high-density and dustless gas and then by a dust screen (which can potentially be also the outer regions of the high-density gas). The shape of the Balmer break in such a model is mainly determined by the physical conditions of the dense gas that absorbs the AGN continuum, as well as the amount of external dust attenuation. It is worth noting that the shape of the Balmer break varies among LRDs. For example, I. Labbé et al. (2024) recently reported an LRD at $z = 4.47$, which has both Hα absorption and a 'sharp' Balmer break that rises rapidly at the wavelengths longwards of the Balmer limit, unlike the gradual break we see in Abell 2744-QSO1. One might thus wonder whether our modelling approach can explain the diversity of the Balmer breaks in LRDs. One potential clue to resolve this question comes from the variation in the turbulence. As shown in Fig. 7, at low turbulence, the Balmer break becomes sharper compared to the case of high turbulence. This is due to the weakening of the Balmer line absorption at low turbulence shown in Fig. 5, which results in less erosion of the break. Therefore, in the context of our models, the diversity of the Balmer break could be partly related to the diversity of the turbulence in the dense absorbing gas (see e.g. M. Bottorff et al. 2000). Additionally, superpositions (and blending) of strong emission lines might change the shape of the break. While in the case of Abell 2744-QSO1 the emission lines are not very strong, in the case discussed by I. Labbé et al. (2024), an abundant set of strong emission lines are present. Furthermore, we have not fully excluded the contribution from a stellar Balmer break, which would add more complexity to the shape of the break. We will present our analyses on other LRDs including the one reported in I. Labbé et al. (2024) in a future paper.

One might wonder what observational evidence is required to verify our models. One piece of evidence comes from the connection between the Balmer break and the Balmer absorption. As already shown by K. Inayoshi & R. Maiolino (2025) and in Fig. 5, when there is a strong Balmer break, there is likely also strong Balmer absorption produced in the same gas. Despite the complex dependencies of the break and absorption strengths on various parameters, statistically, stronger Balmer breaks are accompanied by stronger Balmer-line absorption. The fact that at least 20 per cent of the LRDs and *JWST*-discovered AGN show evidence of Hα absorption suggests that the observed Balmer breaks likely have, at least partly, a dense-gas absorption component. Still, a detailed fit and assessment is required for each individual LRD/AGN, which is beyond the scope of this paper. In addition, constraining the shape of the Balmer break in observations will be useful, since statistically, narrower and weaker absorption would correspond to sharper breaks. We do emphasize that there could be large stochasticity within small samples. Thus, it is vital to accumulate more high spectral resolution observations aiming to find Balmer lines absorption and combine them with PRISM observations. Another interesting observable is the potential DLA-like features in the rest-frame FUV of LRDs. Verifications and detailed modelling of these features can help us understand the origin of the UV continuum. This requires more PRISM observations with high S/N to constrain the shapes of the DLA-like features and compare them with the shapes of the Balmer breaks.

Finally, we would like to comment on the occurrence rate of LRDs given our physical model. It is known that not all *JWST*-selected AGN are LRDs. As shown by K. N. Hainline et al. (2025), about 30 per cent of the *JWST*-selected Type 1 AGN are LRDs. If the case of Abell 2744-QSO1 is typical, given a covering fraction of $C_f \approx 0.24$ for BLR clouds (see Section 6.2.2), one expects about 24 per cent of the time our LOS is blocked by dense BLR gas, which implies an LRD fraction of 24 per cent. This is certainly a very rough estimation and does not take into account the variations in the AGN and BLR properties. Also, as we have shown in Section 6 and in Appendix B, the derived value for C_f depends on the assumption of the Eddington ratio and the ionization parameter and can vary in a range of $0.22 - 0.46$ for Abell 2744-QSO1. Furthermore, we caution that it remains debated whether all LRDs are hosting AGN since the majority of these sources are colour-selected. Still, it would be interesting to investigate the properties of the absorbing gas over a larger sample and see if they match the statistics.

8.2 Implications of a non-stellar origin of the Balmer break

Past attempts to fit the Balmer break observed in Abell 2744-QSO1 and in other LRDs have faced difficulties with scenarios advanced that are extreme and difficult to reconcile with other findings. The stellar interpretation of the Balmer break typically leads to high stellar mass. Combined with the large number of LRDs, this results in extremely high stellar mass density per cosmic volume, possibly in tension with the standard cosmological framework (K. Inayoshi & K. Ichikawa 2024; B. Wang et al. 2025; H. B. Akins et al. 2025b).

Additionally, when combined with the very compact sizes of the LRDs (often unresolved), a stellar interpretation of the Balmer break and optical continuum results in extremely high stellar densities of $10^6 - 10^7$ M$_\odot$ pc^{-2} (J. F. W. Baggen et al. 2024; I. Labbé et al. 2024), which have never been seen (with such high masses) at lower redshifts or in the local Universe, hence posing the question of how these hyper-dense and massive stellar system would dissolve across the cosmic epochs. The same issue also applies specifically to Abell 2744-QSO1, for which Y. Ma et al. (2025) reported a lower limit on the stellar density of 10^6 M$_\odot$ pc^{-2}, if one associates the Balmer break and optical continuum with a stellar origin. However, the same authors recognized that any stellar fit is unsatisfactory for this object, and an unusually steep extinction curve (steeper than both the D. Calzetti et al. 2000 and SMC extinction curves of K. D. Gordon et al. 2003) is required.

Our work strongly disfavours a stellar origin of the optical continuum and of the Balmer break on multiple grounds. The conservative upper limit on the dynamical mass is at least an order of magnitude below the stellar mass obtained when interpreting the Balmer break and optical continuum in terms of stellar emission, which implies a very conservative upper limit of 10 per cent on the contribution of the stellar light to the optical continuum and Balmer break. Our dense-gas absorption scenario provides a good fit ($\chi^2_\nu = 1.12$) to the spectrum and predicts the presence of Hβ absorption which is roughly consistent with the high-resolution spectrum. The indications of variability provide further support for the non-stellar origin of the optical continuum.

The scenario of an optical continuum dominated by AGN light and the Balmer break originating from gas absorption naturally avoids all extreme physical scenarios faced when interpreting the Balmer break and optical continuum as stellar, as discussed above. AGNs are intrinsically very compact; hence, if they dominate the optical continuum, they very naturally explain the very compact (often unresolved) emission. It has been known for decades that AGNs are surrounded by extremely dense gas (the BLR; H. Netzer 1990), hence ascribing the Balmer break to dense gas absorption does not require invoking new, exotic scenarios.

Clearly, AGN dominating the optical continuum of LRDs and dense gas absorption being responsible for the Balmer break, naturally explain most of their properties. In this paper, we have verified this model for the specific case of Abell 2744-QSO1. However, as discussed in the previous section, the same scenario may explain the properties observed also in other LRDs. This would more broadly alleviate the issues faced by previous work when attempting to explain the Balmer break with a stellar origin. An analysis of other LRDs with a methodology similar to that adopted here will be presented in a future work.

8.3 Insights into the X-ray weakness of *JWST*-selected AGN

In the local Universe, it is observed that AGNs are frequently accompanied by strong hard X-ray emission, which has been proposed to be associated with 'hot coronae' above accretion discs. Photons from the accretion discs undergo Compton up-scattering by electrons in the hot coronae, leading to non-thermal X-ray emission. The non-thermal hard X-ray emission is generally considered as a ubiquitous feature of AGN, whose contributions to the AGN SED can be characterized by a spectral slope from the optical to the X-ray, $\alpha_{\rm ox} = -0.384 \times \log(L_{2\ \rm keV}/L_{2500\ \text{Å}})$, which has a typical value of -1.2 to -1.4 for Type 1 AGN and QSOs at $z \lesssim 3$ (G. Zamorani et al. 1981; E. Lusso & G. Risaliti 2017).

However, one of the most puzzling observational results obtained by combining data from *JWST* and from X-ray missions, such as *Chandra*, is the lack of hard X-ray emission in most *JWST*-selected AGN (T. T. Ananna et al. 2024; M. Kokubo & Y. Harikane 2024; E. Lambrides et al. 2024; J. Lyu et al. 2024; M. Yue et al. 2024b; R. Maiolino et al. 2025b). For example, as shown by R. Maiolino et al. (2025b), compared to quasars selected in the UV/optical at low redshift, *JWST*-selected AGN at $z \gtrsim 4$ with similar bolometric luminosities, no matter whether they are Type 1 or Type 2, are 1–2 orders of magnitude weaker in their X-ray luminosities. Similarly, E. Lambrides et al. (2024) found that the broad-line AGN selected by *JWST* must have their $\alpha_{\rm ox}$ offset from the lower redshift broad-line AGN at similar UV luminosities by more than 0.6 dex.

The explanations for the X-ray weakness of the *JWST*-selected AGN (apart from the non-AGN explanations) can be broadly divided into external processes and internal processes. For external processes, R. Maiolino et al. (2025b) suggest Compton-thick obscuration by dust-free clouds within BLRs leads to the X-ray weakness. This picture is further investigated by I. Juodžbalis et al. (2024a) using the observation of an extremely X-ray weak AGN at $z = 2.26$, suggesting that the Compton-thick clouds along the LOS also lead to strong Balmer and He I absorption detected in the *JWST*/NIRSpec grating spectra of this source. Furthermore, B. Trefoloni et al. (2025) suggest the metal-poor nature of the BLRs of the *JWST*-selected AGN might lead to more compact BLRs compared to metal-rich AGN at low redshift as well as metal-rich QSOs at high redshift, increasing the chance of obscuration. For internal processes, various authors have suggested super-Eddington accretion as a mechanism to reduce hard X-ray luminosities (L. Dai et al. 2018; A. King 2024; E. Lambrides et al. 2024; P. Madau & F. Haardt 2024; F. Pacucci & R. Narayan 2024; K. Inayoshi et al. 2025). For example, E. Lambrides et al. (2024) argue the super-Eddington accretion leads to much steeper optical-to-X-ray slopes and thus reduces the X-ray luminosities. E. Lambrides et al. (2024) also show that the high-ionization emission lines are suppressed under super-Eddington accretion due to photon trapping. Meanwhile, super-Eddington accretion can also explain the lack of UV/optical variability in *JWST*-selected AGN due to photon trapping (K. Inayoshi et al. 2025).

For Abell 2744-QSO1 L. J. Furtak et al. (2024) report that the hard X-ray emission constrained by *Chandra* in the rest-frame 40 keV only has a 3σ upper limit of $L_{40\ \rm keV} < 3 \times 10^{43}$ erg s^{-1}, which is at least 10 times weaker than the value expected from UV/optical luminosities given a typical AGN SED. Given the confirmation of the X-ray weakness, we discuss below whether any of the physical conditions in Abell 2744-QSO1 we derive would imply reduction in the X-ray emission.

First, we note that the column density for the dust-less gas in our fiducial model is $N_{\rm H} = 10^{24}$ cm^{-2}, and the Compton-thick column density is $N_{\rm H;thick} \approx 1.5 \times 10^{24}$ cm^{-2}. Thus, our fiducial model of a slab of gas along the LOS is capable of reducing the hard X-ray emission by a factor of 2 (or 0.3 dex) at 40 keV, whereas a cloud that is twice as thick as the cloud in our fiducial model can reduce the hard X-ray emission by roughly a factor of 4 (0.6 dex). We emphasize that the above estimations are only tentative as we are not constraining the total $N_{\rm H}$ accurately in our analyses, and the photoelectric absorption of X-ray is not quantitatively calculated (see M. S. Longair 2011). Additionally, the column density estimated from our models is only sensitive to the fraction of the gas responsible for the Balmer absorption and Balmer break. It is possible that there is additional gas (on the opposite side of the illuminated side of the clouds; see discussion in I. Juodžbalis et al. 2024a) that is colder and, while not contributing to the Balmer absorption, its column contributes to the X-ray absorption. In other words, the column density estimated in our model is only a lower limit of the column density absorbing the X-rays.

An immediate question is how often one expects to see X-ray weak AGN if it is due to Compton-thick absorption. In principle, the occurrence rate of the X-ray weak AGN should depend on the covering fraction of Compton-thick clouds. If we took the covering fraction from our best-fitting fiducial model, which is $C_f \approx 0.24$, the occurrence rate would be 24 per cent, which is significantly lower than the nearly 90 per cent of the X-ray weakness in *JWST*-selected Type 1 AGN (R. Maiolino et al. 2025b; Ji et al., in preparation) but close to the occurrence rate of LRDs among the sample of *JWST*-selected Type 1 AGN (∼ 30 per cent; K. N. Hainline et al. 2025) as discussed in the last subsection. Therefore, if Abell 2744-QSO1 is representative for *JWST*-selected AGN, the (near) Compton-thick obscuration cannot explain the ubiquity of X-ray weakness but might explain the occurrence rate of LRDs among AGN. To check whether a high-C_f model can provide a comparably good fit, we performed a test by fixing $C_f = 0.9$. This produced a significantly worse fit with $\chi^2_\nu = 3.2$, mainly due to the over prediction of the strength of the nebular emission with respect to the strength of the Balmer break. The fit can be improved by increasing the column density, thereby increasing the optical depth of the nebular emission. At $N_{\rm H} = 10^{25}$ cm^{-2}, the fit is improved to have $\chi^2_\nu = 2.1$, but still significantly worse than the fiducial fit. At $N_{\rm H} \gtrsim 10^{25}$ cm^{-2}, the improvement in the fit becomes negligible. While such a high column density possibly exists in some LRDs (e.g. A. Graaff et al. 2025; R. P. Naidu et al. 2025), one needs to start considering the electron scattering optical depth for the optical emission (e.g. S. Panda et al. 2020; V. Rusakov et al. 2025), and we defer the investigation on CLOUDY's calculations in this regime in future work. Overall, while the best-fitting C_f can be affected by other model parameters, whether a high C_f is preferred requires more statistical evidence. Certainly, one should be cautious on the interpretations based on a single target. Also, the above analyses are based on another idealization that all BLR clouds have the same column density.

In addition to the dense gas obscuration, the intrinsic X-ray weakness might occur in Abell 2744-QSO1 due to super-Eddington accretion. L. J. Furtak et al. (2024) estimated a sub-Eddington accretion ratio of ~ 0.3 for Abell 2744-QSO1, and our estimations in Section 5.1 gives $\lambda_{\rm Edd} \sim 0.05 - 0.24$, which put Abell 2744-QSO1 into the sub-Eddington regime. Still, if we assume the scenario proposed by E. Lambrides et al. (2024) and A. Lupi et al. (2024) where the black hole masses of essentially all *JWST*-selected AGN might be overestimated (in our case by a factor of $\gtrsim 3 - 20$ to be compatible with super-Eddington accretion) and thus the Eddington ratios are underestimated, some of the features seen in the observations of Abell 2744-QSO1 including the X-ray weakness might be explained with super-Eddington accretion. The underestimated factor for the mass accretion rate, $\dot{m}/\dot{m}_{\rm Edd}$, can be even larger due to the photon trapping effect at super-Eddington accretion (P. Madau, F. Haardt & M. Dotti 2014; K. Inayoshi et al. 2025). Since $\lambda_{\rm Edd} \propto L_{\rm bol}/M_{\rm BH}$, if $L_{\rm bol}$ is not biased, an underestimation of $\lambda_{\rm Edd}$ by a factor of 20 would mean an overestimation of $M_{\rm BH}$ by the same factor. In Fig. 2, the black hole in Abell 2744-QSO1 would still be overmassive compared to the stellar mass. In terms of dynamical mass, the system will get closer to the J. Kormendy & L. C. Ho (2013) relation, approaching the 1σ dispersion, although one should take into account that the dynamical mass is still a very conservative upper limit. We caution that the potential bias associated with the bolometric conversion to get $L_{\rm bol}$ at the super-Eddington regime is not taken into account in the above estimation.

An additional piece of evidence may potentially come from the strength for high-ionization lines such as He IIλ4686. As shown in Fig. B2, to fit the observed He IIλ4686 together with Balmer emission lines, one can use an AGN SED with super-Eddington accretion, which performs slightly better than the sub-Eddington model. However, as we mentioned in Section 6, the softening of the EUV photons at the super-Eddington regime might not be realistic due to the complete exclusion of the emission within the photon-trapping radius (K. Inayoshi et al. 2025). As a result, further understanding of the effect of the super-Eddington SED is still needed and we leave this investigation to future work.

To distinguish the super-Eddington case from the sub-Eddington case, evidence from the UV/optical variability can also be useful, as the super-Eddington accretion should in principle result in less continuum variability due to photon trapping (K. Inayoshi et al. 2025). As shown in Section 7, there is evidence for the variation in EW(Hβ) over a rest-frame time interval of ~ 2.5 yr, which might be tracing an earlier variation in the continuum if this is real. Still, we note that based on multi-epoch *JWST* and *HST* photometry, most of the *JWST*-selected AGN and LRDs show no evidence for continuum variability (M. Kokubo & Y. Harikane 2024; H. Übler et al. 2024a; Z. Zhang et al. 2025; R. Maiolino et al. 2025b). More photometric/spectroscopic follow-up is needed to understand the variability or the lack thereof in *JWST*-selected AGN and LRDs.

To conclude, Abell 2744-QSO1 serves as an interesting case to test theories of X-ray weakness in *JWST*-selected AGN. The observed Balmer break, if indeed originating in a dense and warm absorber, might also lead to strong absorption of the hard X-ray emission due to Compton down-scattering. However, the best-fitting covering fraction is not high enough to explain the ubiquitous X-ray weakness in *JWST*-selected AGN, if Abell 2744-QSO1 is a representative case. Alternatively, there could be intrinsic X-ray weakness caused by super-Eddington accretion, which is supported by the lack of high-energy photons. In the case of intrinsic X-ray weakness, the covering fraction of Abell 2744-QSO1 might instead imply the fraction of LRDs among *JWST*-selected AGN is ~ 24 per cent, if the physical conditions of its BLR are representative.

8.4 Implications of an overmassive black hole

The finding that the AGN discovered by *JWST* tend to be overmassive relative to the stellar mass of their host galaxies has been reported by several studies (e.g. Y. Harikane et al. 2023; F. Pacucci et al. 2023; H. Übler et al. 2023; Á. Bogdán et al. 2024; L. J. Furtak et al. 2024; I. Juodžbalis et al. 2024b; R. Maiolino et al. 2024b; M. A. Marshall et al. 2025). It has been claimed that part of this offset is due to a much larger dispersion of the $M_{\rm BH} - M_\star$ and selection effects that make overmassive black holes preferentially observed, since they are on average more luminous (H. Zhang et al. 2023; J. Li et al. 2025). Yet, the discovery of highly overmassive and dormant (hence low-luminosity) black holes suggests that the bias and putative high-dispersion effects cannot entirely explain the offset on this relation (I. Juodžbalis et al. 2024b). Regardless of the role of selection effects, the simple finding that even a small fraction of the black holes found by *JWST* are as massive as 10 per cent of the host's stellar mass (or even more), is very important, as it indicates that nature somehow manages to produce such overmassive black holes in the early Universe. Within this context, Abell 2744-QSO1 is a remarkable object as it is not only one of the most overmassive black holes confirmed to date, but also one of the most distant overmassive black holes.

Based on high-resolution spectroscopic data, R. Maiolino et al. (2024b) and H. Übler et al. (2023) found that, in terms of dynamical masses, these early black holes are closer to the local relation. One implication could be that the host galaxies of these black holes have about the right amount of baryonic mass, but that the formation of stars has not been as efficient as the black hole growth. This could be due to the feedback of the black hole during its accretion, although mostly in the form of heating/photo-dissociation feedback, rather than ejective feedback. However, Abell 2744-QSO1 is an interesting object in this context in the sense that its black hole is highly overmassive also relative to the dynamical mass of the host galaxy. Specifically, the conservative upper limit on the dynamical mass indicates that the black hole must be more massive than 10 per cent of the dynamical mass of the host galaxy. If one takes the tentative measurement of the velocity dispersion, then the implied dynamical mass of the host galaxy would be just a factor of about two higher than the black hole mass, meaning that the black hole potentially contributes to the observed dynamical mass.

It is beyond the scope of this paper to explore the possible theoretical implications of this finding. However, we note that highly overmassive black holes are predicted both in scenarios where black holes originate from heavy seeds, such as the so-called Direct Collapse Black Holes (e.g. H. Zhang et al. 2023; A. K. Bhowmick et al. 2024; P. Natarajan et al. 2024), remaining outliers in the population through sustained growth across cosmic times (H. Hu et al. 2022; M. T. Scoggins & Z. Haiman 2024), and/or scenarios in which black holes experience episodes of super-Eddington accretion (e.g. M. Volonteri, J. Silk & G. Dubus 2015; K. Inayoshi et al. 2022; R. Schneider et al. 2023; A. Trinca et al. 2023, 2024; J. S. Bennett et al. 2024; W. Li et al. 2024). These two scenarios are not in conflict, and both of them could apply to different classes of black holes, or even the same objects. Primordial black holes, formed from fluctuation in the early phases after inflation, are also a possible alternative to explain overmassive black holes in the early Universe

(P. Dayal 2024). Many of these studies manage to reproduce the overmassive nature of early black holes on the $M_{\rm BH} - M_{\star}$ relation. However, there has been little effort in exploring the offset on the $M_{\rm BH} - M_{\rm dyn}$ relation. Thus, it is vital in the near future to explore this relation with models and simulations. The extreme properties of objects such as Abell 2744-QSO1 may help to break degeneracies between the models.

8.5 Low metallicity and possible feedback

As already illustrated by L. J. Furtak et al. (2024), the MSA PRISM spectrum of Abell 2744-QSO1 shows peculiar narrow emission lines with very weak [O III]λ5008. Our high-resolution spectrum confirms the weakness of [O III]λ5008, with EW < 3.7 Å. Such a low EW of the [O III]λ5008 has been observed also in many lower redshift quasars. Potential explanations for the weak [O III]λ5008 include very extended NLRs (with sizes larger than the host galaxies, hence running out of gas to ionize; H. Netzer et al. 2004), and the so-called Baldwin effect for [O III]λ5008 caused by the inclinations of the accretion discs (G. Risaliti, M. Salvati & A. Marconi 2011). However, the above explanations were proposed in the context of very luminous quasars ($L_{\rm bol} \approx 10^{46} - 10^{48}$ erg s^{-1}), while Abell 2744-QSO1 is a much lower luminosity AGN ($L_{\rm bol} \approx 0.2 - 1 \times 10^{45}$ erg s^{-1}). Specifically, in terms of bolometric luminosity Abell 2744-QSO1 is similar to many other AGN discovered by *JWST* at high-z (e.g. R. Maiolino et al. 2024b; A. Adamo et al. 2025; J. Scholtz et al. 2025; A. J. Taylor et al. 2025), which are instead characterized by prominent [O III] emission. In principle, the weakness of [O III] could be due to a very low metallicity. However, our high-resolution spectrum reveals that the narrow component of Hβ is relatively weak as well, in contrast to many other *JWST*-discovered Type 1 AGN, whose Hβ emission is dominated by the narrow component (H. Übler et al. 2023, 2024a; R. Maiolino et al. 2024b). The weakness of the narrow Hβ cannot be explained by the low metallicity. One possible explanation for the weak narrow lines is that the host galaxy has experienced a recent strong feedback effect by the AGN, which has removed a large fraction of the ISM in the host galaxy, hence leaving little gas to ionize in the host galaxy (i.e. a very weak NLR).

In Section 6.2.3, based on the fit of the UV continuum, we discuss a scenario where the UV light of Abell 2744-QSO1 is dominated by stellar light. The strong feedback scenario inferred from the weak narrow Hβ implies that the star formation must have quenched in the last few Myr. Under the hypothesis that the UV continuum is dominated by young stars, one additional characteristic of Abell 2744-QSO1 is the mismatch between $M_{\rm UV}$ and the luminosity of Hβ. Specifically, using the UV calibration of R. C. Kennicutt (1998), corrected for a G. Chabrier (2003) initial mass function, we can estimate a star-formation rate (SFR) of 0.2 M$_{\odot}$ yr^{-1} (we assumed a calibration for solar metallicity,$MBlhyp\mathrm{UV}Blhyp - 16.98 \pm 0.09$ mag, L. J. Furtak et al. 2024, and uncertainties on the calibration of 0.3 dex). From the luminosity of the narrow Hβ (Table 1), assuming Case B recombination and the SFR law of A. E. Shapley et al. (2023), we infer an SFR of 0.06 M$_{\odot}$ yr^{-1}. This is a discrepancy of a factor of three, without even considering that any dust attenuation would suppress the UV-inferred SFR more than the SFR based on Hβ, and that the latter estimate assumes no NLR to be present in the AGN. Since the UV and Hβ SFRs trace star formation on time-scales of 100 and 10 Myr, respectively, this mismatch could point to a decreasing SFR trend, reminiscent of rapidly quenched galaxies (V. Strait et al. 2023; T. J. Looser et al. 2024; W. M. Baker et al. 2025) and consistent with the strong-feedback interpretation.

On the other hand, it is also true that Abell 2744-QSO1 has an anomalously low [O III]λ5008 to Hβ flux ratio, which is [O III]/H$\beta_{\rm narrow} = 0.60 \pm 0.18$ from the R2700 BlackTHUNDER spectrum. This [O III]/H$\beta_{\rm narrow}$ is the lowest among all high-z AGN to our best knowledge (e.g. V. Kokorev et al. 2023; M. A. Marshall et al. 2023, 2025; H. Übler et al. 2023, 2024a; R. Maiolino et al. 2024b; B. Trefoloni et al. 2025). Such a low ratio could be due to a very low metallicity in the ISM of the host galaxy. While it is difficult to assess the metallicity without other nebular emission lines, based on the photoionization models presented by K. Nakajima & R. Maiolino (2022), it is possible that the metallicity of the host is below 0.01 $Z_{\odot}$. Such a low metallicity inferred from [O III]/H$\beta_{\rm narrow}$ implies that we might be witnessing the formation of a primeval black hole in a primeval galaxy. Alternatively, the weakness of [O III] relative to Hβ could be a consequence of very high gas density in the ISM of this system. Specifically, if the electron density is higher than the critical density of [O III]λ5008, which is $n_{\rm e;ISM} > n_{\rm [OIII];critical} \sim 10^6$ cm^{-3}, the observed strength of [O III] would be significantly suppressed relative to Hβ (B. T. Draine 2011). However, this scenario would imply that there is no intermediate/low-density gas in the system and that most of the ISM has extremely high densities, which is atypical even in high-z galaxies (e.g. Y. Isobe et al. 2023; S. Li et al. 2025).

9 CONCLUSIONS

In this work, we have presented new NIRSpec-IFU data of a lensed Little Red Dot (LRD) at $z = 7.04$, obtained within the context of the BlackTHUNDER *JWST* Large Programme, using both high (G395H, R~2700) and low (PRISM, R~100) spectral resolution modes. We also re-analysed archival, low-resolution MSA spectra of the three images of the lensed LRD.

The spectrum confirms a prominent, but smooth Balmer break and the presence of broad Balmer lines tracing the BLR of an AGN. We also detect a very narrow component of Hβ and [O III]λ5008 emission and tentative (3.2σ) Hβ absorption. By analysing these spectral properties in detail, we reach the conclusions listed below.

(i) Assuming local virial relations, we infer a black hole mass of $4^{+4}_{-2} \times 10^7$ M$_{\odot}$. The black hole is estimated to accrete at an Eddington ratio of $\lambda_{\rm Edd} = L_{\rm bol}/L_{\rm Edd} \approx 0.05 - 0.24$, depending on whether the bolometric luminosity is measured assuming bolometric corrections from the Hβ luminosity or from the optical continuum (L_{5100}).

(ii) The narrow component of Hβ is extremely narrow, unresolved (conservatively, $\sigma < 47$ km s^{-1}). This, together with the compact size of the galaxy, was used to set an tight, conservative upper limit on the dynamical mass of $M_{\rm dyn} < 4 \times 10^8$ M$_{\odot}$, which is one order of magnitude lower than the stellar mass of the galaxy inferred when assuming that the Balmer break and optical continuum are of stellar origin (4×10^9 M$_{\odot}$). Our finding indicates that the stellar light cannot contribute more than 10 per cent (very conservatively) to the Balmer break and to the optical continuum.

(iii) We have shown that the Black Hole in Abell 2744-QSO1 is overmassive, by $\sim 1 - 2$ orders of magnitude relative to both the stellar *and* dynamical mass of the host galaxy, when compared to local scaling relations. This is the first high-z black hole found to be so overmassive on both scaling relations, and may have important implication understanding the seeding and early growth of black holes.

(iv) The Balmer break-like feature in the PRISM spectrum of Abell 2744-QSO1 can be described by absorption from dust-free dense gas, likely originating in the BLR. Specifically, we have shown that the spectrum can be well fit by a model composed of an optical part dominated by AGN continuum attenuated by dust-free gas in the BLR along the line of sight, and then by a dust screen outside (or in the outer parts of the BLR). The UV part is dominated by a less attenuated continuum of an AGN (either scattered or transmitted through partial covering) or from a young stellar population. Based on our fiducial model, the dense absorbing gas has a density of $n_{\rm H} = 10^{10}$ cm^{-3}, a column density of at least $N_{\rm H} = 10^{24}$ cm^{-2}, an ionization parameter of $U = 10^{-1.5}$, and a microturbulence velocity of $v_{\rm turb} = 120$ km s^{-1}. Our modelling approach provides a better fit to the spectrum of Abell 2744-QSO1 compared to previous works that assume a stellar Balmer break.

(v) This non-stellar origin for the Balmer break has the advantages of not invoking a high stellar mass that is inconsistent with the inferred dynamical mass and which would result in an extremely high stellar density; it does not require a peculiar shape of the attenuation curve, and does not imply extremely high intrinsic equivalent widths for broad emission lines.

(vi) Our fiducial model also predicts an absorption line in Hβ with an equivalent width of 8.0 Å with respect to the continuum. This value is consistent, within 1.1σ with the tentative Hβ absorption that we measured from the high-resolution ($R \sim 2700$) IFU spectrum of Abell 2744-QSO1, which has an EW of $5.5^{+2.2}_{-1.7}$ Å. Further tuning of the model parameters can result in even better consistency.

(vii) The shape of the Balmer break in our model depends on various model parameters. Specifically, a microturbulence velocity of $v_{\rm turb} \sim 100$ km s^{-1} is needed to recover the smooth Balmer break observed in Abell 2744-QSO1, which is caused by the superpositions of deep Balmer absorption lines near the Balmer limit. The variation in the microturbulence velocity could lead to different shapes of the Balmer break and might explain the diversity of the break seen in other *JWST*-discovered LRDs.

(viii) Potentially, the Balmer break of other LRDs may be explained with the same scenario of AGN continuum and dense gas absorption, especially given that at least 20 per cent of the LRDs present evidence of Hα absorption. A non-stellar origin of the Balmer break in LRDs would greatly alleviate the extreme stellar mass densities in these systems, as well as the extremely high stellar mass density per cosmic volume, inferred when assuming a stellar origin of the Balmer breaks. Studies such as the one performed here on other LRDs can clarify this aspect.

(ix) The rest-frame UV continuum of Abell 2744-QSO1 likely has a different origin compared to the optical continuum.
The UV continuum can be described by an AGN/SF continuum with a small amount of dust attenuation ($A_{\rm V} \sim 0.1$) and a damped Lyα absorber with $N_{\rm HI} \sim 3 \times 10^{21}$ cm^{-2}, although we cannot fully exclude the scenario where the UV continuum is instead nebular dominated. The nebular dominated scenario would require a temperature of $T_e \sim 30\,000$ K and the normalization of the continuum model might not be entirely physical.
Overall, the UV continuum likely comes from a more extended region compared to the optical part due to the significantly lower gas column density and dust attenuation. Alternatively, the UV could potentially also be AGN light transmitted through a partial covering absorber.

(x) The lack of hard X-ray emission in Abell 2744-QSO1 might be related to the presence of the dense gas along the line of sight in our model, whose lower limit on the column density is close to the Compton-thick regime. If the X-ray weakness is indeed due to Compton-thick absorption within the BLR, our best-fitting covering fraction of the BLR clouds implies 24 per cent of the *JWST*-discovered AGN are X-ray weak, which is significantly lower than the observed fraction of ∼ 90 per cent. Meanwhile, if we interpret the dense gas obscuration as the necessary condition for LRDs, this result implies 24 per cent of the *JWST*-discovered AGN are LRDs, which is consistent with the value of ∼ 30 per cent currently found in observations. It is possible that for the remaining part of non-LRD AGN (about 70 per cent of them), the X-ray weakness is intrinsic due to, for example, high accretion rates.

(xi) Super-Eddington accretion can explain the X-ray weakness and potentially the weakness of He IIλ4686 in the PRISM spectrum of Abell 2744-QSO1. However, this scenario requires an overestimation of the black hole mass by a factor of $\gtrsim 3-20$ and the extreme UV part of the super-Eddington SED remains to be examined carefully.

(xii) We have found evidence for a higher equivalent width of the Balmer lines in one of the three lensed images of Abell 2744-QSO1, specifically image C, relative to the other two images. We note that a variation in EW cannot be ascribed to any calibration issues. This finding can be explained in terms of a drop of the continuum flux in image C and the fact that the BLR has not yet responded to the ionizing flux variation because of its size. This interpretation is supported by the finding that the flux observed in image C a few months before the spectroscopic observation was about a factor of two higher.

(xiii) We used this information to attempt a first reverberation mapping at such an early epoch, which would make this source consistent with the relation between $R_{\rm BLR}$ and L_{5100} found in local reverberation studies.

(xiv) Abell 2744-QSO1has the lowest EW([O III]λ5008) among all *JWST*-discovered AGN, and also the weakest Hβ narrow relative to the broad component. These features may indicate that the AGN has exerted extremely strong feedback, removing most of the ISM in the host galaxy and possibly quenching star formation.

(xv) Abell 2744-QSO1 has the lowest flux ratio between [O III]λ5008 and the narrow Hβ among all high-z AGNs, with [O III]λ5008/H$\beta_{\rm narrow} = 0.60 \pm 0.18$. This indicates that the host galaxy of this black hole is very metal poor (possibly $Z < 10^{-2}\,Z_\odot$). Alternatively, very high electron densities ($n_{\rm e} > 10^6$ cm^{-3}) in the ISM may suppress [O III]λ5008 relative to Hβ.

As a concluding remark, the case study of Abell 2744-QSO1 provides clues for deciphering the physical conditions of LRDs and AGN discovered by *JWST*, and demonstrates the need for deep and high spectral resolution observations that help differentiate AGN and stellar scenarios. It remains to be explored in future work whether the SED modelling approach proposed in this work can be generalized to other LRD AGNs, and whether the X-ray weakness in these sources is related to the inferred properties. Furthermore, it would be important to perform a statistical analysis to understand how the inferred physical conditions are changing with redshift and whether this explains the significantly reduced number of LRDs at low redshift.

ACKNOWLEDGEMENTS

We thank the anonymous referee, whose thoughtful suggestions improved the clarity of this work. We thank Gary Ferland and T. Taro Shimizu for helpful discussions. We thank L. Furtak for providing the combined spectrum of the three images presented in their work. XJ and RM acknowledge ERC Advanced Grant 695671 'QUENCH' and support by the Science and Technology Facilities Council (STFC) and by the UKRI Frontier Research grant RISEandFALL. RM acknowledges funding from a research professorship from the Royal Society. HÜ acknowledges funding by the European Union (ERC APEX, 101164796). Views and opinions expressed are, however, those of the authors only and do not necessarily reflect those of the European Union or the European Research Council Executive Agency. Neither the European Union nor the granting authority can be held responsible for them. MP acknowledges grant PID2021-127718NB-I00 funded by the Spanish Ministry of Science and Innovation/State Agency of Research (MICIN/AEI/10.13039/501100011033). MP also acknowledges support through the grant RYC2023-044853-I, funded by MICIU/AEI/10.13039/501100011033 and FSE+. KI acknowledges support from the National Natural Science Foundation of China (12073003, 12003003, 11721303, 11991052, 11950410493), and the China Manned Space Project (CMS-CSST-2021-A04 and CMS-CSST-2021-A06). AJB acknowledges funding from the 'First-Galaxies' Advanced Grant from the European Research Council (ERC) under the European Union's Horizon 2020 research and innovation program (Grant agreement No. 789056). SC, EP, and GV acknowledge support by European Union's HE ERC Starting Grant No. 101040227–WINGS.

This work is based on observations made with the NASA/ESA/CSA *James Webb Space Telescope*. The data are available at the Mikulski Archive for Space Telescopes (MAST) at the Space Telescope Science Institute, which is operated by the Association of Universities for Research in Astronomy, Inc., under NASA contract NAS 5–03127 for *JWST*. These observations are associated with the programmes, BlackTHUNDER (PID 5015; PIs: H. Übler, R. Maiolino) and UNCOVER (PID 2561; PIs: I. Labbé, R. Bezanson).

DATA AVAILABILITY

All analysis results of this paper will be shared on reasonable request to the corresponding author. The NIRCam cutouts of Fig. 1 were made from publicly available mosaics from UNCOVER DR4 (S. H. Price et al. 2025). The NIRSpec observations used in this paper are available through the MAST portal.

REFERENCES

Abramowicz M. A., Czerny B., Lasota J. P., Szuszkiewicz E., 1988, ApJ, 332, 646
Abuter R. et al., 2024, Nature, 627, 281
Adamo A. et al., 2025, Nat. Astron., 9, 1134
Akins H. B. et al., 2025a, preprint (arXiv:2503.00998)
Akins H. B. et al., 2025b, ApJ, 991, 37
Ananna T. T., Bogdán Á., Kovács O. E., Natarajan P., Hickox R. C., 2024, ApJ, 969, L18
Baggen J. F. W. et al., 2024, ApJ, 977, L13
Baker W. M. et al., 2025, A&A, 697, A90
Baldwin J. A., Phillips M. M., Terlevich R., 1981, PASP, 93, 5
Baldwin J. A., Ferland G. J., Korista K. T., Hamann F., LaCluyzé A., 2004, ApJ, 615, 610
Bennett J. S., Sijacki D., Costa T., Laporte N., Witten C., 2024, MNRAS, 527, 1033
Bentz M. C., Manne-Nicholas E., 2018, ApJ, 864, 146
Bentz M. C. et al., 2013, ApJ, 767, 149
Bergamini P. et al., 2023, ApJ, 952, 84
Bezanson R. et al., 2018, ApJ, 868, L36
Bezanson R. et al., 2024, ApJ, 974, 92
Bhowmick A. K. et al., 2024, MNRAS, 533, 1907
Bogdán Á. et al., 2024, Nat. Astron., 8, 126
Böker T. et al., 2022, A&A, 661, A82
Böker T. et al., 2023, PASP, 135, 038001
Bottorff M. C., Ferland G. J., 2000, MNRAS, 316, 103
Bottorff M., Ferland G., Baldwin J., Korista K., 2000, ApJ, 542, 644
Bottorff M. C., Ferland G. J., Straley J. P., 2006, PASP, 118, 1176
Brazzini M., D'Eugenio F., Maiolino R., Juodžbalis I., Ji X., Scholtz J., 2025, preprint (arXiv:2507.08929)
Burke C. J. et al., 2021, Science, 373, 789
Calzetti D., Armus L., Bohlin R. C., Kinney A. L., Koornneef J., Storchi-Bergmann T., 2000, ApJ, 533, 682
Cameron A. J., Katz H., Witten C., Saxena A., Laporte N., Bunker A. J., 2024, MNRAS, 534, 523
Cappellari M., 2017, MNRAS, 466, 798
Cappellari M., Emsellem E., 2004, PASP, 116, 138
Cappellari M. et al., 2006, MNRAS, 366, 1126
Cappellari M. et al., 2013, MNRAS, 432, 1709
Carnall A. C., 2017, preprint (arXiv:1705.05165)
Carnall A. C. et al., 2023, Nature, 619, 716
Carniani S. et al., 2015, A&A, 580, A102
Chabrier G., 2003, ApJ, 586, L133
Chang S.-J., Gronke M., Matthee J., Mason C., 2025, preprint (arXiv:2508.08768)
Chisholm J. et al., 2024, MNRAS, 534, 2633
D'Eugenio F. et al., 2024, Nat. Astron., 8, 1443
D'Eugenio F. et al., 2025a, preprint (arXiv:2503.11752)
D'Eugenio F. et al., 2025b, preprint (arXiv:2506.14870)
D'Eugenio F. et al., 2025c, ApJS, 277, 4
Dai L., McKinney J. C., Roth N., Ramirez-Ruiz E., Miller M. C., 2018, ApJ, 859, L20
Davies R. L. et al., 2021, ApJ, 909, 78
Dayal P., 2024, A&A, 690, A182
Dere K. P., Landi E., Mason H. E., Monsignori Fossi B. C., Young P. R., 1997, A&AS, 125, 149
Díaz-Santos T. et al., 2021, A&A, 654, A37
Dimitrijević M. S., Popović L. Č., Kovačević J., Dačić M., Ilić D., 2007, MNRAS, 374, 1181
Ding X. et al., 2023, Nature, 621, 51
van Dokkum P. G., 2001, PASP, 113, 1420
Dong X., Wang T., Wang J., Yuan W., Zhou H., Dai H., Zhang K., 2008, MNRAS, 383, 581
Dorner B. et al., 2016, A&A, 592, A113
Draine B. T., 2011, Physics of the Interstellar and Intergalactic Medium. Princeton Univ. Press, Princeton, NJ
Du P. et al., 2015, ApJ, 806, 22
Du P. et al., 2016, ApJ, 825, 126
Eftekhari F. S. et al., 2022, MNRAS, 517, 4714
Fabian A. C., Vasudevan R. V., Gandhi P., 2008, MNRAS, 385, L43
Ferland G. J., Hu C., Wang J.-M., Baldwin J. A., Porter R. L., van Hoof P. A. M., Williams R. J. R., 2009, ApJ, 707, L82
Ferland G. J. et al., 2017, Rev. Mex. Astron. Astrofis., 53, 385
Ferland G. J., Done C., Jin C., Landt H., Ward M. J., 2020, MNRAS, 494, 5917
Finn C. W. et al., 2014, MNRAS, 440, 3317
Foreman-Mackey D., Hogg D. W., Lang D., Goodman J., 2013, PASP, 125, 306
Furtak L. J. et al., 2023, ApJ, 952, 142
Furtak L. J. et al., 2024, Nature, 628, 57
Gaia Collaboration, 2023, A&A, 674, A1
Gaskell C. M., 1980, The Observatory, 100, 148
Gaskell C. M., 2009, New Astron. Rev., 53, 140
Gordon K. D., Clayton G. C., Misselt K. A., Landolt A. U., Wolff M. J., 2003, ApJ, 594, 279
Goulding A. D. et al., 2023, ApJ, 955, L24
de Graaff A. et al., 2024, A&A, 684, A87
de Graaff A. et al., 2025, A&A, 701, A168
Grandi S. A., 1982, ApJ, 255, 25
Greene J. E., Ho L. C., 2005, ApJ, 630, 122
Greene J. E., Strader J., Ho L. C., 2020, ARA&A, 58, 257
Greene J. E. et al., 2024, ApJ, 964, 39
Grevesse N., Asplund M., Sauval A. J., Scott P., 2010, Ap&SS, 328, 179
Guia C. A., Pacucci F., Kocevski D. D., 2024, Res. Notes Am. Astron. Soc., 8, 207

Hainline K. N. et al., 2025, ApJ, 979, 138
Hall P. B., 2007, AJ, 133, 1271
Harikane Y. et al., 2023, ApJ, 959, 39
Ho L. C., Kim M., 2014, ApJ, 789, 17
Hopkins P. F., Murray N., Quataert E., Thompson T. A., 2010, MNRAS, 401, L19
Hu H., Inayoshi K., Haiman Z., Li W., Quataert E., Kuiper R., 2022, ApJ, 935, 140
Hu W. et al., 2023, ApJ, 956, 39
Inayoshi K., Ichikawa K., 2024, ApJ, 973, L49
Inayoshi K., Maiolino R., 2025, ApJ, 980, L27
Inayoshi K., Nakatani R., Toyouchi D., Hosokawa T., Kuiper R., Onoue M., 2022, ApJ, 927, 237
Inayoshi K., Kimura S. S., Noda H., 2025, PASJ, 77, 811
Inoue A. K., 2011, MNRAS, 415, 2920
Isobe Y., Ouchi M., Nakajima K., Harikane Y., Ono Y., Xu Y., Zhang Y., Umeda H., 2023, ApJ, 956, 139
Izumi T. et al., 2019, PASJ, 71, 111
Jakobsen P. et al., 2022, A&A, 661, A80
Ji X., Yan R., Riffel R., Drory N., Zhang K., 2020, MNRAS, 496, 1262
Ji X. et al., 2025, preprint (arXiv:2507.23774)
Juodžbalis I. et al., 2024a, MNRAS, 535, 853
Juodžbalis I. et al., 2024b, Nature, 636, 594
Juodžbalis I. et al., 2025a, preprint (arXiv:2504.03551)
Juodžbalis I. et al., 2025b, preprint (arXiv:2508.21748)
Kennicutt R. C., Jr, 1998, ARA&A, 36, 189
Killi M. et al., 2024, A&A, 691, A52
King A., 2024, MNRAS, 531, 550
Kocevski D. D. et al., 2023, ApJ, 954, L4
Kocevski D. D. et al., 2025, ApJ, 986, 126
Kokorev V. et al., 2023, ApJ, 957, L7
Kokubo M., Harikane Y., 2024, preprint (arXiv:2407.04777)
Kormendy J., Ho L. C., 2013, ARA&A, 51, 511
Kubota A., Done C., 2019, MNRAS, 489, 524
Labbé I. et al., 2024, preprint (arXiv:2412.04557)
Lambrides E. et al., 2024, preprint (arXiv:2409.13047)
Landi E., Young P. R., Dere K. P., Del Zanna G., Mason H. E., 2013, ApJ, 763, 86
Larson R. L. et al., 2023, ApJ, 953, L29
Laseter I. H. et al., 2024, A&A, 681, A70
Li J. et al., 2025, ApJ, 981, 19
Li S. et al., 2025, ApJ, 979, L13
Li W. et al., 2024, ApJ, 969, 69
Li Z., Inayoshi K., Chen K., Ichikawa K., Ho L. C., 2025, ApJ, 980, 36
Liddle A. R., 2007, MNRAS, 377, L74
Lin X. et al., 2024, ApJ, 974, 147
Lin X. et al., 2025, preprint (arXiv:2507.10659)
Longair M. S., 2011, High Energy Astrophysics. Cambridge Univ. Press, Cambridge
Looser T. J. et al., 2024, Nature, 629, 53
Lupi A., Trinca A., Volonteri M., Dotti M., Mazzucchelli C., 2024, A&A, 689, A128
Luridiana V., Morisset C., Shaw R. A., 2015, A&A, 573, A42
Lusso E., Risaliti G., 2017, A&A, 602, A79
Lyu J. et al., 2024, ApJ, 966, 229
Ma Y. et al., 2025, ApJ, 981, 191
MacLeod C. L. et al., 2010, ApJ, 721, 1014
Madau P., 2025, preprint (arXiv:2501.09854)
Madau P., Haardt F., 2024, ApJ, 976, L24
Madau P., Haardt F., Dotti M., 2014, ApJ, 784, L38
Maiolino R. et al., 2024a, Nature, 627, 59
Maiolino R. et al., 2024b, A&A, 691, A145
Maiolino R. et al., 2025a, preprint (arXiv:2505.22567)
Maiolino R. et al., 2025b, MNRAS, 538, 1921
Marconcini C. et al., 2023, A&A, 677, A58
Marshall M. A. et al., 2023, A&A, 678, A191
Marshall M. A. et al., 2025, A&A, 702, A50
Matthee J. et al., 2024, ApJ, 963, 129
Mazzolari G. et al., 2024a, preprint (arXiv:2412.04224)
Mazzolari G. et al., 2024b, A&A, 691, A345
Mazzolari G. et al., 2025, A&A, 700, A12
Naidu R. P. et al., 2024, preprint (arXiv:2410.01874)
Naidu R. P. et al., 2025, preprint (arXiv:2503.16596)
Nakajima K., Maiolino R., 2022, MNRAS, 513, 5134
Natarajan P., Pacucci F., Ricarte A., Bogdán Á., Goulding A. D., Cappelluti N., 2024, ApJ, 960, L1
Netzer H., 1990, in Blandford R. D., Netzer H., Woltjer L., Courvoisier T. J. L., Mayor M., eds, Active Galactic Nuclei. Springer-Verlag, Berlin, p. 57
Netzer H., Laor A., 1993, ApJ, 404, L51
Netzer H., Shemmer O., Maiolino R., Oliva E., Croom S., Corbett E., di Fabrizio L., 2004, ApJ, 614, 558
Neumayer N., Seth A., Böker T., 2020, A&AR, 28, 4
Ormerod K. et al., 2024, MNRAS, 527, 6110
Osterbrock D. E., Ferland G. J., 2006, Astrophysics of Gaseous Nebulae and Active Galactic Nuclei. University Science Books, Sausalito, CA
Pacucci F., Narayan R., 2024, ApJ, 976, 96
Pacucci F., Nguyen B., Carniani S., Maiolino R., Fan X., 2023, ApJ, 957, L3
Panda S., Martínez-Aldama M. L., Marinello M., Czerny B., Marziani P., Dultzin D., 2020, ApJ, 902, 76
Pascalau R. G. et al., 2025, preprint (arXiv:2505.06349)
Peimbert M., 1967, ApJ, 150, 825
Pensabene A., Carniani S., Perna M., Cresci G., Decarli R., Maiolino R., Marconi A., 2020, A&A, 637, A84
Pérez-González P. G. et al., 2024, ApJ, 968, 4
Perna M. et al., 2023, A&A, 679, A89
Perna M. et al., 2025, A&A, 696, A59
Pezzulli E., Valiante R., Orofino M. C., Schneider R., Gallerani S., Sbarrato T., 2017, MNRAS, 466, 2131
Pfister H., Volonteri M., Dai J. L., Colpi M., 2020, MNRAS, 497, 2276
Planck Collaboration VI, 2020, A&A, 641, A6
Price S. H. et al., 2025, ApJ, 982, 51
Raiter A., Schaerer D., Fosbury R. A. E., 2010, A&A, 523, A64
Rauscher B. J. et al., 2017, PASP, 129, 105003
Reddy N. A. et al., 2015, ApJ, 806, 259
Reines A. E., Volonteri M., 2015, ApJ, 813, 82
Risaliti G., Salvati M., Marconi A., 2011, MNRAS, 411, 2223
Rodríguez Del Pino B. et al., 2024, A&A, 684, A187
Rusakov V. et al., 2025, preprint (arXiv:2503.16595)
Santos D. J. D. et al., 2025, A&A, 696, A30
Sarkar A. et al., 2021, ApJ, 907, 12
Schaerer D., 2002, A&A, 382, 28
Schneider R., Valiante R., Trinca A., Graziani L., Volonteri M., Maiolino R., 2023, MNRAS, 526, 3250
Scholtz J. et al., 2025, A&A, 697, A175
Scoggins M. T., Haiman Z., 2024, MNRAS, 531, 4584
Setton D. J. et al., 2024, preprint (arXiv:2411.03424)
Shakura N. I., Sunyaev R. A., 1973, A&A, 24, 337
Shapley A. E., Sanders R. L., Reddy N. A., Topping M. W., Brammer G. B., 2023, ApJ, 954, 157
Shields G. A., Ludwig R. R., Salviander S., 2010, ApJ, 721, 1835
Simmonds C. et al., 2024, MNRAS, 535, 2998
Stern J., Laor A., 2012, MNRAS, 423, 600
Stone M. A., Lyu J., Rieke G. H., Alberts S., Hainline K. N., 2024, ApJ, 964, 90
Strait V. et al., 2023, ApJ, 949, L23
Tacchella S. et al., 2025, MNRAS, 540, 851
Taylor A. J. et al., 2025, ApJ, 986, 165
Toloba E. et al., 2014, ApJS, 215, 17
Tozzi G., Maiolino R., Cresci G., Piotrowska J. M., Belfiore F., Curti M., Mannucci F., Marconi A., 2023, MNRAS, 521, 1264
Trefoloni B. et al., 2025, A&A, 700, A203
Trinca A., Schneider R., Maiolino R., Valiante R., Graziani L., Volonteri M., 2023, MNRAS, 519, 4753
Trinca A. et al., 2024, preprint (arXiv:2412.14248)
Tripodi R. et al., 2024, preprint (arXiv:2412.04983)
Übler H. et al., 2023, A&A, 677, A145

Übler H. et al., 2024a, MNRAS, 531, 355
Übler H. et al., 2024b, MNRAS, 533, 4287
van der Wel A. et al., 2022, ApJ, 936, 9
Vanden Berk D. E. et al., 2001, AJ, 122, 549
Veilleux S., Osterbrock D. E., 1987, ApJS, 63, 295
Vestergaard M., Peterson B. M., 2006, ApJ, 641, 689
Volonteri M., Silk J., Dubus G., 2015, ApJ, 804, 148
Volonteri M., Reines A. E., Atek H., Stark D. P., Trebitsch M., 2017, ApJ, 849, 155
Volonteri M. et al., 2025, A&A, 695, A33
Wang B. et al., 2024, ApJ, 969, L13
Wang B. et al., 2025, ApJ, 984, 121
Witstok J. et al., 2025, Nature, 639, 897
Wu S. et al., 2024, MNRAS, 532, 4703
Yue M. et al., 2024a, ApJ, 966, 176
Yue M., Eilers A.-C., Ananna T. T., Panagiotou C., Kara E., Miyaji T., 2024b, ApJ, 974, L26
Zackrisson E., Rydberg C.-E., Schaerer D., Östlin G., Tuli M., 2011, ApJ, 740, 13
Zamorani G. et al., 1981, ApJ, 245, 357
Zhang H., Behroozi P., Volonteri M., Silk J., Fan X., Aird J., Yang J., Hopkins P. F., 2023, MNRAS, 523, L69
Zhang Z., Jiang L., Liu W., Ho L. C., 2025, ApJ, 985, 119

APPENDIX A: LENS MODELLING

The lens magnification factors and time delays are not the focus of this paper, and our results are largely unaffected by the details of the lens model. However, in this section we very briefly summarize the results of previous lens models for the three images of Abell 2744-QSO1, and we also present an independent analysis.

L. J. Furtak et al. (2023, 2024) use the wealth of data available for this cluster to model the lensing of the three images of Abell 2744-QSO1. They obtain that the magnification factors for the three images are $\mu_{\rm A} = 6.15^{+0.77}_{-0.39}$, $\mu_{\rm B} = 7.29^{+0.36}_{-2.18}$, and $\mu_{\rm C} = 3.55^{+0.25}_{-0.24}$. They also estimate the time delays between the three images: image A follows image C by about ~ 19 yr, while image B follows image A by about ~ 3 yr (although these values were estimated by L. J. Furtak et al. 2023, based on the photometric redshift of the source).

We have independently validated these quantities, for each of the three images, by using the high-precision strong lens model derived from *JWST* observations by P. Bergamini et al. (2023). We obtain the following lens magnifications: $\mu_{\rm A} = 5.8^{+0.4}_{-0.2}$, $\mu_{\rm B} = 9.1^{+0.9}_{-0.8}$, and $\mu_{\rm C} = 3.2^{+0.1}_{-0.1}$, respectively. Additionally, we find a delay between the arrival of images C and A of $\tau = 17.9^{+0.3}_{-0.5}$ yr and $\tau = 2.2^{+0.1}_{-0.1}$ yr between images A and B. While these results are broadly consistent with those of the L. J. Furtak et al. (2023, 2024) analysis, they underscore the inherent uncertainties and systematic biases that can arise from the choice of the lens model.

APPENDIX B: FITS BASED ON MODELS WITH DIFFERENT PARAMETERS

In this section, we show additional fitting results based on different model assumptions. In Section 6, we introduced a range of ionization parameters to describe the properties of the warm absorber that produces the Balmer break as well as the tentative Hβ absorption in Abell 2744-QSO1. In Fig. B1, we compare best-fitting models with different ionization parameters in a range of $U = 10^{-2} - 10^{-1}$ for the warm absorber. All the other parameters are fixed to the fiducial values listed in Table 2. One can see the main effect of the ionization parameter is to change the relative strength of the nebular emission with respect to the continuum. At $U = 10^{-2}$, the ionization parameter is relatively low and the strength of Hγ is clearly underpredicted. In contrast, at $U = 10^{-1}$, Hβ is slightly weaker compared to the observation. The choice of the ionization parameter also impacts the best-fitting covering fraction, C_f. For example, at the highest ionization parameter of $U = 10^{-1}$, the best-fitting covering fraction increases to $C_f = 0.34$ compared to the fiducial case of

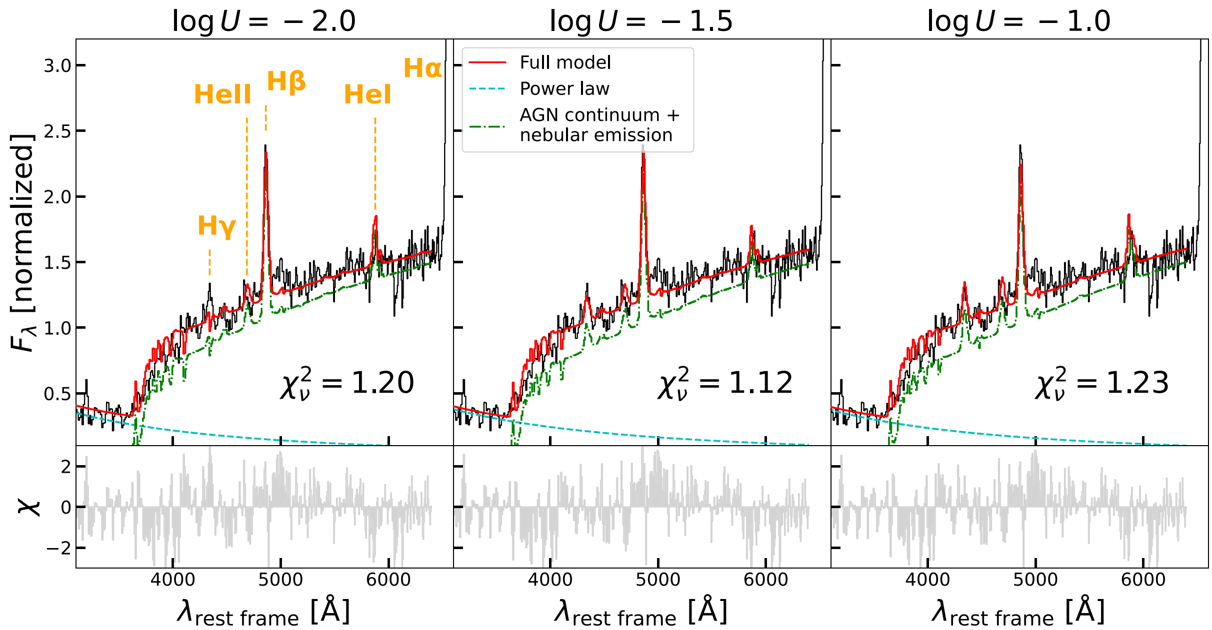

Figure B1. Best-fitting models for the combined spectrum of images A + C of Abell 2744-QSO1 with the GTO reduction in the rest-frame wavelength range of 1600 – 6400 Å. We compare three different ionization parameters for the dense gas that absorbs the AGN continuum, which are $U = 10^{-2}$, $10^{-1.5}$, and 10^{-1}. The observed spectrum is plotted as the solid black line. In each panel, we show the resulting χ of the fit.

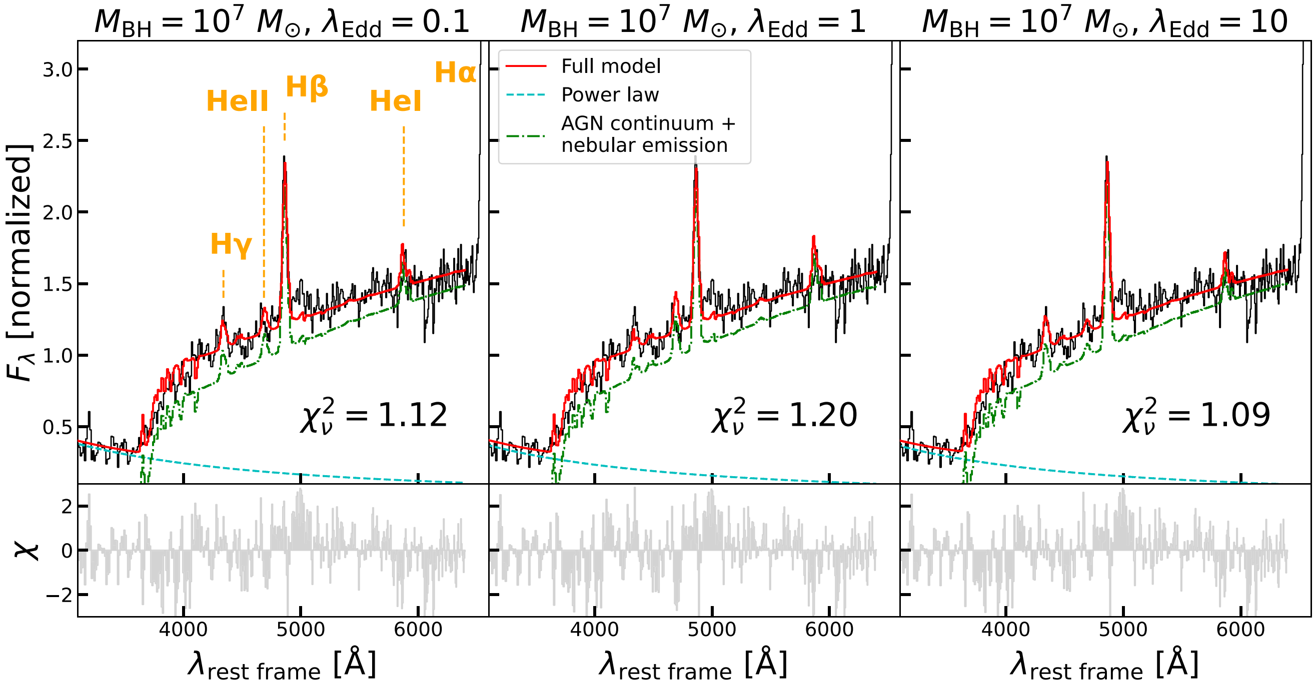

Figure B2. Comparison between three fits to the PRISM spectrum of Abell 2744-QSO1 using different AGN SEDs with $\lambda_{\rm Edd} = 0.1$, 1, and 10 zoomed in the rest-frame optical. The observed spectrum is from the GTO reduced A + C images and is plotted in solid black. The bottom panels show χ of the fits calculated for each pixel. In each panel, we also show the reduced χ^2 of the fit. The main differences between the fits are the nebular emission in Hγ, He IIλ4686, and He Iλ5876. Overall the super-Eddington case with $\lambda_{\rm Edd} = 10$ provides the best fit, but only marginally relative to the sub-Eddington fit with $\lambda_{\rm Edd} = 0.1$.

$C_f = 0.24$ at $U = 10^{-1.5}$. In comparison, at $U = 10^{-2}$, the best-fitting covering fraction slightly decreases to $C_f = 0.23$. Overall, the model with out fiducial ionization parameter, $U = 10^{-1.5}$, produces the best fit, although the differences between the χ^2_ν of the fit is not large.

Fig. B2 compares fitting results with three different Eddington ratios, $\lambda_{\rm Edd} = 0.1$, 1, and 10, for the input SEDs. The most notable difference is in the nebular emission. When $\lambda_{\rm Edd} = 0.1$, the strengths of He IIλ4686 and He Iλ5876 from the BLR is slightly overpredicted. When $\lambda_{\rm Edd} = 1$, He IIλ4686 and He Iλ5876 are further overpredicted but Hγ is underpredicted. The smallest reduced χ^2 is achieved at $\lambda_{\rm Edd} = 10$. The above difference is mainly driven by the hardness of the ionizing radiation, which is generally too hard for Abell 2744-QSO1 at the sub-Eddington regime. This is consistent with the recent finding of E. Lambrides et al. (2024), who claimed that *JWST*-selected Type 1 AGN generally show softer SEDs compared to those expected at the sub-Eddington regime. Still, the difference in the reduced χ^2 between the super-Eddington case and the sub-Eddington case is only 0.05. Also, based on our derivation in Section 5.1, Abell 2744-QSO1 is more likely to host a sub-Eddington AGN. In addition, according to K. Inayoshi et al. (2025), the UV spectrum of a super-Eddington AGN should actually become harder due to the emission from the hotter part of the accretion disc within the photon-trapping radius. This is in contrast to the SED model we took from E. Pezzulli et al. (2017), which does not include the emission within the photon-trapping radius. Finally, we note that different from the fiducial case ($\lambda_{\rm Edd} = 0.1$) where the best-fitting covering fraction is 0.24, the near-Eddington case ($\lambda_{\rm Edd} = 1$) yields a best-fitting covering fraction of 0.22, and the super-Eddington case a best-fitting covering fraction of 0.46.

APPENDIX C: FITTING OF SPECTRA WITH DIFFERENT REDUCTIONS

In this section we show the fitting results for NIRSpec MSA and IFU PRISM spectra with different data reductions. The first spectrum we used is the same spectrum adopted by L. J. Furtak et al. (2024), which combines MSA PRISM spectra from three images of Abell 2744-QSO1 following the reduction process detailed in L. J. Furtak et al. (2024). The second spectrum we used is the PRISM spectrum integrated from the IFU observation of BlackTHUNDER, of which is data reduction process is given in Section 2. The BlackTHUNDER PRISM spectrum is only for the image A of Abell 2744-QSO1. The third spectrum we used is the same spectrum adopted by Y. Ma et al. (2025), which is the MSA PRISM spectrum for image A of Abell 2744-QSO1 from the UNCOVER DR4. The data reduction is given by S. H. Price et al. (2025) and also summarized by Y. Ma et al. (2025). We summarize the best-fitting model parameters for these spectra in Table 3.

Fig. C1 shows our fiducial fit to the spectrum reduced by L. J. Furtak et al. (2024). The photoionization model parameters we used to compute the attenuated AGN continuum are the fiducial set given in Table 2. Compared to the fit to the A + C images, the best-fitting model for the spectrum reduced by L. J. Furtak et al. (2024) yields a larger χ^2_ν (which is still significantly lower than the $\chi^2_\nu \sim 3$ reported by Y. Ma et al. 2025 using alternative models). The UV part appears less well fitted by a featureless power law and shows continuous flux excess around 2000–3000 Å. The resulting UV slope is shallower than the one fitted for the A + C images, leading to a longer tail in the optical and thus requiring an $A_{\rm V}$ 0.26 magnitudes higher than that of the A + C images (cf. Table 3). Fig. C2 shows fits to the L. J. Furtak et al. (2024)'s spectrum with different UV models for a wavelength

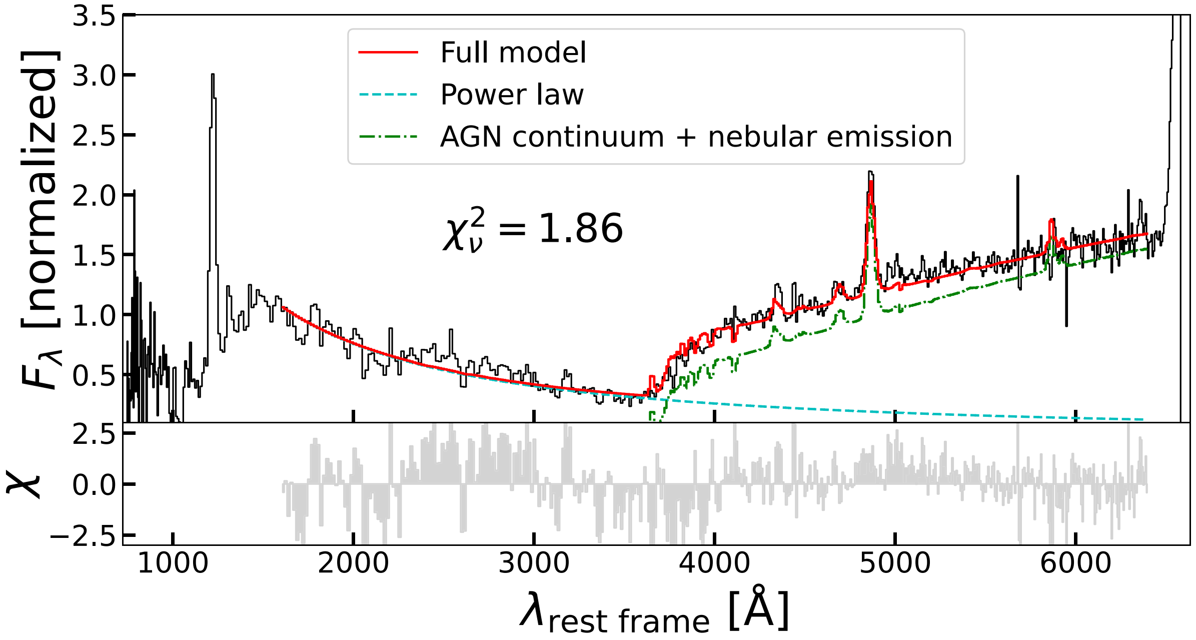

Figure C1. Fiducial fit for the combined images of A + B + C reduced by L. J. Furtak et al. (2024) in the rest-frame wavelength range of 1600 − 6400 Å. The observed PRISM spectrum is normalized to the flux density at $\lambda = 4260$ Å in the rest frame of Abell 2744-QSO1. Given the apparently unphysical bad pixels in the optical, we added 5σ-clipping to the fit.

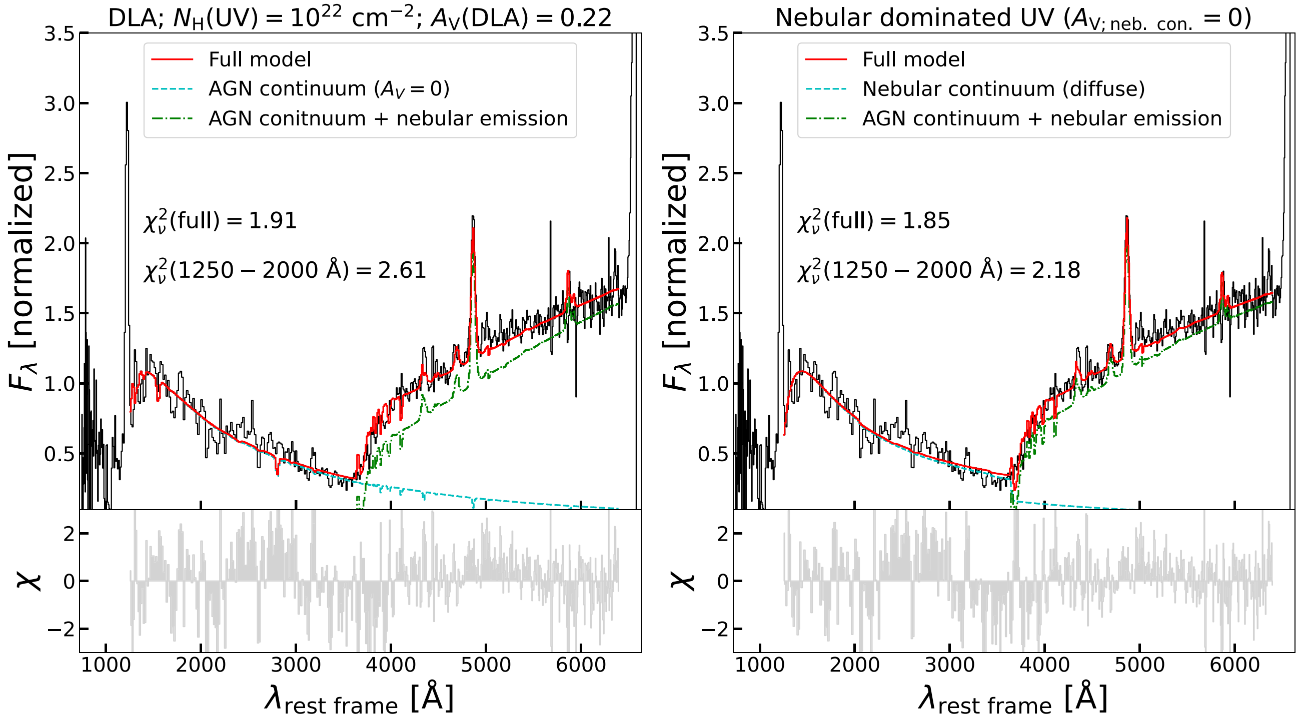

Figure C2. Best-fitting models for the PRISM combined images of A + B + C reduced by L. J. Furtak et al. (2024) in the rest-frame wavelength range of 1250 − 6400 Å with different assumptions in the UV. *Left:* the UV continuum is assumed to be the AGN continuum emission attenuated by a slab of gas with $N_{\rm H} = 10^{22}$ cm^{-2}. *Right:* the UV continuum is assumed to be a nebular continuum composed of a two-photon continuum, a hydrogen free-bound continuum, and a hydrogen free–free continuum. Both models assume no dust attenuation in the UV. The nebular continuum model provides a better fit compared to the DLA model.

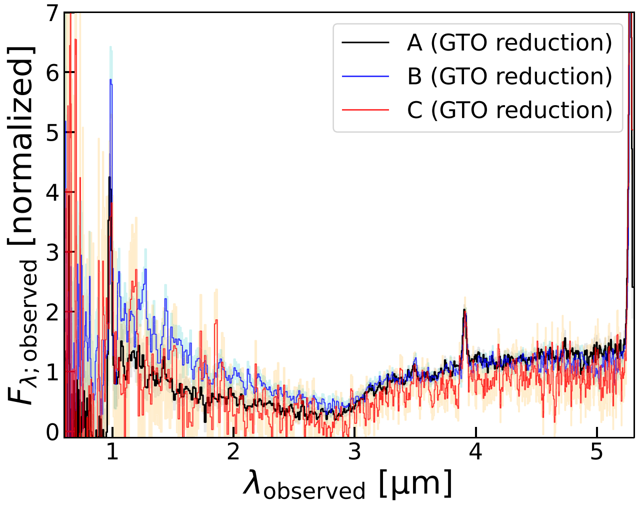

Figure C3. Comparison between three MSA PRISM spectra from the three images of Abell 2744-QSO1. The spectra are reduced with the GTO pipeline and are normalized to the flux density at $\lambda = 3.6$ μm. The rest-frame UV continuum of the spectrum from image B is bluer compared to the other two spectra, possibly due to a background subtraction issue.

range of 1250 – 6400 Å. As can be seen in Fig. 1, L. J. Furtak et al. (2024)'s spectrum shows a smoother DLA-like feature around Lyα. This actually makes the DLA model with $N_{\mathrm{H}} = 10^{22}$ cm^{-2} with a small amount dust attenuation [A_{V}(DLA) = 0.22] fail to describe the UV part well (left panel), assuming the intrinsic UV spectrum has an AGN origin. In comparison, a nebular dominated UV continuum with $T_{\mathrm{e}} = 30\,000$ K is able to the fit the UV part better, especially the turnover feature around Lyα.

The different result from the L. J. Furtak et al. (2024)'s spectrum is likely caused by the inclusion of image B. As shown in Fig. C3, when the spectra from three images are normalized to the rest-frame optical, the UV continuum of image B shows a different slope compared to the other two images. As we have noted in Section 2, the MSA PRISM spectrum from image B (included in the combined spectrum of L. J. Furtak et al. 2024) possibly has a background subtraction issue, which might affect the DLA-like feature in the UV and lead to the different fitting result. In addition, we caution that in our analyses, the normalization of the nebular continuum is set to a free parameter during the fit.

Figs C4 and C5 show the corresponding results for the integrated IFU PRISM spectrum from the observations of BlackTHUNDER. Here the spectrum is taken from the central 0″.2 of image A only. In Table 3, one can see that the best-fitting model has the steepest UV slopes among all the fits. The best-fitting A_{V} is 0.09 magnitudes lower than that of the A + C images. Similar to the results of the A + C images, a DLA model is favoured over the nebular dominated model for the UV part of the spectrum.

Finally, we show our fit to the spectrum from the UNCOVER DR4 adopted by Y. Ma et al. (2025) in Fig. C6. This reduced spectrum produces the largest χ^2_ν, which is still significantly lower than the fitting results from Y. Ma et al. (2025). The comparison between the DLA fit and the nebular continuum fit is shown in Fig. C7. Similar to the result based on image A from BlackTHUNDER, the DLA model provides a better fit compared to the nebular continuum model. This further indicates the different result obtained from the PRISM spectrum of L. J. Furtak et al. (2024) might be caused by the spectrum from image B.

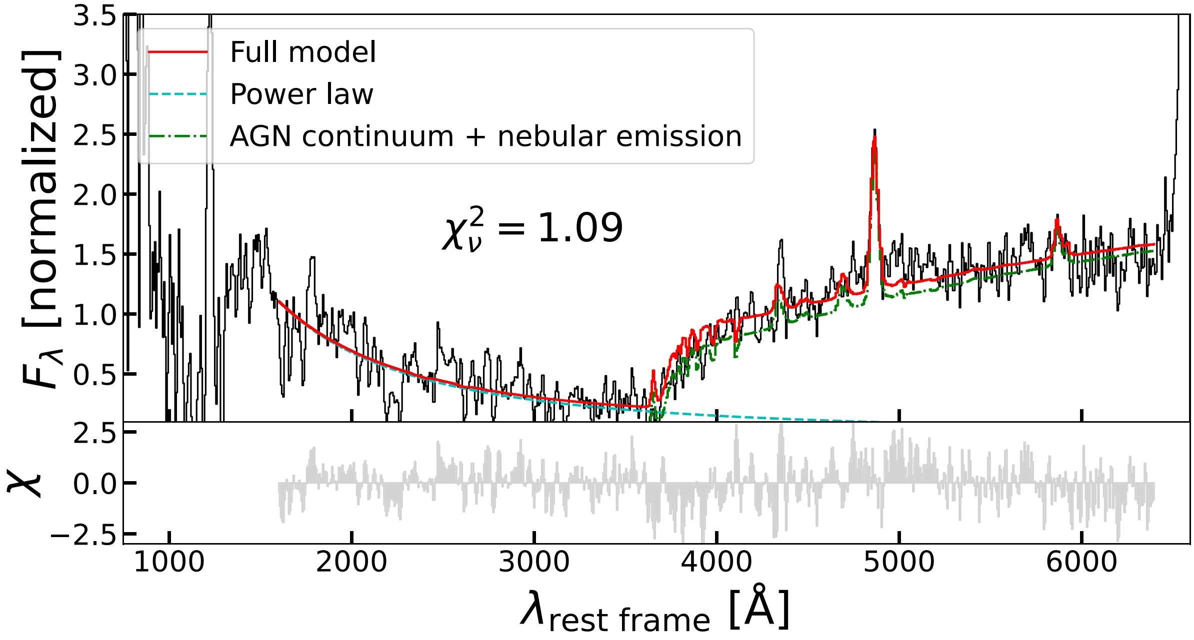

Figure C4. Fiducial fit for the integrated PRISM IFU spectrum of image A from BlackTHUNDER in the rest-frame wavelength range of 1600 – 6400 Å. The observed PRISM spectrum is normalized to the flux density at $\lambda = 4260$ Å in the rest frame of Abell 2744-QSO1.

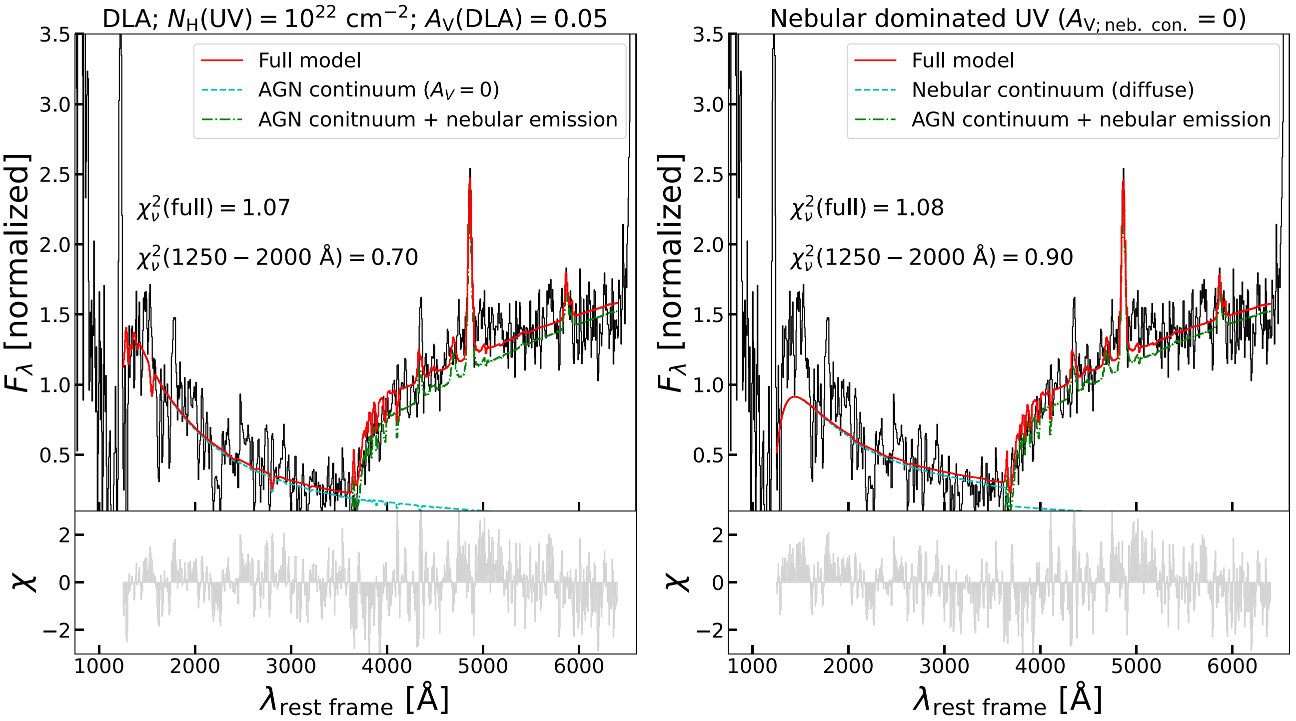

Figure C5. Fiducial fit for the integrated PRISM IFU spectrum of image A from BlackTHUNDER in the rest-frame wavelength range of 1250 – 6400 Å with different assumptions in the UV. *Left:* the UV continuum is assumed to be the AGN continuum emission attenuated by a slab of gas with $N_{\rm H} = 10^{22}$ cm^{-2}. *Right:* the UV continuum is assumed to be a nebular continuum composed of a two-photon continuum, a hydrogen free-bound continuum, and a hydrogen free–free continuum. Both models assume no dust attenuation in the UV. The nebular continuum model provides a worse fit compared to the DLA model.

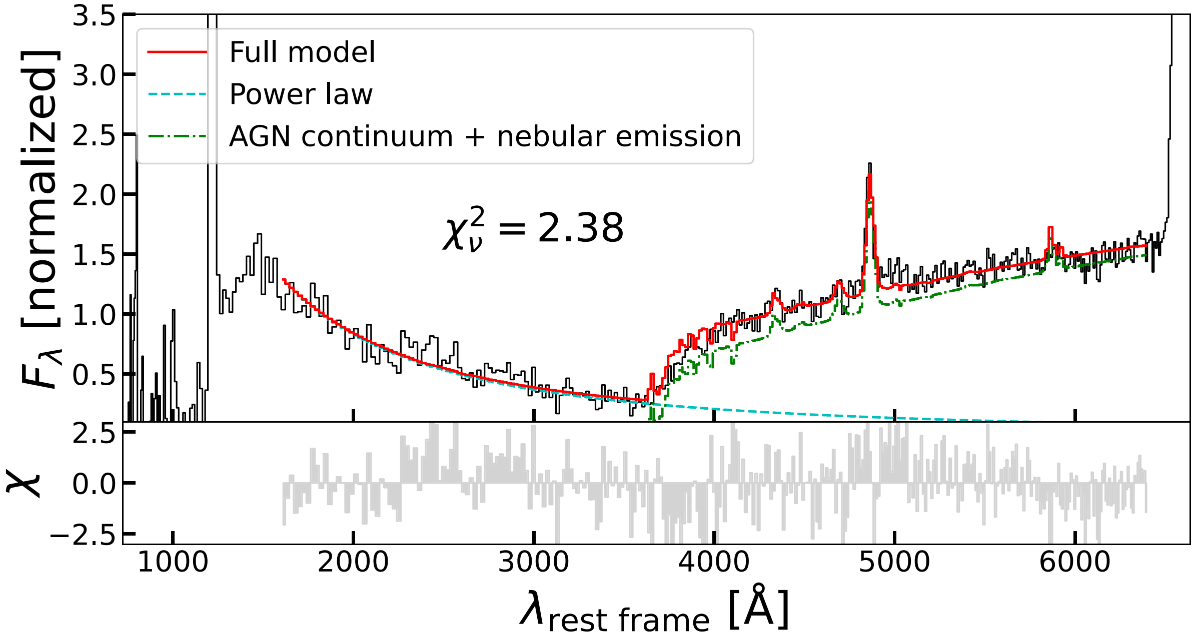

Figure C6. Fiducial fit for the image A of Abell 2744-QSO1 from the UNCOVER data release in the rest-frame wavelength range of 1600 – 6400 Å. This is the same spectrum that was fitted by Y. Ma et al. (2025), who obtained $\chi^2_\nu = 2.74 - 4.32$ based on their models. The observed PRISM spectrum is normalized to the flux density at $\lambda = 4260$ Å in the rest frame of Abell 2744-QSO1. We adopted 5σ-clipping during the fit.

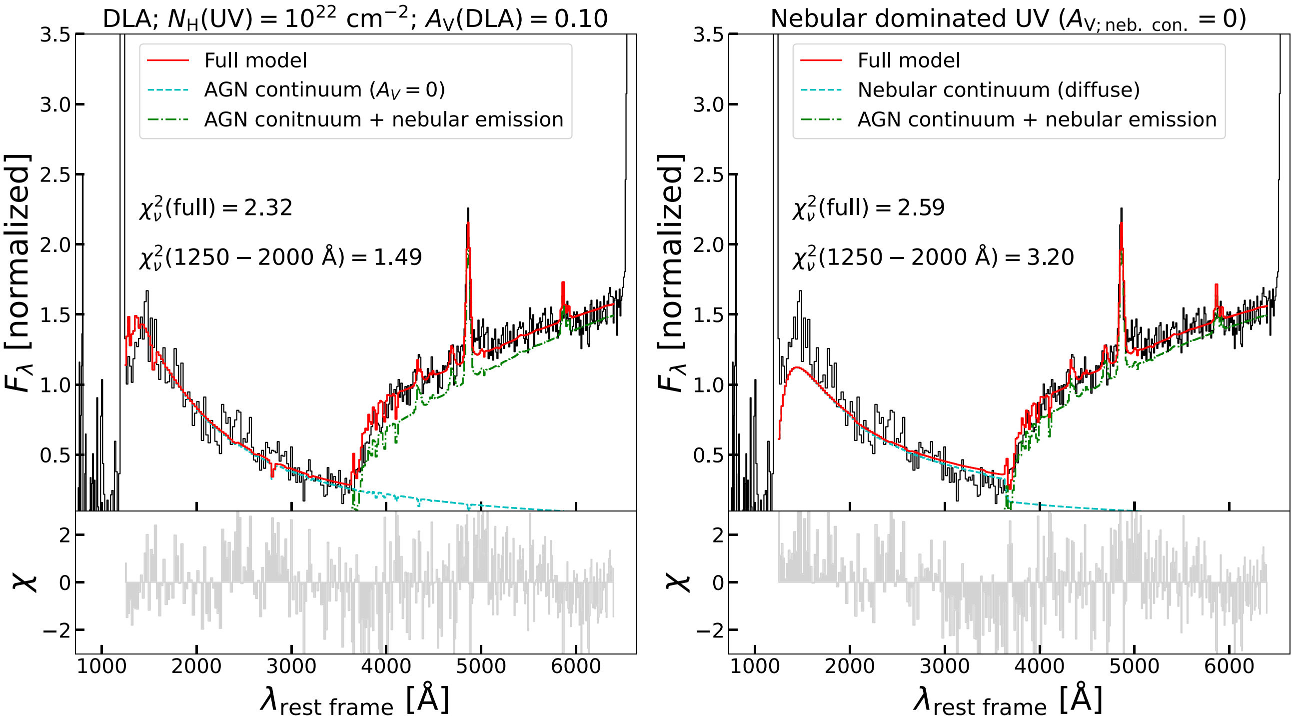

Figure C7. Fiducial fit for the spectrum of image A from UNCOVER DR4 in the rest-frame wavelength range of 1250 − 6400 Å with different assumptions in the UV. *Left:* the UV continuum is assumed to be the AGN continuum emission attenuated by a slab of gas with $N_{\rm H} = 10^{22}$ cm^{-2}. *Right:* the UV continuum is assumed to be a nebular continuum composed of a two-photon continuum, a hydrogen free-bound continuum, and a hydrogen free–free continuum. Both models assume no dust attenuation in the UV. The nebular continuum model provides a worse fit compared to the DLA model.

APPENDIX D: ADDITIONAL ANALYSES AND INFORMATION ON VARIABILITY

In this appendix, we provide some additional multi-epoch analyses on the variability of Abell 2744-QSO1. We also discuss the impact of the data reduction on the variability analysis.

D1 Comparison of IFU and MSA spectra of image A

As already discussed in the main text, the BlackTHUDER IFU spectrum taken in November 2024, provides an additional spectroscopic epoch of image A, relative to the MSA spectrum taken in July 2023 (i.e. 1.7 months earlier in the source rest-frame). Fig. D1 compares the PRISM spectrum of image A extracted from the IFU Cube with the PRISM MSA spectrum. The two spectra are consistent with each other within the errors, implying that the source has probably been stable within the ~ 2 months in the rest frame covered by the two observations, although intra-epoch variability cannot be excluded.

It is, however, intriguing that some changes are seen in the emission lines. The Hβ is slightly higher in the IFU spectrum, although within the uncertainties (both Poissonian and calibration). However, the variation is not seen in terms of equivalent width (Section 7; i.e. when the spectra are normalized to the continua), meaning that the slight variation of Hβ may be simply due to a calibration effect.

Also, Hγ seems stronger in the IFU spectrum. However, this is still only at the 2σ level, and it is possible that this is due to an artefact in the IFU PRISM cube. Alternatively, it may trace real variability in the absorbing medium (either in the Balmer absorption or dust absorption, if located in the outer parts of the BLR). Or, the IFU may be tracing gas on more extended scales, and less obscured, that is missed by the MSA. There is no clear evidence for extension of the Balmer lines, but it is also true that image A is located at the edge of the shutter, hence some structural variation close to the resolution limit may result in flux differences between the MSA and the IFU.

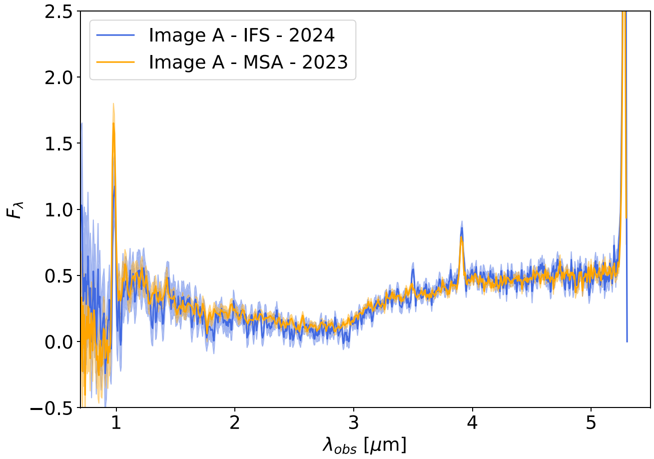

Figure D1. Comparison of the two low resolution spectra of Image A of Abell2744-QSO1 obtained with the MSA in November 2023 (orange, front, reduced with the GTO pipeline) and with the IFU in Nov 2024 through the BlackTHUNDER programme (blue, back). There are not significant variations between the two spectra.

Some flux variation, again only at the $\sim 2\sigma$ level is seen in Lyα. Once again, variability of the Lyα emission lines between the two epochs cannot be excluded. However, Lyα is spectrally unresolved or marginally resolved, hence the apparent drop in the peak flux of

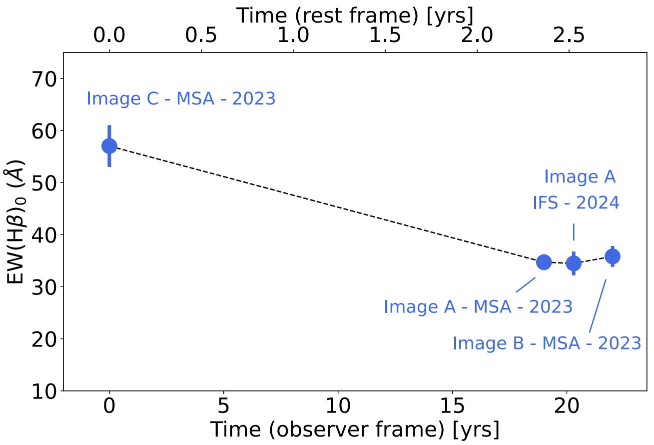

Figure D2. Same as Fig. 10, but where now the spectra are not obtained from the full-shutter pipeline extraction, which takes properly into account the path- and diffraction-losses, but by extracting the spectrum from 3-pixel apertures from the 2D spectra (which does not take into account for path- and diffraction-losses). In this case the EW variation of Hβ is still highly significant, but reduced. The effect is likely arising from the inappropriate spectral extraction in this case.

Lyα is mostly due to the MSA having higher resolution (hence the line more peaky) than in the IFU spectrum.

D2 Issues associated with custom-extraction from the 2D spectra

As already pointed out in Section 2.2, the correction of path- and diffraction-losses is very accurate for unresolved sources like this one. The pipeline extraction of the spectra from the full-shutter takes into account of these aspects. On the contrary, extracting the 1D spectra with bespoke apertures on the 2D spectra is deprecated if one wants to carefully account for the flux calibration, as this procedure does not take into account the path- and diffraction-losses, and this can introduce issues when looking for variability. Especially for sources located close to the edge of the shutter, using extraction from the 2D spectra can easily lead to inappropriate flux calibration, and the effect can also be more pronounced at the location of strong emission lines, whose PSF and diffraction losses may not be captured by a fixed or bespoke aperture on the 2D spectrum. As stated, the rigorous approach is to take the full-shutter spectra extracted by the pipeline. In order to illustrate the effect of using the bespoke extraction from the 2D, Fig. D2 shows the quantities same as Fig. 10, i.e. the variation of EW among different observations, but where the EWs are measured on spectra extracted from 3-pixel aperture on the 2D spectrum (i.e. similar to the optimized extraction used in other works), instead of the pipeline full-shutter extraction. The variation in EW in image C is still highly significant, but it is now reduced to about 50 per cent–60 per cent. This is not due to an extended component of Hβ (which might result in picking more Hβ in the full shutter relative to the 3 pixel extraction). Indeed, we have checked in the IFU cube that the EW(Hβ) changes less than 2 per cent using spectra extracted from $0\farcs2$ and $0\farcs5$ apertures. The difference is instead likely originating from the fact that the bespoke extraction from the 2D spectrum does not incorporates path- and diffraction-losses, which may be particularly problematic around strong emission lines and especially for sources close to the edge of the spectrum.

[1] *Kavli Institute for Cosmology, University of Cambridge, Madingley Road, Cambridge CB3 0HA, UK*
[2] *Cavendish Laboratory, University of Cambridge, 19 JJ Thomson Avenue, Cambridge CB3 0HE, UK*
[3] *Department of Physics and Astronomy, University College London, Gower Street, London WC1E 6BT, UK*
[4] *Max-Planck-Institut für extraterrestrische Physik, Gießenbachstraße 1, D-85748 Garching, Germany*
[5] *Center for Astrophysics, Harvard and Smithsonian, 60 Garden St., Cambridge, MA 02138, USA*
[6] *Centro de Astrobiología (CAB), CSIC-INTA, Ctra. de Ajalvir km 4, Torrejón de Ardoz, E-28850 Madrid, Spain*
[7] *Scuola Normale Superiore, Piazza dei Cavalieri 7, I-56126 Pisa, Italy*
[8] *Department of Physics, University of Oxford, Denys Wilkinson Building, Keble Road, Oxford OX13RH, UK*
[9] *Sorbonne Université, CNRS, UMR 7095, Institut d'Astrophysique de Paris, 98 bis bd Arago, F-75014 Paris, France*
[10] *INAF – Osservatorio Astrofisico di Arcetri, largo E. Fermi 5, I-50127 Firenze, Italy*
[11] *European Southern Observatory, Karl-Schwarzschild-Strasse 2, D-85748 Garching, Germany*
[12] *Steward Observatory, University of Arizona, 933 N Cherry Avenue, Tucson, AZ 85721, USA*
[13] *Institute of Astronomy, University of Cambridge, Madingley Road, Cambridge CB3 0HA, UK*
[14] *Kavli Institute for Astronomy and Astrophysics, Peking University, Beijing 100871, China*
[15] *Waseda Research Institute for Science and Engineering, Faculty of Science and Engineering, Waseda University, 3-4-1, Okubo, Shinjuku, Tokyo 169-8555, Japan*
[16] *AURA for European Space Agency, Space Telescope Science Institute, 3700 San Matin Drive, Baltimore, MD 21218, USA*
[17] *Dipartimento di Fisica e Astronomia, Università di Bologna, Via Gobetti 93/2, I-40129 Bologna, Italy*
[18] *INAF – Osservatorio di Astrofisica e Scienza dello Spazio di Bologna, Via Gobetti 93/3, I-40129 Bologna, Italy*
[19] *Department of Astronomy and Astrophysics University of California, Santa Cruz, 1156 High Street, Santa Cruz CA 96054, USA*
[20] *Dipartimento di Fisica, Sapienza Universita di Roma, Piazzale Aldo Moro 5, I-00185 Rome, Italy*
[21] *INAF/Osservatorio Astronomico di Roma, Via Frascati 33, I-00040 Monte Porzio Catone, Italy*
[22] *INFN, Sezione Roma1, Dipartimento di Fisica, 'Sapienza' Universita di Roma, Piazzale Aldo Moro 2, I-00185 Roma, Italy*
[23] *Sapienza School for Advanced Studies, Viale Regina Elena 291, I-00161 Roma, Italy*
[24] *Como Lake Center for Astrophysics, DiSAT, Universitádegli Studi dell'Insubria, via Valleggio 11, I-22100 Como, Italy*
[25] *NRC Herzberg, 5071 West Saanich Rd, Victoria, BC V9E 2E7, Canada*
[26] *Department of Astronomy, University of Geneva, Chemin Pegasi 51, CH-1290 Versoix, Switzerland*
[27] *Cosmic Dawn Center (DAWN), Elektrovej 327, 2800 Kgs. Lyngby, Copenhagen, Denmark*
[28] *Niels Bohr Institute, University of Copenhagen, Jagtvej 128, DK-2200 Copenhagen, Denmark*

This paper has been typeset from a TEX/LATEX file prepared by the author.